Fractal Geometry of Iso-Surfaces of a Passive Scalar in a Turbulent Boundary Layer

A Thesis
Presented to
The Academic Faculty

by

Frank Schuerg

In Partial Fulfillment
of the Requirements for the Degree
Master of Science in
Engineering Science and Mechanics

School of Civil and Environmental Engineering
Georgia Institute of Technology
November 2003

Copyright © 2003 by Frank Schuerg

Fractal Geometry of Iso-Surfaces of a Passive Scalar in a Turbulent Boundary Layer

Approved:

Dr. Donald R. Webster, Chairman

Dr. Laurence J. Jacobs, Second Chairman

Dr. P. K. Yeung

Date Approved 11/18/03

Acknowledgements

I am grateful to many people and institutions for their help in the preparation of this thesis. For the opportunity to work on this fascinating topic, the support, and the technical input, I thank my advisor Dr. Donald R. Webster. I am grateful to L. Prasad Dasi for data collection and introductory support. Many good suggestions came from my thesis committee members Dr. Laurence J. Jacobs and Dr. P. K. Yeung. I would also like to acknowledge with thanks the financial support by the U.S. National Science Foundation.

The thesis was written in the course of an exchange program with the University of Stuttgart, Germany. I would like to thank again the program coordinator Dr. Laurence J. Jacobs for his excellent administrative work. For the administration in Germany, I am grateful to the program coordinator Prof. Lothar Gaul and to Dr. Jan Wirnitzer. Thanks to Dr. Ulrich Rist for serving as German thesis co-advisor. The financial support for my foreign studies by the German Academic Exchange Service (DAAD) and the German Federal Education Grant Act (BaföG) are gratefully acknowledged.

For further financial and - more importantly - personal support, I wish to thank my Mom and Dad, my girlfriend Gabriele, and my whole family and friends. Whether by plane, by phone, via internet, or by mail, they found always a way to keep in touch with me while I was in my American ivory tower.

Contents

Acknowledgements iii

List of Tables vi

List of Figures vii

List of Variables ix

Summary xii

1 Introduction 1

2 Background 4

2.1 Turbulence theory and classical description 4

2.1.1 Characteristics of turbulence 4

2.1.2 Deterministic equations and random solutions 5

2.1.3 Statistical description of turbulence 7

2.1.4 Velocity field and energy cascade 9

2.1.5 Scalar field and turbulent mixing 12

2.1.6 Turbulent boundary layers 15

2.1.7 The concentration field of a continuous point source 17

2.2 Fractal geometry 20

2.2.1 Conceptual introduction 20

2.2.2 Levels of geometrical complexity 21

2.2.3 Embedding dimension and topological dimension 22

2.2.4 Deterministic self-similar fractals vs. natural objects 23

2.2.5 The fractal dimension in theory and practice 26

2.2.6 Dimensional classification of concentration iso-surfaces 31
2.2.7 Additional fractal measures for iso-surface description 35
2.2.8 Fractal dimension of iso-surfaces in the literature 39

3 Method **42**
3.1 Experiment setup 42
3.2 Numerical method 44
3.2.1 Image calibration 44
3.2.2 Choice of concentration threshold 45
3.2.3 Extraction of concentration iso-surfaces 47
3.2.4 Noise considerations 51
3.2.5 Box-counting algorithm 54
3.2.6 Calculation of fractal measures 59
3.3 Testing of algorithm 62
3.3.1 Approach 62
3.3.2 Creation of evaluation image sets 63
3.3.3 Quantitative assessment of algorithm accuracy 65

4 Results and discussion **76**
4.1 Statistics of the concentration field 76
4.2 Geometry of iso-surfaces 85
4.2.1 Qualitative description based on sample images 85
4.2.2 Quantitative description based on fractal geometry 86
4.3 Discussion and outlook 111

Bibliography **118**

List of Tables

Table 3.1 Important flow and plume parameters 43

Table 3.2 Rms of the deviation from the theoretical dimension 68

Table 3.3 Mean dimension, averaged over the inner 7-point plateau 69

Table 4.1 Concentration fields statistics and concentration thresholds 81

List of Figures

Figure 2.1	Generator for the contiguous $D = 1.6131$ Koch curve	23
Figure 2.2	Contiguous $D = 1.6131$ Koch curve	25
Figure 2.3	Alternative generators for the $D = 1.6131$ Koch curve	29
Figure 2.4	Partially dispersed $D = 1.6131$ Koch curve	30
Figure 2.5	Fully dispersed $D = 1.6131$ Koch curve	32
Figure 3.1	Raw intensity image	45
Figure 3.2	Concentration image	46
Figure 3.3	Concentration iso-surfaces for different concentration thresholds	48
Figure 3.4	Exemplary 8×8 conventional boundary pixels	50
Figure 3.5	Exemplary 8×8 boundary-outline pixels	51
Figure 3.6	Examples of noise	53
Figure 3.7	Exemplary box-counting subdivision of bounding box	55
Figure 3.8	Coverage count for a typical boundary-outline pixel image	56
Figure 3.9	Shifting of the starting location for the box-counting subdivision	57
Figure 3.10	Generators for the randomly dispersed Koch curves	64
Figure 3.11	Exemplary Koch curves for the 5 different dimensions	66
Figure 3.12	12 samples from the set of 1000 evaluation images for $D = 1.1046$	70
Figure 3.13	12 samples from the set of 1000 evaluation images for $D = 1.2553$	71
Figure 3.14	12 samples from the set of 1000 evaluation images for $D = 1.4466$	72
Figure 3.15	12 samples from the set of 1000 evaluation images for $D = 1.6131$	73
Figure 3.16	12 samples from the set of 1000 evaluation images for $D = 1.7604$	74
Figure 3.17	Box-counting dimensions for the five evaluation image sets	75
Figure 4.1	Exemplary pixel concentration time series	77
Figure 4.2	PDFs of instantaneous concentration fields	78
Figure 4.3	Streamwise concentration mean and sdev across image region	79

Figure 4.4 Cross-stream concentration mean and sdev across image region 80
Figure 4.5 PDFs of normalized fluctuating concentration fields 82
Figure 4.6 Concentration mean and standard deviation versus distance .. 83
Figure 4.7 12 sample boundary-outline images for $C_{th,3}$ at $x = 250$ mm .. 87
Figure 4.8 12 sample boundary-outline images for $C_{th,3}$ at $x = 500$ mm .. 88
Figure 4.9 12 sample boundary-outline images for $C_{th,3}$ at $x = 1000$ mm . 89
Figure 4.10 12 sample boundary-outline images for $C_{th,3}$ at $x = 2000$ mm . 90
Figure 4.11 Coverage count 92
Figure 4.12 Coverage fraction 93
Figure 4.13 Coverage dimension 95
Figure 4.14 Coverage dimension as a function of distance from the source. 96
Figure 4.15 Coverage dimension for an absolute concentration threshold .. 97
Figure 4.16 Coverage length 100
Figure 4.17 Underestimate of total coverage length 103
Figure 4.18 LEB-scale PDF 104
Figure 4.19 Scale-cumulative length-area ratio 106
Figure 4.20 Scale-cumulative length-area ratio exponent 107
Figure 4.21 Scale-local length-area density 108
Figure 4.22 Scale-local length-area density exponent 109
Figure 4.23 Length-area density exponent for low concentration thresholds 110
Figure 4.24 Fitting of the coverage dimension 112
Figure 4.25 Analytical versus measured underestimated coverage length .. 114
Figure 4.26 Underestimated coverage length for absolute length scales 115

List of Variables

A	Parameter of calibration equation
B	Parameter of calibration equation
B_1	Parameter of mean velocity profile in a turbulent boundary layer
B_2	Parameter of mean velocity profile in a turbulent boundary layer
b	Subdividing factor of the self-similar cascade
C	Instantaneous concentration
$\tilde{C}$	Sample space variable of concentration
$\langle C \rangle$	Mean concentration
C_{th}	Concentration threshold
C^*	Concentration normalized by the source concentration
c	Fluctuating concentration
c'	Root mean square (rms) fluctuating concentration
cal	Calibration image number
cal_{max}	Total number of calibration images
D_d	Fractal dimension; coverage dimension; Hausdorff-Besicovitch dimension
D_C	Coastline dimension
d	Embedding dimension; diameter of a pipe
d_t	Topological dimension
E	Kinetic energy spectrum
F_d	Coverage fraction
f_d	LEB-scale PDF
g_d	Scale-local area-volume density
H	Water depth
h	Hausdorff measure
I	Raw light intensity

i	Streamwise pixel number
j	Vertical pixel number
K	Experimental constant to estimate the eddy diffusivity
k	Wave number; von Karman constant
L_d	Coverage length
$L_{d,u}$	Coverage length underestimate
l	Integral length scale
M	Number of line segments of a generator
M_C	Number of line segments of a coastline generator
$\dot{m}_{source}$	Passive scalar mass flow rate from the source
N_d	Coverage count
n	Image number; concentration threshold number
n_{max}	Total number of images
P	Instantaneous pressure; probability
$\langle P \rangle$	Mean pressure
p	Fluctuating pressure; step number of the self-similar cascade
q	Molecular flux per unit area
r	Subdivision factor of the self-similar cascade
Re	Reynolds number
$S_{i,j}$	Mean strain rate tensor
s	Box-counting subdivision step
s_{max}	Total number of box-counting subdivisions
$s_{i,j}$	Fluctuating strain rate tensor
Sc	Schmidt number
t	Time
U	Instantaneous velocity
U_0	Free stream velocity outside the boundary layer
u	Fluctuating velocity
u'	Root mean square (rms) fluctuating velocity
u_τ	Wall friction velocity

$\langle U \rangle$	Mean velocity
u^+	Normalized mean velocity in a boundary layer
V	Velocity
$\dot{V}_{source}$	Passive scalar source flow rate
x	Streamwise coordinate direction
y	Transverse coordinate direction; vertical distance from the wall
y^+	Wall units
z	Vertical coordinate direction
α_Ω	Scale-cumulative area-volume ration exponent
α_g	Scale-local area-volume density exponent
Γ	Scalar spectrum; Gamma function
γ	Generalized volume of a unity sphere
δ	Boundary layer thickness; cross-stream plume extent
δ_b	Size of the bounding box
δ_ν	Viscous length scale
ϵ	Dissipation rate of turbulent kinetic energy
η	Kolmogorov length scale
η_B	Batchelor length scale
κ	Molecular diffusivity of a scalar quantity
κ_T	Turbulent eddy diffusion coefficient
λ	Length scale
λ_{grid}	Grid resolution
ν	Kinematic viscosity of a fluid
Π	Wake strength parameter
ρ	Density of a fluid
τ_w	Wall shear stress
χ	Dissipation rate of scalar variance
Ω_d	Scale-cumulative area-volume ratio

Summary

The objective is to study the fractal geometry of concentration iso-surfaces of a non-buoyant, high Schmidt number ($\mathrm{Sc} \approx 1000$), passive scalar field produced by an iso-kinetic point source in the inertial layer of a fully developed turbulent boundary layer of an open channel flow. The data consists of a sequence of instantaneous planar concentration images (collected via PLIF), for four distances from the source. The measurements resolve the Batchelor length scale in both dimensions of the laser plane and are slightly under-resolved in the perpendicular direction. The evolving iso-surfaces are defined by a threshold concentration level and the boundary-outline method is used to extract the iso-surfaces from each image. A box-counting algorithm is applied to determine the coverage count for the extracted iso-surfaces.

The fractal dimension and other fractal measures are found to depend on the scale. In the inertial-convective range, the fractal measures clearly depend on the concentration threshold level that defines the iso-surfaces. For instance, the fractal dimension decreases as the threshold level increases. With increasing distance from the source, the fractal dimension decreases for iso-surfaces defined by higher thresholds and increases for iso-surfaces defined by lower thresholds. Overall, the fractal measures suggest that few, sparse dye filaments of high concentration and with steep gradients are distorted by the turbulent motions. As they evolve downstream, the peaks become less steep and the dye filaments break up into several dispersed, smoother objects. This indicates an overall homogenization of the concentration field.

In the viscous-convective range, the fractal dimension is observed to be essentially independent of both the concentration threshold and the distance from the source. A polynomial curve is fitted to obtain an analytical relation for the universal fractal dimension as function of scale. Other fractal measures can be derived analytically based on the fitted curve. For instance, the coverage length underestimate measures

the degree to which the iso-surface area is underestimated when the measurements of the turbulent concentration field are under-resolved. The result is expected to be valuable in the development of subgrid-scale models, for example.

CHAPTER 1

Introduction

Examples of turbulent mixing processes include stirring in a cup of coffee to dissolve cream and sugar, releasing smoke from a cigarette into the ambient air, and injecting fuel and air into the cylinders of a car engine. Each example involves interfaces between mixed and unmixed fluid regions denoted by different species concentration, temperature, or density levels. Defining interfaces in a continuously varying concentration field, for example, is often challenging. Once interfaces are defined, however, they are typically characterized as convoluted, folded, and wrinkled surfaces.

The geometry of these fluid interfaces is of practical importance in a number of natural and engineered shear flow environments. First, in non-reactive mixing processes, the molecular flux according to Fick's law occurs across concentration gradients at interfaces. Estimating the resulting mixing rate is necessary, for example, for predicting the release of pollutants into the atmosphere through a stack or the discharge of waste water into a stream. Second, in reactive mixing, the reaction rate depends on the size and shape of the interface, which may be an defined by an iso-surface of the stoichiometric species concentration. Examples are combustion chambers in vehicles or power plants, and reactors in chemical engineering processes. Third, electromagnetic and acoustic wave propagation in fluids are influenced by interfacial structure. As the wave speed commonly changes across interfaces, passing waves are subject to refraction and reflection. This effect is encountered in aero-optic and aero-acoustic applications, for example in earth-based astronomy, and for noise control of an aircraft.

Classical turbulence theory (Kolmogorov, 1941) and the theory of turbulent mixing of a passive scalar, such as species concentration or slight perturbations of temperature or density (Obukhov, 1949; Corrsin, 1951; Batchelor, 1959), focus on descriptions of spectral space instead of physical space. However, the fact that self-similarity and power-law behavior are observed in spectral space (at least to some extent for small scales) raises hope for finding universal behavior in physical space as well. The theory of fractal geometry (Mandelbrot, 1982) provides a number of powerful measures to describe complex objects in physical space. Quantifying the structure of fluid interfaces by means of fractal geometry serves several purposes. The physical space measures, as opposed to spectral space, allow for a direct prediction of mixing efficiency and reaction rate. In addition, the physical space measures enable us to identify the relevant parameters for the design and control of turbulent mixing and reaction processes (such as Reynolds number, mean scalar gradient, or flow geometry). A discovery of universal characteristics of fluid interfaces in physical space could form a basis for a turbulence theory based on universality of physical characteristics. More practically, the universal characteristics could be used to develop subgrid-scale models for numerical simulations of turbulent mixing processes.

The present study focuses on concentration iso-surfaces (i.e. surfaces defined by iso-contours of the concentration of a passive scalar), created by iso-kinetically releasing dye into the inertial layer of a fully developed turbulent boundary layer of an open channel flow. For example, this arrangement serves as model for waste water discharge into a stream. Fractal geometry measures will be utilized to quantify the complex iso-surface structure and to thereby characterize the mixing process downstream of the source. Chapter 2 consists of a general review of turbulence and turbulent mixing. In the same chapter, we introduce the concepts of fractal geometry, and define the most important measures to describe the iso-surface geometry. In Chapter 3, the experiment setup is briefly summarized. The primary focus of this chapter is the numerical method to extract iso-surfaces and calculate fractal measures. In addition, the performance of the algorithm is extensively tested and evaluated by evaluating theoretical fractal objects. The experimental results are presented in

Chapter 4. We give a detailed description of the turbulent mixing process based on a combination of classical statistics of the concentration field, qualitative examination of concentration iso-surface images, and fractal measures of the concentration iso-surface geometry. Finally, theoretical and practical implications of the results are discussed and interpreted, and an outlook is provided.

CHAPTER 2

Background

2.1 Turbulence theory and classical description

2.1.1 Characteristics of turbulence

In 1883, Osborne Reynolds conducted experiments on water flow through smooth, straight pipes. By injecting a thin stream of dye into the flow he was able to distinguish two drastically different flow types occurring in the pipe. At low flow rates, the dye stream followed a smooth, well-defined, and easily predictable path. This type of flow is called laminar, as the fluid moves smoothly, without macroscopic mixing motions across velocity gradients. At a higher flow rate, however, a transition to another flow type was observed. The formerly smooth dye stream became irregular, fluctuating, and unpredictable, and exhibited strong macroscopic mixing motions that spread the dye quickly over the cross-section of the pipe. Such a flow is called turbulent. Reynolds found that the transition from laminar to turbulent flow occurred at a fixed value of a parameter that is now called Reynolds number, $\mathrm{Re} = Vd/\nu$, where V is the velocity averaged over the cross-section, d is the diameter of the pipe, and ν is the kinematic viscosity of the fluid.

Most flows occurring in nature and engineering applications are turbulent. Examples include the boundary layer of the earth's atmosphere, major oceanic currents like the Gulf Stream, boundary layers over aircrafts, cars, or submarines, and mixing and combusting flows in reactors. While it is not trivial to define turbulence *precisely*, a number of characteristics must be present for a flow to be turbulent:

- Irregularity: Turbulent flows appear irregular and chaotic. It is impossible to give a detailed prediction of the development of the motions in the future based on present flow conditions.

- Diffusivity: Turbulent flows exhibit strong macroscopic motions of fluid elements, which cause rapid mixing and increase the rates of momentum, heat, and mass transfer.
- Nonlinearity: Turbulent flows require a nonlinear amplification of small perturbations to reach a chaotic state.
- Three-dimensional vorticity: Turbulent flows are characterized by high levels of fluctuating vorticity. Vorticity manifests itself in identifiable structures within the flow, called eddies, that coexist at a vast range of scales. Kinetic energy of the fluctuations is transferred among scales by means of the nonlinear, three-dimensional mechanism of vortex tilting and stretching.
- Dissipation: Turbulent flows are always dissipative. The vortex tilting and stretching mechanism transfers kinetic energy and vorticity to increasingly smaller scales. Finally, velocity gradients become so large that the kinetic energy is dissipated to heat by viscosity. Thus, to sustain turbulence a constant energy supply is needed to balance the viscous losses.

Unless stated otherwise, the following brief introduction to turbulence theory and characteristics of turbulent flows is based on three introductory turbulence books, namely Tennekes and Lumley (1972), Pope (2000), and Kundu (1990).

2.1.2 Deterministic equations and random solutions

The mixing of a passive scalar in a turbulent flow, such as the dye in Reynolds' water pipe, can be described in terms of the velocity $U_i(x_i, t)$, pressure $P(x_i, t)$, and concentration $C(x_i, t)$ fields. The system is governed by conservation of mass, the

Navier-Stokes equations, and the scalar evolution equation. If we assume incompressible flow and neglect body forces, these equations are

$$\begin{aligned} \frac{\partial U_i}{\partial x_i} &= 0, && (2.1) \\ \frac{\mathrm{D}U_i}{\mathrm{D}t} &= -\frac{1}{\rho}\frac{\partial P}{\partial x_i} + \nu \frac{\partial^2 U_i}{\partial x_j \partial x_j}, && (2.2) \\ \frac{\mathrm{D}C}{\mathrm{D}t} &= \kappa \frac{\partial^2 C}{\partial x_j \partial x_j}, && (2.3) \end{aligned}$$

where ν is the kinematic viscosity of the fluid, and κ is the molecular diffusivity of the scalar quantity. The equations are constrained by the appropriate initial and boundary conditions for inflow, outflow, and fluid barriers. An interesting question is how this *deterministic* set of equations of motion, Eqs. 2.1 - 2.3, connects with the obvious *random* nature of turbulent flows. A combination of two observations addresses this question. First, in any flow, there are perturbations in the initial and boundary conditions. Second, turbulent flows exhibit an extreme sensitivity to such perturbations.

In fact, much simpler mechanical systems can display chaotic behavior. Bublath (1992) gave the demonstrative example of a steel pendulum swinging over two magnets that are arranged symmetrically about the pendulum's equilibrium position. Depending on the initial deflection of the pendulum, it will come to rest exactly above one of the magnets, due to the magnetic force. However, unless the starting location of the pendulum is trivial (i.e. the equilibrium position, or a location directly above one of the two magnets), it is impossible to predict the magnet over which the pendulum will come to rest. It turns out that even infinitesimal changes in the initial conditions (i.e. the starting location of the pendulum) or the boundary conditions (such as air friction or vibrations) change the outcome of the experiment. For the dye in Reynolds' water pipe, and for turbulent flows in general, this implies that it is impossible to predict instantaneous velocities or concentrations at particular points in space and time because we *never* know the initial and boundary conditions *exactly.*

2.1.3 Statistical description of turbulence

As explained in the previous section, the randomness of turbulence makes a deterministic approach impossible. Instead, one has to consider the instantaneous turbulent flow conditions, such as velocity, pressure, temperature, etc. as random variables and must employ statistical methods to make quantitative statements about the flow. As the emphasis of the present study lies on turbulent concentration fields, we will use the instantaneous dye concentration, C, to demonstrate the properties of random variables.

For an injected dye, such as Reynolds' pipe flow experiment, there is a range of possible concentrations, bounded by the injection concentration as the upper limit and the pure ambient water as the lower limit. We call this range the sample space, and introduce an independent sample space variable, $\tilde{C}$, which can take all possible values. For other random variables, however, the sample space may have other bounds or may even be unbounded. Therefore, in the following we will consider the most general case of an unbounded sample space. The probability, P, that the instantaneous concentration at a point in space and time, $C(x_i, t)$, lies within the subinterval of the sample space, $\tilde{C}_a \leq C \leq \tilde{C}_b$, can be derived from

$$P\{\tilde{C}_a \leq C \leq \tilde{C}_b\} = \int_{\tilde{C}_a}^{\tilde{C}_b} f(\tilde{C}) \mathrm{d}\tilde{C}, \tag{2.4}$$

where $f(\tilde{C})$ is the probability density function (PDF) of the concentration distribution at that particular spatial location. In other words, the PDF $f(\tilde{C})$ is the probability per unit distance in the sample space. It is non-negative, i.e. $f(\tilde{C}) \geq 0$, and satisfies the normalization condition $\int_{-\infty}^{\infty} f(\tilde{C}) \mathrm{d}\tilde{C} = 1$. The PDF $f(\tilde{C})$ fully characterizes the random variable C.

Reynolds recognized that for turbulent flows it is convenient to decompose the instantaneous flow variables into the sum of the mean and a fluctuation. If we assume that the dye was injected through a nozzle located at the centerline of the pipe, the instantaneous concentration, C, consists of a mean concentration, which varies symmetrically about the pipe's centerline, and a random concentration fluctuation that, despite its unpredictability, also exhibits a distinct spatial structure. We use upper-case letters for the instantaneous variables. The mean is indicated by angled brackets, and the fluctuation is indicated by lower-case letters. Using that notation, the decomposition of the instantaneous concentration can be expressed as

$$C = \langle C \rangle + c. \tag{2.5}$$

If the PDF $f(\tilde{C})$ of the random variable C is known, one can readily calculate the statistics of this variable. The mean is defined by

$$\langle C \rangle = \int_{-\infty}^{\infty} \tilde{C} f(\tilde{C}) \mathrm{d}\tilde{C}. \tag{2.6}$$

The variance is defined to be the mean-square fluctuation,

$$\mathrm{var}(C) = \langle c^2 \rangle = \int_{-\infty}^{\infty} (\tilde{C} - \langle C \rangle)^2 f(\tilde{C}) \mathrm{d}\tilde{C}, \tag{2.7}$$

and the square-root of the variance is the standard deviation,

$$\mathrm{sdev}(C) = \sqrt{\mathrm{var}(C)} = \langle c^2 \rangle^{1/2}, \tag{2.8}$$

which is also frequently called the root mean square (rms) concentration, c'.

In turbulence, however, the PDF of a random variable is generally unknown. The higher-order moments of turbulent flow variables exhibit significant deviations from the distributions that are known in the field of statistics, such as the normal (or Gaussian) distribution. As a result, the mean of a random flow variable is usually calculated as the ensemble average over several realizations. Suppose that a collection of a total of n_{max} experiments, conducted under the same conditions, yields concentration time records $C^n(t)$, for $1 \leq n \leq n_{max}$. The ensemble average of $C(t)$ is then given by

$$\langle C(t) \rangle = \frac{1}{n_{max}} \sum_{n=1}^{n_{max}} C^n(t), \tag{2.9}$$

which may still be a function of time. For a temporally stationary process, the ensemble average can be replaced by a time mean, as given by

$$\langle C(t) \rangle = \lim_{t_0 \to \infty} \frac{1}{t_0} \int_0^{t_0} C(t) dt = \mathrm{const.} \tag{2.10}$$

By definition, the mean of a fluctuation is zero, i.e. $\langle c \rangle = 0$.

2.1.4 Velocity field and energy cascade

To understand the process of turbulent mixing, it is necessary to take a closer look at the characteristics of both the velocity and passive scalar concentration fields, which in fact exhibit a number of similarities. The more general velocity field is discussed in this section because its characteristics appear in every turbulent flow, independent of the presence of a passive scalar. Often, the mean velocity is the focus of the analysis. The evolution equation for the mean velocity is found by performing the Reynolds-average (analogous to the time average in Eq. 2.10) of the continuity and Navier-Stokes equations (Eqs. 2.1 and 2.2). This procedure yields the Reynolds-averaged equations of motion:

$$\frac{\partial \langle U_i \rangle}{\partial x_i} = 0, \tag{2.11}$$

$$\frac{\mathrm{D}\langle U_i \rangle}{\mathrm{D}t} = -\frac{1}{\rho}\frac{\partial \langle P \rangle}{\partial x_i} + \nu \frac{\partial^2 \langle U_i \rangle}{\partial x_j \partial x_j} - \frac{\partial \langle u_i u_j \rangle}{\partial x_j}. \tag{2.12}$$

The tensor $\langle u_i u_j \rangle$ is called Reynolds stress tensor and plays an important role because it is the only term that distinguishes the momentum equations of the mean velocity field and the instantaneous velocity field. The term represents the transport of momentum due to turbulent velocity fluctuations.

The distribution of kinetic energy is an important characteristic of turbulence. As already explained, the instantaneous velocity field can be decomposed into the sum of a mean velocity field and a fluctuating velocity field. Similarly, the total kinetic energy contained in the instantaneous velocity field can be decomposed into mean kinetic energy and turbulent kinetic energy, according to

$$\frac{1}{2}\langle U_i^2 \rangle = \frac{1}{2}\langle U_i \rangle^2 + \frac{1}{2}\langle u_i^2 \rangle. \tag{2.13}$$

Multiplying the Reynolds-averaged Navier-Stokes equations, Eq. 2.12, by the mean velocity vector, $\langle U_i \rangle$, and then summing over i, we get the mean kinetic energy equation

$$\begin{aligned}\frac{\mathrm{D}}{\mathrm{D}t}\left(\frac{1}{2}\langle U_i \rangle^2\right) &= \frac{\partial}{\partial x_j}\left(-\frac{\langle P \rangle \langle U_j \rangle}{\rho} + 2\nu \langle U_i \rangle \langle S_{ij} \rangle - \langle u_i u_j \rangle \langle U_i \rangle\right) \\ &\quad -2\nu \langle S_{ij} \rangle \langle S_{ij} \rangle + \langle u_i u_j \rangle \frac{\partial \langle U_i \rangle}{\partial x_j},\end{aligned} \tag{2.14}$$

where S_{ij} is the mean strain rate, defined as

$$S_{ij} = \frac{1}{2}\left(\frac{\partial\langle U_i\rangle}{\partial x_j} + \frac{\partial\langle U_j\rangle}{\partial x_i}\right). \tag{2.15}$$

The substantial derivative on the left side of Eq. 2.14 is the rate of change of mean kinetic energy. The first three terms on the right are transport terms, which essentially redistribute the mean kinetic energy within the mean velocity field, without changing the total amount. The fourth term on the right represents viscous dissipation directly from the mean flow, i.e. the generation of heat. Because the mean velocity gradients are mild, direct viscous dissipation is usually very small for the mean flow and can be neglected. The fifth term also represents a loss of mean kinetic energy, but to the fluctuating velocity field. This terms reappears as a source term in the turbulent kinetic energy equation.

The turbulent kinetic energy equation is obtained by subtracting the Reynolds-averaged Navier-Stokes equations (Eq. 2.12) from the instantaneous Navier-Stokes equations (Eq. 2.2), multiplying by the fluctuating velocity vector, u_i, and then Reynolds-averaging. Hence, the turbulent kinetic energy equation is

$$\begin{aligned} \frac{\mathrm{D}}{\mathrm{D}t}\left(\frac{1}{2}\langle u_i^2\rangle\right) &= -\frac{\partial}{\partial x_j}\left(-\frac{1}{\rho}\langle p u_j\rangle + \frac{1}{2}\langle u_i^2 u_j\rangle - 2\nu\langle u_i s_{ij}\rangle\right) \\ &\quad -\langle u_i u_j\rangle\frac{\partial\langle U_i\rangle}{\partial x_j} - 2\nu\langle s_{ij}s_{ij}\rangle, \end{aligned} \tag{2.16}$$

where s_{ij} is the strain rate of the fluctuating field, given by

$$s_{ij} = \frac{1}{2}\left(\frac{\partial u_i}{\partial x_j} + \frac{\partial u_j}{\partial x_i}\right). \tag{2.17}$$

The substantial derivative on the left side of Eq. 2.16 is the rate of change of turbulent kinetic energy. Again, the first three terms on the right are transport terms, and only redistribute without generating or dissipating the turbulent kinetic energy. The fourth term is called turbulence shear production. This term corresponds to the transfer of kinetic energy from the mean flow to the fluctuating flow and appears with opposite sign in the mean kinetic energy equation as discussed above. The fifth term is the viscous dissipation of turbulent kinetic energy. Unlike its equivalent in the mean kinetic energy equation, this term is not negligible, but rather represents a *vital* feature of turbulence. It is called the dissipation rate and is denoted by ϵ.

A phenomenological description of the turbulence cascade was given by Richardson (1922). The mechanism of turbulence production withdraws energy from the mean flow and generates eddies of the size l, which is usually slightly smaller than the characteristic width of the mean shear flow, e.g. the diameter of Reynolds' pipe. These large eddies contain the bulk of the turbulent kinetic energy. Due to a high Reynolds number (based on their characteristic sizes, l, and characteristic velocities, which may be estimated as the rms fluctuating velocity, u'), the large-scale eddies become unstable and break down into smaller eddies. The somewhat smaller eddies ultimately become unstable themselves and break down into even smaller eddies. The turbulent kinetic energy therefore cascades from large to small eddies in a series of small steps. This breakdown process is called vortex tilting and stretching and results from the nonlinear terms in the equations of motion. The process is essentially inviscid, which means that virtually no turbulent kinetic energy is dissipated during the cascade to smaller scales. The incessant stretching generates continuously longer and thinner vortex filaments, with ever increasing velocity gradients. Eventually, the characteristic Reynolds number of the eddies becomes small enough that the steep velocity gradients are rapidly smeared out (i.e. dissipated) by molecular viscosity.

Viscous dissipation occurs at the smallest scales of the velocity field. However, the rate of dissipation is determined by the first process in the sequence, i.e. the breakdown of the largest eddies. The kinetic energy contained in the largest eddies is of the order of u'^2, and their characteristic turnover frequency is u'/l. Observations reveal that these eddies usually break down after one or two turnovers. The rate at which they transfer turbulent kinetic energy to the next smaller scales, and consequently the dissipation rate, must then be of the order of

$$\epsilon \sim \frac{u'^3}{l}. \tag{2.18}$$

Kolmogorov (1941) argued that the size of the smallest eddies only depends on the dissipation rate, ϵ, and the kinematic viscosity, ν. Dimensional reasoning yields an estimate for the length scale of the smallest eddies of

$$\eta = \left(\frac{\nu^3}{\epsilon}\right)^{1/4}, \tag{2.19}$$

which is called the Kolmogorov length scale, and marks the lower limit of the range of scales in the velocity field. Furthermore, Kolmogorov suggested that the anisotropy of the largest eddies, which is imposed by the boundary conditions of the mean flow, is lost during the cascade towards smaller eddies. Therefore, at scales, λ, significantly smaller than the largest scales of the flow (i.e. $\lambda \ll l$), the eddies become universal and isotropic. This range of scales is called the universal equilibrium range, and extends down to the smallest scales. For high Reynolds numbers, the largest and the smallest scales are separated by a large range. In the middle of the range, i.e. for $l \gg \lambda \gg \eta$, viscosity does not play a role and therefore the statistics at these scales are only a function of the scale, λ, and the dissipation rate, ϵ. This range is commonly referred to as inertial subrange.

Kolmogorov considered the energy cascade in spectral space rather than in physical space. Each length scale, λ, in physical space is related to a wavenumber, $k = 1/\lambda$, in spectral space. From dimensional reasoning, the energy spectrum, $E(k)$, in the inertial subrange (i.e. $\frac{1}{l} \ll k \ll \frac{1}{\eta}$) is given by the power-law

$$E(k) \propto \epsilon^{2/3} k^{-5/3}. \tag{2.20}$$

This power-law has been verified experimentally, and emphasizes the self-similar character of the eddies in spectral space.

2.1.5 Scalar field and turbulent mixing

Passive scalars in general are quantities that do not interfere with the dynamics of a flow. The concentration of the dye in Reynolds' pipe flow experiment is one example of a passive scalar. Other examples for passive scalar quantities are small temperature or density fluctuations, or the concentration of any passive conserved solute, e.g. salinity in the ocean.

Kolmogorov's phenomenological theory for the velocity field was adapted to turbulent passive scalar fields by Obukhov (1949), Corrsin (1951), and Batchelor (1959). In analogy to the total kinetic energy of the velocity field (Eq. 2.13), the quantity $\langle C^2 \rangle$ can be decomposed into a mean and a fluctuation, according to

$$\langle C^2 \rangle = \langle C \rangle^2 + \langle c^2 \rangle. \tag{2.21}$$

The scalar variance, $\langle c^2 \rangle$, can be interpreted physically as a measure for the deficiency of entropy of the fluid relative to the state in which the concentration is uniform, with the same mean value. The two main transport mechanisms for the concentration field are advection by the fluid motion and molecular diffusion. Advection essentially consists of the irregular stirring action of turbulence. The stirring distorts initially smooth filaments of dye, convoluting them at ever finer scales, and thereby increasing the magnitude of the concentration gradients.

This process represents a cascade of scalar variance, analogous to the cascade of kinetic energy explained in the previous section. The characteristic scales in the scalar variance cascade depend on the ratio of the diffusivities of momentum and the scalar, i.e. the Schmidt number, $\mathrm{Sc} = \nu/\kappa$. A rough estimate for the scale at which scalar fluctuations are dissipated by molecular diffusion (which can be obtained in analogy to the Kolmogorov scale) is called the Batchelor scale,

$$\eta_B = \left(\frac{\nu \kappa^2}{\epsilon} \right)^{1/4} = \eta \mathrm{Sc}^{-1/2}. \tag{2.22}$$

The rate at which the scalar variance is dissipated at the Batchelor scale is given by $\chi = 2\kappa \langle (\partial c/\partial x_i)^2 \rangle$, and corresponds to the dissipation rate, ϵ, for the velocity field. For the case of a dye mixing in water, the Schmidt number is rather high (roughly around 1000), and the scalar field extends to much smaller scales than the velocity field.

The scalar variance cascade, for high Reynolds numbers, can be subdivided into four distinct scale ranges. Equivalent to the velocity field, the bulk of the turbulent scalar variance is contained in the largest scales of the flow, i.e. at $\lambda \approx l$. In the inertial-convective range, $l \gg \lambda \gg \eta$, the statistics of the scalar quantity only depend on the rates of dissipation of turbulent kinetic energy, ϵ, and turbulent scalar variance, χ. Again from dimensional reasoning, the scalar spectrum, $\Gamma(k)$, in the inertial-convective range (i.e. $\frac{1}{l} \ll k \ll \frac{1}{\eta}$) is given by the power-law

$$\Gamma(k) \propto \chi \epsilon^{-1/3} k^{-5/3}. \tag{2.23}$$

Beyond the Kolmogorov scale, there is a range, $\eta \gg \lambda \gg \eta_B$, where the statistics of the scalar quantity are a function of χ alone, called viscous-convective range. For $\frac{1}{\eta} \ll k \ll \frac{1}{\eta_B}$, the scalar spectrum takes the form

$$\Gamma(k) \propto \chi k^{-1}. \tag{2.24}$$

The power-law behavior of the scalar spectrum implies that the concentration field exhibits self-similar properties in spectral space, in analogy with the velocity field. Finally, in the viscous-diffusive range ($\lambda \approx \eta_B$), the molecular diffusion dominates the scalar statistics.

The molecular flux per unit area that ultimately smears out the gradients of the scalar quantity is governed by Fick's law,

$$q_i = -\kappa \frac{\partial C}{\partial x_i}. \tag{2.25}$$

The total molecular flux and rate of homogenization therefore closely depend on the surface area across which the molecular flux is occurring. Turbulent stirring effectively increases the surface area of an initially smooth dye filament. The total diffusive flux is therefore enhanced by the increased surface area between concentration filaments and unmixed fluid.

For a quantitative description of the surface area characteristics of turbulence, it is necessary to define fluid interfaces precisely. An easy and effective way to characterize interfaces in a scalar field is to set a threshold on the scalar quantity. For the example of a concentration field, one can define concentration iso-surfaces according to

$$C(x_i, t) = C_{th} = \text{const.} \tag{2.26}$$

By varying the threshold, the concentration iso-surfaces can be adapted to represent for example the interface between mixed fluid and pure ambient fluid or a particular species concentration that may be of interest in a chemical reaction. Iso-surfaces in a three-dimensional turbulent scalar field are generally two-dimensional surfaces, evolving in space and time, with varying degrees of convolutedness at scales between the integral scale, l, and the Batchelor scale, η_B.

The Reynolds number is known to have significant impact on the characteristic properties of the mixing process. Not only does it trigger the transition from laminar to turbulent flow (see Sec. 2.1.1), it also controls changes in flow properties within the turbulent regime. By reviewing a variety of flow types, such as shear layers, jets, pipe flows, and boundary layers, Dimotakis (2000) identified a universal change in a number of turbulent mixing characteristics to occur at $\mathrm{Re}_{min} \approx 10^4$. For $\mathrm{Re} < \mathrm{Re}_{min}$, one usually observes a significant Reynolds number dependence of many different mixing parameters, while for $\mathrm{Re} > \mathrm{Re}_{min}$, the Reynolds number dependence is much weaker. Most conspicuously, there is a qualitative change in the appearance of the scalar field. A rather distinct transition takes place towards a more well-mixed state, with lower scalar gradients and a larger fraction of the flow field being occupied by fluid with intermediate concentration. The occurrence of this mixing transition, and the transition Reynolds number seem to be independent of the particular flow geometry. However, the sharpness of the transition does vary for different flow types.

2.1.6 Turbulent boundary layers

The information in the previous sections regards turbulent flows in general. The flow geometry for the present study is a turbulent boundary layer over a flat, smooth wall. The mean and fluctuating velocity fields in a turbulent boundary layer have distinct characteristics, some of them being significantly different from other flow geometries such as turbulent jets. Therefore, it is necessary to discuss this particular flow type in more detail.

A turbulent boundary layer can be subdivided into an inner region, which is dominated by the viscous effects of the wall, and an outer region, where direct effects of viscosity are negligible. The universal characteristics of the mean velocity profile are revealed by use of the proper length and velocity scales. The characteristic length scale in the inner region is the viscous scale,

$$\delta_\nu = \nu / u_\tau, \tag{2.27}$$

where the wall friction velocity is defined by

$$u_\tau \equiv \sqrt{\tau_w / \rho}, \tag{2.28}$$

where τ_w is the wall shear stress, and ρ is the density of the fluid. The viscous length scale properly normalizes the distance from the wall, which is normally referred to as wall units,

$$z^+ \equiv y u_\tau / \nu. \tag{2.29}$$

In the outer region, the characteristic length scale is the boundary layer thickness, δ, which also normalizes the distance from the wall.

Across the inner and outer region of a turbulent boundary layer, various layers can be identified in terms of mean velocity profiles. Starting at the wall and going outwards, we have the viscous sublayer, the buffer layer, the logarithmic layer (which is also called inertial layer), and the defect layer. The location of the viscous sublayer, expressed in wall units, is given by $y^+ < 5$. The Reynolds shear stress is negligible compared to the viscous stress due to the proximity of the wall. Therefore, the flow in the viscous sublayer can be considered to be laminar, and the transport of momentum and scalar quantities perpendicular to the wall is rather small. Because the viscous sublayer is very thin, the shear stress across the viscous sublayer is constant and equal to the wall shear stress. Using that assumption, the mean velocity in the viscous sublayer is given by

$$u^+ \equiv \frac{\langle U \rangle}{u_\tau} = y^+. \tag{2.30}$$

The buffer layer, located at $5 < y^+ < 30$, is the transition region between the viscosity-dominated and the turbulence-dominated parts of the boundary layer. The shear production and turbulence intensity peak in the buffer layer, causing strong fluctuating velocity and scalar fields and rapid mixing. The mean velocity profile is characterized by an asymptotic transition from the viscous sublayer profile to the profile of the logarithmic layer.

In the logarithmic layer, extending from $y^+ > 30$ to $y/\delta < 0.2$, the mean velocity profile follows the logarithmic law

$$u^+ = \frac{1}{k} \ln y^+ + B_1, \tag{2.31}$$

with the von Karman constant $k \approx 0.41$ and $B_1 \approx 5.2$. Obviously, the logarithmic layer crosses the boundary between inner and outer regions, and the logarithmic law can be expressed equally well by a velocity defect law compared to the free stream velocity outside the boundary layer, U_0, and in terms of length scales that are normalized by the boundary layer thickness, δ, i.e.

$$\frac{U_0 - \langle U \rangle}{u_\tau} = -\frac{1}{k} \ln \frac{y}{\delta} + B_2, \tag{2.32}$$

where $B_2 \approx 0.7$.

For $y/\delta > 0.2$, called the defect layer, the mean velocity deviates slightly from the logarithmic law, according to

$$\frac{U_0 - \langle U \rangle}{u_\tau} = \frac{1}{\kappa} \left\{ -\ln\left(\frac{y}{\delta_\nu}\right) + \Pi \left[2 - 2\sin^2\left(\frac{\pi}{2}\frac{y}{\delta}\right) \right] \right\}. \tag{2.33}$$

The wake strength parameter, Π, is flow dependent, but its exact value is controversial in the basic turbulence literature.

2.1.7 The concentration field of a continuous point source

This section describes the characteristics of the concentration field, i.e. of a plume arising from an iso-kinetic, continuous point source in a turbulent boundary layer (see e.g. Roberts and Webster, 2002). A coordinate system is defined by the streamwise coordinate x, and the vertical coordinate z, with the origin at the plume source location.

Consider the case of a uniform concentration of dye released continuously from a point source. While the mean flow advects the dye downstream, turbulence produced in the boundary layer mixes and spreads the plume. Larger turbulent eddies transport dye filaments away from the centerline, and smaller eddies distort the dye filaments, resulting in high concentration gradients on which molecular diffusion acts. Thereby, the vertical location of the source within the boundary layer is of importance because it determines the mean velocity, the turbulence intensity, and the size of the largest eddies. The instantaneous concentration field created by the different transport mechanisms is characterized by a high degree of inhomogeneity and intermittency, both in space and time (e.g. Webster et al., 2003). Large areas of low concentration (close to zero) are sporadically interrupted by local filaments of high concentration. The peak concentrations are separated by steep gradients and are typically much higher than the mean concentrations. In addition, the peak concentrations can be encountered even far off the centerline of the plume. The magnitude of the instantaneous peaks drops dramatically with streamwise distance from the source, and the concentration field appears more homogenous. However, even far downstream, the concentration field remains unpredictable.

For a uniform flow, a theoretical model for the mean concentration field of a continuous point source release can be formed if the eddy diffusion coefficient, κ_T, is assumed to be constant. In this model, the eddy diffusion coefficient is assumed to be equal in the vertical and transverse directions, and independent of x. In reality, κ_T is likely to change with location and direction within the field. In addition, diffusion in the streamwise direction is neglected, due to relatively small concentration gradients in this direction. Thus, the model is only valid far away from the source, for $x \gg 2\kappa/\langle U\rangle$. Under these assumptions, the mean concentration field can be derived from the scalar evolution equation, Eq. 2.3, to be

$$\langle C(x,y,z)\rangle = \frac{\dot{m}_{source}}{4\pi\kappa_T x}\exp\left(-\frac{(y^2+z^2)\langle U\rangle}{4\kappa_T x}\right), \tag{2.34}$$

where $\dot{m}_{source}$ is the mass flow rate of the passive scalar from the source, and $\langle U\rangle$ is the uniform flow velocity. Strictly, Eq. 2.34 only holds for unbounded flows, where the effects of walls and free surfaces on the plume are negligible.

From the model, we can observe several characteristics of the mean concentration field. The mean concentration is maximal at the centerline. Off the centerline, the mean concentration is symmetrical and follows a Gaussian profile. With increasing streamwise distance from the source, the mean concentration on the centerline attenuates in proportion with x^{-1} and the cross-stream Gaussian profile spreads out. The cross-stream extent of the mean concentration field can be quantified, for example, in terms of the locations at which the mean concentration is one percent of the centerline concentration. Using that definition, the cross-stream extent of the concentration field spreads in proportion with $x^{-1/2}$. Thus, the plume's cross-sectional area increases in proportion with x.

The fluctuating concentration field can be described in terms of the standard deviation of the concentration fluctuations (Webster et al., 2003). However, compared to the mean concentration field, it is more difficult to predict theoretically. Qualitatively, the standard deviation behaves similar to the mean concentration. On the centerline, the fluctuations decay faster with x than the mean, indicating that the plume is becoming homogenous faster than it is diluting. In the cross-stream directions, the fluctuations decrease with distance from the centerline. However, the profiles of the standard deviation become flatter with increasing x, i.e. the fluctuations spread in the cross-stream directions.

2.2 Fractal geometry

2.2.1 Conceptual introduction

Iso-surfaces in a turbulent passive scalar field are folded and wrinkled at a wide range of scales. Since the work of Richardson (1961) on the length of coastlines and borderlines, it is known that the geometrical description of complex and convoluted objects is not a trivial task. To understand the underlying problem, consider a classical example given by Mandelbrot (1967), and in more detail (1982): How long is the coast of Britain? Measuring the length of an object always necessitates the arbitrary definition of a reference length, which we call a yardstick. The length of the object, L, is then measured by counting the number of yardsticks, N, that are required to cover the object, and multiplying that number by the reference length, λ, of the yardstick, i.e.

$$L = \lambda N. \tag{2.35}$$

For a straight line, the result does not depend on the defined size of the yardstick, which means if we re-define the yardstick to half of its original size, we simply need twice as many yardsticks to cover the straight line. For other Euclidean objects such as a circle, the measured length changes with yardstick size if the yardstick and object have approximately the same size, but the length quickly tends towards a constant value as the yardstick gets smaller. For a complex object such as Britain's coastline, however, different yardstick sizes never yield the same result. In fact, as we decrease the size of the yardstick, the length of the coastline grows without bound. The reason for that surprising phenomenon lies in the large hierarchy of scales that are contained in a coastline. A yardstick of the order of kilometers only resolves the largest bays and peninsulas, whereas if we downsize the yardstick, ever-smaller coastal structures are taken into account: river mouths, tiny spits of land, and finally rocks, stones, and sand. This effect leads to the conclusion that for coastlines, the length alone (i.e. without the corresponding yardstick size) is an arbitrary, and thus a useless measure.

2.2.2 Levels of geometrical complexity

Problems similar to those observed in the measurement of coastline lengths are encountered in many scientific fields that involve the geometrical description of complex and convoluted objects. Catrakis (2000) provides an example list including lung tissue, topographic surfaces, solar granulation, and galaxy distribution in the universe. These and other examples indicate that classical Euclidean geometry may be an insufficient tool for many applications. In order to retain the connection to the length scaling in our coastline example, the discussion will be restricted initially to convoluted curves that are embedded in a plane. Complex structures of different dimensionality will be discussed subsequently.

Euclidean objects, such as a circle, have structure at a single, large scale only. As already mentioned, the unique length of such simple objects is readily determined by means of a yardstick of arbitrary, but significantly smaller size than the object itself.

More complex objects have structure at a large range of scales, and therefore it is difficult to assign a unique length to them. In this case, we need to look for a more general measure that contains information about the length-scaling behavior at various yardstick sizes. Richardson (1961) found that the length of coastlines, L, can be represented by a power-law function of the yardstick size, λ, as expressed in

$$L(\lambda) = \lambda N(\lambda) \propto \lambda^{1-D}. \tag{2.36}$$

In other words, his log-log plots of coastline length versus yardstick size consisted of straight lines, over a large range of scales, with the exponent, D, being the negative slope of the lines. Mandelbrot (1967) realized that this exponent represents a convenient measure for a complete description of the length-scaling behavior of a complex object. As D is generally a non-integer, he coined the name "fractal dimension". The fact that Richardson (1961) found the fractal dimension of coastlines to be a constant indicates that the coastline is self-similar, i.e. exhibits the same structural complexity over a wide range of scales.

It may be anticipated, and confirmed in nature, that such *exactly* self-similar objects are exceptions, and in general, objects can have different geometrical complexity at different scales. For the coastline, this means that larger bays and peninsulas may look quite smooth while smaller bays and peninsulas are very rugged, or vice versa. In that case, a simple power-law is no longer sufficient to describe the length-scaling behavior. In particular, the fractal dimension is not a constant, but a function of scale, i.e. $D = D(\lambda)$, and therefore $L(\lambda) = \lambda N(\lambda) \not\propto \lambda^{1-D(\lambda)}$. Instead, the length-scaling is given by the more general, non-power-law expression

$$L(\lambda) = \lambda N(\lambda) \propto \lambda \exp\left\{ \int_{\lambda}^{\infty} D(\tilde{\lambda}) \frac{\mathrm{d}\tilde{\lambda}}{\tilde{\lambda}} \right\}. \tag{2.37}$$

From the considerations above, Catrakis (2000) suggested a three-level hierarchy of complexity:

- Level 1: complexity only at a single scale - Euclidean geometry.
- Level 2: complexity is the same at all scales - power-law geometry.
- Level 3: complexity varies with scale - scale-dependent geometry.

2.2.3 Embedding dimension and topological dimension

The fractal dimension is generally a non-integer and is always bounded between the topological dimension, d_t, and the embedding dimension, d, of the object, i.e.

$$d_t \leq D \leq d. \tag{2.38}$$

In fact, Mandelbrot (1982) defined fractals as geometrical sets that have a fractal dimension larger than the topological dimension. The topological dimension, d_t, is defined as the number of independent variables that are required to describe the neighborhood of any of an object's points. Thus, we have a topological dimension of 0 for points, 1 for curves (e.g. circles), and 2 surfaces (e.g. hollow spheres). Obviously, d_t is always integer-valued. The embedding dimension, d, of a set is the smallest integer for which the set can be embedded in d-dimensional space (i.e. $\mathbb{R}^d$) without intersecting itself. For example, the embedding dimension is 1 for a set of points, arranged on a straight line, 2 for a circle, and 3 for a hollow sphere.

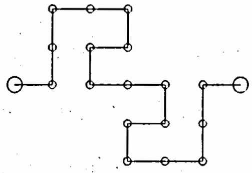

Figure 2.1: Generator for the contiguous $D = 1.6131$ Koch curve.

2.2.4 Deterministic self-similar fractals vs. natural objects

Ideal models are often useful in understanding the essential features of a theory. In the case of fractal geometry (or more precisely: Level 2 complexity, as initially considered by Mandelbrot, 1982), such idealizations are deterministic self-similar fractals (Sreenivasan, 1991).

Deterministic self-similar fractals are created by performing the same prescribed operation (called the "generator") repeatedly on a starting object (called the "initiator"), which may be rather simple. For these theoretical objects, it is important to realize that "the same prescribed operation" means "exactly the same", and that "repeatedly" shall imply "ad infinitum". Among the most commonly known examples are the Koch curves and the Cantor dust (see e.g. Mandelbrot, 1982, for a detailed description). In particular, let us study the contiguous quadric Koch curve with a fractal dimension of $D = \log_{10} 18/\log_{10} 6 \approx 1.6131$ (in the following, we will give approximate values of fractal dimensions with an accuracy of 5 digits, and drop the approximate sign). The generator is shown in Fig. 2.1. A square is used as the initiator, which is the zeroth step of the self-similar cascade. During the first step, all four straight line segments of the initiator square are replaced by the generator, such that the start and end points of the generator (indicated by larger circles in Fig. 2.1) are placed at the start and end points of each replaced straight line segment. During the second step, all straight line segments of the first step are replaced by the generator, and so on. Obviously, the generator has to be downsized from step to step. For the particular generator in Fig. 2.1, all line segments of the previous step are subdivided into $b = 6$ fractions of length $r = 1/b = 1/6$, hence creating a grid for the $M = 18$ new lines of the generator. If the lines of the initiator have unity length, the generator of the pth step of the cascade has a length of r^{-p}. The fractal dimension of such Level 2 complex curves is entirely determined by their generator, and can be calculated from

$$D = \frac{\log_{10} M}{\log_{10}(1/r)}. \tag{2.39}$$

Fig. 2.2 shows the initiator and the first three steps of the self-similar cascade of this Koch curve. As can be seen, the range of scales at which the curve is convoluted consecutively expands during each step towards increasingly small scales. After a very large number of cascade steps, the area enclosed by the curve goes to a finite value, whereas the length of the curve tends towards infinity. In this sense, the Koch curve could be viewed as the plane transect of a concentration iso-surface of an initially smooth blob of dye that is injected into a turbulent flow field. The turbulent eddies contort the shape of the blob, significantly increasing the size of the surface across which molecular mixing takes place. Alternatively, the Koch curve could represent the coastline of an island, with a large variety of differently-sized bays and peninsulas, and a coastline length that increases infinitely with decreasing yardstick size.

In either case, however, the Koch curve appears too regular and symmetrical to be a real dye filament or geographical island. In other words, the application of *exactly* the same generator during the whole cascade represents the key difference to most natural objects. In fact, a precisely repeated scale similarity seems unlikely in turbulent flows (Frederiksen et al., 1996), and complex phenomena in nature are expected to exhibit statistical self-similarity instead (Catrakis, 2000). For the coastline, this implies that the exact shape may vary among single bays and peninsulas of the same size as well as between differently-sized ones. As a results, the fractal dimension of statistical self-similar curves may fluctuate in a random manner, in contrast to every (arbitrarily small) fraction of a deterministic self-similar fractal curve, which shows the same length-scaling behavior and thus the same fractal dimension. It is therefore necessary to consider sufficiently long coastlines or, equivalently, a sufficiently

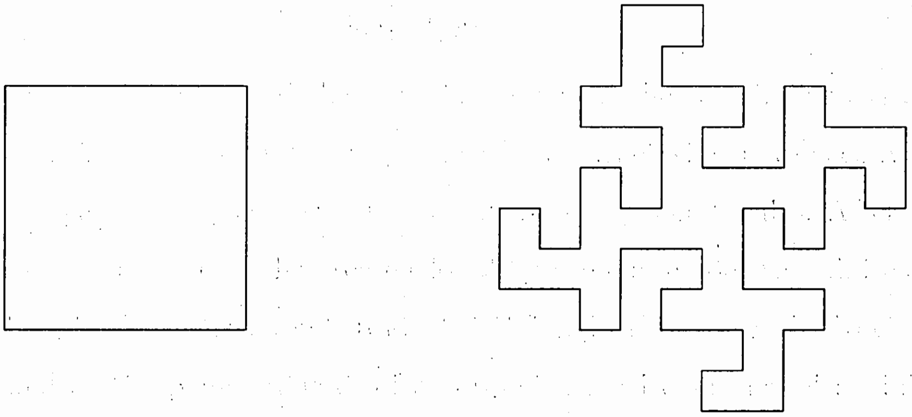

(a) Step 0. (b) Step 1.

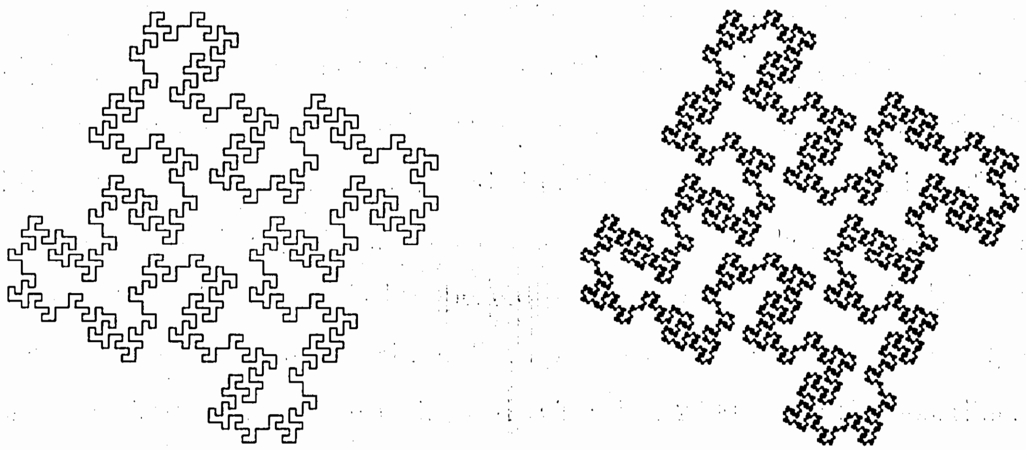

(c) Step 2. (d) Step 3.

Figure 2.2: Initiator (a) and first three steps (b) - (d) of the self-similar cascade for the contiguous $D = 1.6131$ Koch curve.

large number of individual concentration iso-surfaces, and to perform an ensemble-averaging to extract statistically converged fractal measures.

2.2.5 The fractal dimension in theory and practice

While Eq. 2.39 gives the fractal dimension of a few particular objects, we need to define the fractal dimension in a more general way that is applicable to a large variety of objects. As described by Mandelbrot (1982), let us consider some object in $\mathbb{R}^3$, with unknown dimensionality and level of complexity. Similar to the calculation of the length by means of the yardstick in the coastline example, one can quantify the volume, for example, of the object by completely covering it with spheres, counting the number of spheres, and multiplying that number by the volume of the spheres. Because the dimensionality of the object is unknown, we introduce *generalized* spheres of dimension d, which, for integer values of d, can be spheres, circles, or yardsticks. The generalized volume of such spheres of radius λ is given by the Hausdorff measure,

$$h(\lambda) = \gamma(d)\lambda^d, \tag{2.40}$$

where the function

$$\gamma(d) = \frac{\Gamma(\frac{1}{2})^d}{\Gamma(1+\frac{d}{2})} \tag{2.41}$$

represents the generalized volume of a d-dimensional unity sphere, and Γ is the Gamma function. For Euclidean spheres, this function yields $\gamma(3) = \frac{4}{3}\pi$, $\gamma(2) = \pi$, $\gamma(1) = 2$.

More generally, d can have non-integer values to cover objects of higher complexity. All of the definitions retain their validity for that generalization. The generalized d-dimensional volume of the object can be expressed by the sum over all of the spheres that are used to cover the object, i.e. $\sum h(\lambda)$. We want to consider the most economic coverage of the object, and therefore we allow the spheres to have different radii λ_m, which are smaller or equal to the considered radius λ. The most economic coverage is realized by taking the infimum of the sum, i.e. $\inf_{\lambda_m<\lambda} \sum h(\lambda_m)$. For the sum to resolve all of the details of the object, the considered radius must be arbitrarily small, and therefore the generalized d-dimensional volume of the object is finally given by the expression

$$\lim_{\lambda \to 0} \inf_{\lambda_m < \lambda} \sum h(\lambda_m), \tag{2.42}$$

which is called the d-measure of the object. This measure has a positive and finite value only if the number $d \in \mathbb{R}$ is chosen to match the real dimensionality, D, of the considered object. If $d < D$, the d-measure goes to infinity, and for $d > D$, it goes to zero. Thus, D is a critical dimension and is called the Hausdorff-Besicovitch dimension. Mandelbrot (1982) named this dimension the "fractal dimension".

In practice, the numerical calculation of the Hausdorff-Besicovitch dimension would be quite cumbersome, to say the least. The largest difficulty results from the requirement of the most economic coverage by means of spheres of *arbitrary* size. In fact, all numerical methods applied in practice utilize spheres or other Euclidean objects of *constant* size. Most of these methods are based on the four strategies outlined in Mandelbrot (1982), for evaluating the length of coastlines. A comprehensive (though rather obsolete in terms of computational efficiency) summary of Mandelbrot's four strategies and the available numerical methods based on them, is given by Allen et al. (1995). They classify the numerous approaches into vector-based and matrix-based methods, which we will summarize for the case of fractal curves embedded in a plane. Vector-based methods, on the one hand, require a contour-following algorithm to step along the curve using distinct step sizes, analogous to a caliper. The number of required steps can be related to the length-scaling behavior of the curve and the fractal dimension, as shown in Sec. 2.2.2. There are several approaches of varying accuracy and computational efficiency, e.g. the EXACT, FAST, and HYBRID algorithms. Matrix-based methods, on the other hand, rely on the matrix or pixel structure in which digital data is usually represented. They essentially subdivide the whole field into equally-sized elements and count the number of elements that cover the curve. Again, this number can be related to length-scaling behavior and fractal dimension. Examples are the box-counting, distance-mapping, and erosion-dilatation logic algorithms.

Allen et al. (1995) identified the matrix-based methods to be less accurate than the vector-based methods. However, the former methods exhibit significant advantages compared to the latter ones: First, they do not require a complex contour-following algorithm. Second, because they inherently consider the entire image field, they are more adept in dealing with objects that consist of detached elements, such as coastlines with smaller islands in front of the coast (this issue is of great importance below in this section). Third, some of them employ subdividing grids that are based on the underlying pixel grid of a digital image, which further simplifies the algorithm.

The algorithm most applicable for our application is the box-counting algorithm, also called mosaic-amalgamation. It is by far the most commonly applied algorithm to determine fractal dimensions. Briefly, the algorithm subdivides the image field including the fractal object into boxes of consecutively smaller size. For each particular box size, λ, the number of boxes, $N(\lambda)$, that include parts of the fractal object is counted (more details are given in Sec. 3.2.5). The fractal dimension, which for Level 3 complex objects can be a function of scale, is then obtained from

$$D(\lambda) = -\frac{\mathrm{d}\log_{10} N(\lambda)}{\mathrm{d}\log_{10}\lambda}. \tag{2.43}$$

This dimension is also called the box-counting dimension, or coverage dimension. Although we consider it to be the fractal dimension, we must keep in mind that numerous simplifications were made in its definition compared to the Hausdorff-Besicovitch dimension. For example, boxes are used instead of isotropic spheres. Also, the boxes have constant size, and their size does not go to zero. As we will see, this may lead to slight deviations from the original Hausdorff-Besicovitch fractal dimension, even for deterministic self-similar fractal objects.

An important difference between the Hausdorff-Besicovitch dimension and the box-counting dimension becomes obvious when we consider objects that consist of numerous *detached* sub-objects. For the coastline example, we can think of islands in front of the coast and lakes in the hinterland. For concentration iso-surfaces, this corresponds to the presence of several individual filaments of dye within the concentration field. Because this property of an object, called "dispersion" by Mandelbrot

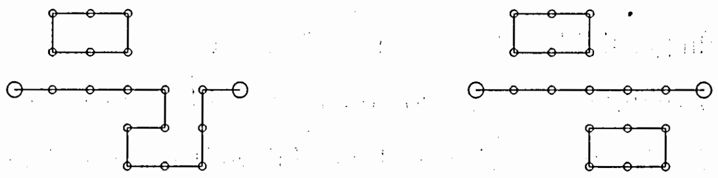

(a) Partially dispersed. (b) Fully dispersed.

Figure 2.3: Alternative generators for the $D = 1.6131$ Koch curve. (a) Smaller detached sub-islands form in front of the coast of the main island. (b) Smaller detached sub-islands and sub-lakes form in front and in the hinterland of the coastline, respectively.

(1982), is an essential feature of the concentration iso-surface fields considered in the present study, it is important to take a closer look at this issue. With a slight modification of the generator from Sec. 2.2.4 (Fig. 2.1), the Koch curve develops islands and lakes that are detached from the main coastline. An example for such a modified generator is shown in Fig. 2.3(a). The characteristic parameters of this generator are the same as in Fig. 2.1, i.e. $b = 6$, $r = 1/6$, and $M = 18$. However, only $M_C = 12$ line segments of the generator form the coastline (thus called coastline-generator), while $M - M_C = 6$ line segments create a detached sub-island in front of the coast (island-generator). The resulting fractal, for which the initiator and the first three levels of the self-similar cascade are shown in Fig. 2.4, now exhibits two different dimensions. If we take the cumulative coastline, i.e. the curves of all objects together, the resulting dimension is $D = \log_{10} M / \log_{10}(1/r) \approx 1.6131$, which is of course equal to the dimension of the fractal in Fig. 2.2. The dimension of the coastline for each individual island, however, is $D_C = \log_{10} M_C / \log_{10}(1/r) \approx 1.3869$, implying generally in $\mathbb{R}^d$ that

$$d_t \leq D_C \leq D. \tag{2.44}$$

An even more disperse generator is shown in Fig. 2.3(b) with the corresponding first three steps of the self-similar cascade shown in Fig. 2.5. Again, we have $b = 6$, $r = 1/6$, and $M = 18$, so that the cumulative fractal dimension, D, remains unchanged. However, the coastline-generator is characterized by $M_C = 6 = b$, and

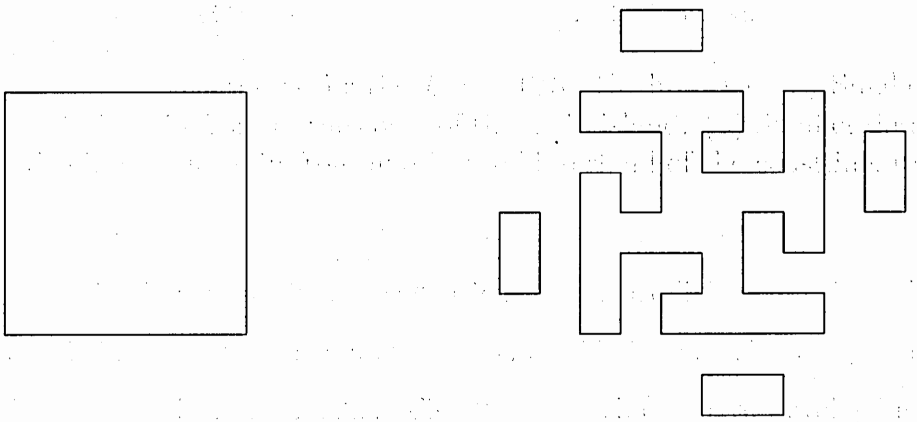

(a) Step 0.

(b) Step 1.

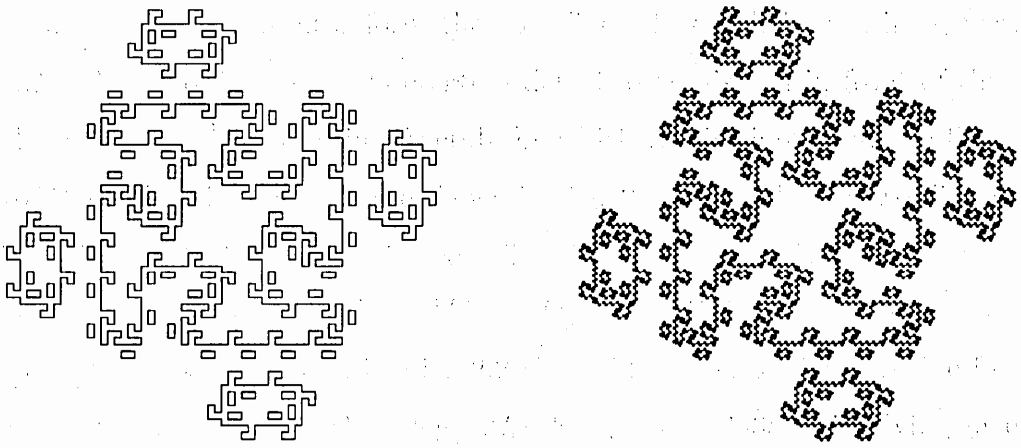

(c) Step 2.

(d) Step 3.

Figure 2.4: Initiator (a) and first three steps (b) - (d) of the self-similar cascade for the partially dispersed $D = 1.6131$ Koch curve (generator from Fig. 2.3(a)). The complexity of the curve arises from both its dispersion and convolution.

the individual coastline dimension takes the smallest possible value, i.e. $D_C = 1 = d_t$. Here, the coastline of each individual island is an Euclidean object, although the cumulative fractal dimension is larger than the topological dimension. This is a very important finding, as it implies that the fractal dimension, depending on its particular definition, considers both the convolution and dispersion. According to Mandelbrot (1982), D_C corresponds to the Hausdorff-Besicovitch dimension, while D is associated with the box-counting dimension. Thus, for the general case of $D_C > d_t$, the Hausdorff-Besicovitch dimension measures only the convolution of an object, while the box-counting dimension measures a combination of convolution and dispersion.

In turbulent mixing processes, we are interested in the scaling behavior of the total, i.e. cumulative, iso-surface area of all filaments of dye within the concentration field. In this respect, the box-counting dimension is more meaningful than the Hausdorff-Besicovitch dimension. In addition, the box-counting dimension is the easier algorithm to employ, thus it will be utilized in the present study.

2.2.6 Dimensional classification of concentration iso-surfaces

In contrast to the theoretically infinite range of scales of deterministic self-similar fractals, turbulent mixing exhibits a finite range of scales. As already explained in Sec. 2.1.5, the scales in a turbulent concentration field extend from the integral scale, l, to the Bachelor scale, η_B. Concentration iso-surfaces in turbulent flows are always three-dimensional (with an additional evolution in time). More precisely, they have an embedding dimension of $d = 3$. The iso-surfaces are dimensionally analogous to hollow spheres (although generally more convoluted), thus they have a topological dimension of $d_t = 2$. From the bounding condition, Eq. 2.38, and for scales smaller than the largest iso-surfaces, the fractal dimension of the concentration iso-surfaces is expected to be within $2 \leq D \leq 3$. Outside the scaling range the concentration field, the embedding dimension does not change because the dye distribution remains three-dimensional at scales at which no new structural convolution and complexity arises. The topological dimension does change, however. When observed at scales larger than the largest dye filaments, the concentration field looks like a cloud of points, and thus

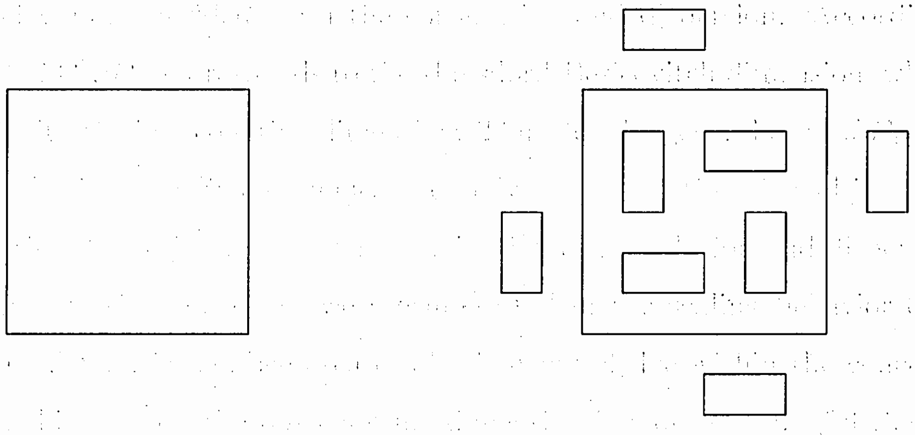

(a) Step 0. (b) Step 1.

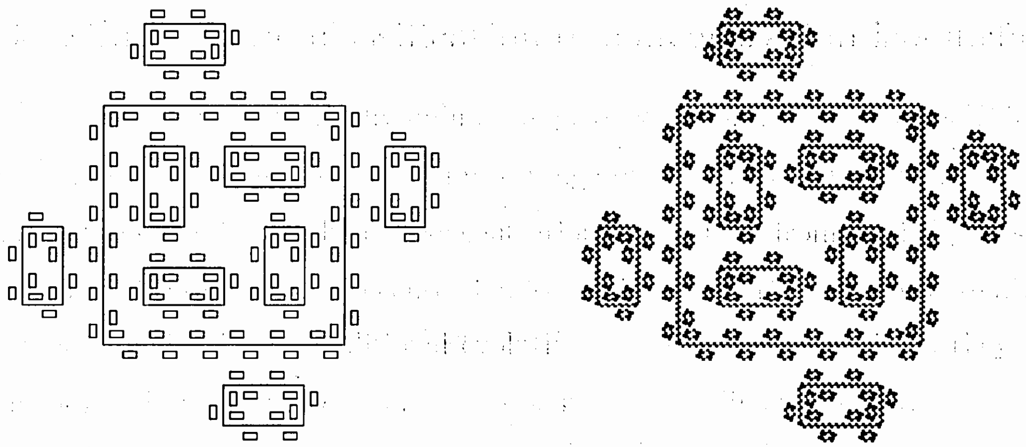

(c) Step 2. (d) Step 3.

Figure 2.5: Initiator (a) and first three steps (b) - (d) of the self-similar cascade for the fully dispersed $D = 1.6131$ Koch curve (generator from Fig. 2.3(b)). The curve exhibits smooth Euclidean coastlines, and the complexity arises solely from its dispersion.

the topological and fractal dimensions could be as low as zero, implying for arbitrary scales $0 \leq D \leq 3$. At scales smaller than the smallest convolution scale, the iso-surfaces appear smooth, like Euclidean objects, and therefore the fractal dimension tends towards the topological dimension, i.e. $D \rightarrow d_t$.

A proper resolution of the 4-D space-time evolution of concentration iso-surfaces, over the vast range of scales at high Reynolds numbers, requires a highly sophisticated experimental setup and huge amounts of data. For that reason, most of the investigations to date have been limited to lower-dimensional transects of the 4-D space-time evolution (cf. Catrakis and Bond, 2000). Most commonly, the experimental data consists of either single-point concentration time records, or time records of 2-D images of a plane in the flow field. In many cases, lower-dimensional spatial transects have been upgraded to higher-dimensional ones using the time coordinate and Taylor's frozen flow hypothesis. This hypothesis states that the mean flow simply advects the turbulent flow structure, without changing its characteristic properties over short time periods. Miller and Dimotakis (1991) and Frederiksen et al. (1996) used this hypothesis to obtain line transects of the concentration field from their single-point concentration time records. In that case, the concentration iso-surfaces are points (indicating threshold-crossings) on a straight line. Thus, the iso-surfaces have a topological dimension of $d_t = 0$ and an embedding dimension of $d = 1$, which limits their fractal dimension to $0 \leq D \leq 1$.

Two-dimensional images of the flow field have been used to obtain transects of varying dimensionality. Sreenivasan et al. (1989) and Catrakis and Dimotakis (1996), for example, used them to extract line transects of the concentration field, without using Taylor's hypothesis. Two-dimensional images are also used to directly extract planar transects of the concentration field. Here, concentration iso-surfaces are curves lying in the image plane, i.e. $d_t = 1$, $d = 2$, and $1 \leq D \leq 2$ for scales smaller than the largest iso-surfaces. Catrakis et al. (2002) used Taylor's hypothesis to obtain complete 3-D concentration iso-surfaces from their temporally resolved records of 2-D images of a fixed plane in the flow. Alternatively, Frederiksen et al. (1997) acquired 3-D concentration fields (without employing Taylor's hypothesis) by scanning a whole volume in the flow field and collecting a series of planar images. In both cases, as discussed above, the iso-surfaces are characterized by $d_t = 2$, $d = 3$, and $2 \leq D \leq 3$, again for scales smaller than the largest iso-surfaces. Remember that the topological dimension can be as low as zero for scales larger than the largest iso-surfaces. In both 3-D approaches, current experimental limitations become obvious, as Catrakis et al. (2002) "froze" the flow between consecutive images, but not over a whole sequence of images, and Frederiksen et al. (1997) were not able to resolve the finest scales of the concentration field.

In the present study, time records of 2-D images are used to extract concentration iso-surfaces in the form of curves within the image plane, yielding $d_t = 1$, $d = 2$, and $1 \leq D \leq 2$ for scales smaller than the largest iso-surfaces, but more generally (for all possible scales) $d_t \geq 0$, $d = 2$, and $0 \leq D \leq 2$. The images nearly resolve the Batchelor scale, but do not extend to the full size of the largest scales in the concentration field. In addition, the temporal resolution does not allow for an application of Taylor's hypothesis to get 3-D concentration iso-surfaces. For quantitative details of the experiment setup, including spatial and temporal resolutions, please refer to Sec. 3.1.

The essential question associated with lower-dimensional transects is: to what extent can the results be used to predict the fractal measures of the real 3-D concentration iso-surfaces? For deterministic fractal objects of Level 2 complexity, there exists a theorem that connects the fractal (Hausdorff-Besicovitch) dimension of the object to that of its lower-dimensional transects according to

$$D_{d+1} = D_d + 1, \tag{2.45}$$

where we use the common notation of indicating the embedding dimension as a subscript on the fractal dimension. The relation is known as the "additive law", and is discussed by Sreenivasan (1991), for example. It holds only if the intersecting transect is thinner than the smallest scales of the object, and if the transect dimension is independent of the orientation of the transect (i.e. if the object is isotropic). Despite these limitations, it has been applied extensively in the study of lower-dimensional transects of turbulent flow interfaces. However, as noted above, the concentration iso-surfaces may exhibit Level 3 complexity, with statistical self-similarity at only a finite range of scales. In addition, all practical work involves the box-counting (or coverage) dimension, instead of the Hausdorff-Besicovitch dimension, and an analogous theorem does not exist (Catrakis, 2000). Substantial deviations from the additive law have been reported for example by Catrakis and Bond (2000). They found that the scale-dependent coverage dimension of concentration iso-surfaces in the similarity plane of a turbulent round jet, at intermediate scales, is significantly larger for plane transects than for line transects, suggesting in general that

$$D_{d+1}(\lambda) > D_d(\lambda) + 1. \tag{2.46}$$

This was explained by the higher-dimensional transects capturing more iso-surface structure because there are more possible directions in which the local iso-surface varies. As a conclusion, lower-dimensional transects of three-dimensional concentration iso-surfaces tend to underestimate the space-filling properties of the iso-surfaces in general, and the fractal dimension in particular. Thus, the measures derived from lower-dimensional transects can be interpreted as a lower bound of the real measures.

2.2.7 Additional fractal measures for iso-surface description

The fractal dimension clearly plays the most important role in describing the geometrical properties of fractal objects in general and the concentration iso-surfaces in particular. Besides the fractal dimension, there exist a number of measures that provide additional, and more comprehensive insight into the characteristics of iso-surfaces. The framework of quantifying measures is usually called coverage statistics, and focuses on the space-filling properties and scale distributions. A valuable overview of the commonly utilized measures is given by Catrakis and Bond (2000). Here, we summarize the definitions and applications of the measures that will be applied in the present study. Although we will analyze 2-D images (i.e. embedding dimension $d = 2$), the framework of measures is presented more generally for an arbitrary d.

The basis for all measures is the coverage count, which is determined by means of the box-counting algorithm, as mentioned in Sec. 2.2.5, and described in detail in Sec. 3.2.5. In $\mathbb{R}^d$, it involves the subdivision of the δ_b^d-sized image field, called the bounding box, in $N_{d,tot}(\lambda)$ d-dimensional boxes (i.e. boxes in $\mathbb{R}^3$, squares in $\mathbb{R}^2$, and tiles in $\mathbb{R}$) of size λ^d, which is consecutively reduced in size. Ideally, the box size, λ, takes all values in the interval $0 < \lambda \leq \delta_b$. At each subdivision step, the number of boxes, $N_d(\lambda)$, that cover part of the fractal object is counted. The coverage count is bounded by $0 \leq N_d(\lambda) \leq N_{d,tot}(\lambda)$. From Eq. 2.37, the coverage count is related to the coverage dimension by the non-power law relationship

$$N_d(\lambda) = \exp\left\{\int_{\lambda}^{\delta_b} D_d(\tilde{\lambda})\frac{\mathrm{d}\tilde{\lambda}}{\tilde{\lambda}}\right\}, \tag{2.47}$$

which implies that the complexity of structures across a wide range of scales can contribute to the coverage behavior at any one scale λ.

The dimensionless coverage fraction, $F_d(\lambda)$, measures the degree to which the object fills space, and is defined as

$$F_d(\lambda) \equiv \frac{N_d(\lambda)}{N_{d,tot}(\lambda)} = \left(\frac{\lambda}{\delta_b}\right)^d N_d(\lambda), \tag{2.48}$$

such that $0 \leq F_d(\lambda) \leq 1$.

For $d = 2$ embedding space, a coverage length, $L_2(\lambda)$, as seen at yardstick size λ, is frequently used in the literature to quantify the surface-generation property of turbulent mixing. In $d = 3$ embedding space, this measure, $L_3(\lambda)$, corresponds to the surface area of the concentration iso-surfaces, as seen at tile size λ^2. For a general embedding space, the generalized coverage length is given by

$$L_d(\lambda) \equiv \lambda^{d_t} N_d(\lambda). \tag{2.49}$$

Obviously, structures of all scales larger or equal to λ contribute to the coverage length of the object. At the smallest scales of the scalar field (i.e. for $\lambda \rightarrow \eta_B$), this measure tends towards the total generalized coverage length, as the scalar interface cannot exhibit finer convolutions. Hence, the total generalized coverage length can be expressed as

$$L_{d,tot} = L_d(\lambda \rightarrow \eta_B). \tag{2.50}$$

For a statistical description or modeling of the object structure, it is useful to know the distribution of the scales involved in the structure. For $d = 1$ embedding space, a natural scale exists in the form of the distance between points of the object (i.e. locations of the threshold-level crossings). However, this scale does not generalize naturally to higher-dimensional embedding spaces $\mathbb{R}^d$. Therefore, the largest-empty-box (LEB) scale, λ, is defined as the size of the largest d-dimensional box, randomly located in the bounding box, that contains a randomly located point, but no part of the object. In other words, the LEB-scale is twice the distance from a randomly located point to the closest iso-surface structure. Besides evaluating a large number of random points, the LEB-scale PDF, $f(\lambda)$, can be derived from the coverage fraction:

$$f_d(\lambda) \equiv \frac{\mathrm{d}F_d(\lambda)}{\mathrm{d}\lambda}. \tag{2.51}$$

The LEB scale can also be interpreted as a measure of the distance from a random location within the bounding box to the nearest part of the object. It has been shown explicitly by Catrakis and Dimotakis (1996) that the LEB-scale PDF is related to the coverage dimension by the d-dimensional scale-distribution transform pair

$$\begin{aligned} D_d(\lambda) &= d - \frac{\lambda f_d(\lambda)}{\int_0^\lambda f_d(\tilde{\lambda})\mathrm{d}\tilde{\lambda}}, && (2.52)\\ f_d(\lambda) &= \frac{d - D_d(\lambda)}{\lambda} \exp\left\{ -\int_\lambda^{\delta_b} [d - D_d(\tilde{\lambda})] \frac{\mathrm{d}\tilde{\lambda}}{\tilde{\lambda}} \right\}. && (2.53) \end{aligned}$$

In order to quantify the interfacial area-volume behavior in $d = 3$ embedding space, Catrakis et al. (2002) proposed an area-volume ratio, $\Omega_3(\lambda)$, in terms of a box-counting measure of the interfacial area, $L_3(\lambda) = \lambda^2 N_3(\lambda)$, normalized by the volume of the bounding box, δ_b^3. This measure can be generalized to other embedding dimensions by replacing the measures for area and volume by the appropriate measures for the particular dimensionality, e.g. to get the length-area ratio for our $d = 2$ embedding space. In general, $\Omega_d(\lambda)$ is given by

$$\begin{aligned} \Omega_d(\lambda) &\equiv \frac{\lambda^{d_t} N_d(\lambda)}{(\delta_b^d)^{d_t/d}} = \left(\frac{\lambda}{\delta_b}\right)^{d_t} N_d(\lambda), && (2.54)\\ \alpha_\Omega(\lambda) &\equiv \frac{\mathrm{d}\log_{10}\Omega_d(\lambda)}{\mathrm{d}\log_{10}\lambda} = D_d(\lambda) - d_t, && (2.55) \end{aligned}$$

where α_Ω is the logarithmic derivative of the generalized area-volume ratio, and is related to the fractal dimension. $\Omega_d(\lambda)$ increases with decreasing scale, λ, tending towards the total area-volume ratio of the iso-surface, $\Omega_{d,tot}$, as λ approaches the smallest scales of the iso-surfaces. Its behavior therefore corresponds to the behavior of the coverage count (cf. Eq. 2.47 and related discussion), and one might suspect that $\Omega_d(\lambda)$, at a given scale, λ, is also sensitive to and influenced by all interfacial features above that scale.

This sensitivity raises an issue regarding the scale-local, as opposed to the scale-cumulative area-volume behavior. Thus, Catrakis et al. (2002) also introduced an area-volume density parameter, $g_3(\lambda)$, for $d = 3$ embedding space, as the scale-local contribution from the interfacial features in the differential scale range to the area-volume ratio. This scale-local quantity can be seen as the first-order term in a Taylor series for the area-volume ratio, i.e. in generalized form $\Omega_d(\lambda) \approx \Omega_d(\lambda{+}\mathrm{d}\lambda){+}g_d(\lambda)\mathrm{d}\lambda$. Thus, the generalized area-volume density, $g_d(\lambda)$, is given by

$$g_d(\lambda) \equiv -\frac{\mathrm{d}\Omega_d(\lambda)}{\mathrm{d}\lambda}, \tag{2.56}$$

$$\alpha_g(\lambda) \equiv -\frac{\mathrm{d}\log_{10} g_d(\lambda)}{\mathrm{d}\log_{10}\lambda}, \tag{2.57}$$

where $\alpha_g(\lambda)$ is the logarithmic derivative of the scale-local area-volume density, analogous to the definition of $\alpha_\Omega(\lambda)$. If $\alpha_g(\lambda) = \text{const.}$, then α_g can be interpreted as an area-volume density exponent with power-law scaling according to $g_d(\lambda) \propto \lambda^{-\alpha_g}$. In the more general case of a scale-dependent α_g, and for scales where $\alpha_g(\lambda) \geq 0$, it can be considered as a scale-local dimension.

By inverting Eq. 2.54 and using Eq. 2.56, Catrakis et al. (2002) showed explicitly for the $d = 3$ case that both the coverage dimension, $D_3(\lambda)$, and the area-volume ratio, $\Omega_3(\lambda)$, are scale-cumulative functions of the area-volume density, coupling iso-surface information from all scales larger or equal to λ:

$$\Omega_3(\lambda) = 1 + \int_\lambda^{\delta_b} g_3(\tilde{\lambda})\mathrm{d}\tilde{\lambda}, \tag{2.58}$$

$$D_3(\lambda) = 2 + \frac{\lambda g_3(\lambda)}{1 + \int_\lambda^{\delta_b} g_3(\tilde{\lambda})\mathrm{d}\tilde{\lambda}}. \tag{2.59}$$

These scale-cumulative measures are affected by contributions from the large scales of the flow. The large scales of the flow do not show self-similar properties in spectral space, and it may be anticipated that this is the case in physical space as well. The coverage dimension, $D_d(\lambda)$, has been employed extensively to evaluate self-similarity in turbulent passive scalar mixing (e.g. Sreenivasan, 1991; Frederiksen et al., 1996; Catrakis and Dimotakis, 1996; Villermaux and Innocenti, 1999). Equations 2.58 and 2.59 imply, however, that considering the coverage dimension alone is not sufficient to detect scale-local self-similarity. In other words, the large-scale influences included in the coverage dimension could mask self-similarity present at smaller scales. In contrast, the area-volume density and exponent enable a scale-local examination of the interfacial area-volume contributions and are expected to be particularly useful for determining the presence of self-similarity.

2.2.8 Fractal dimension of iso-surfaces in the literature

The fractal geometry of interfaces in turbulent flows has been investigated extensively since the fundamental suggestions of Mandelbrot (1975). Most of the work has focused on the fractal dimension as the significant measure, and turbulent round jets are the predominant flow type addressed in the literature. A common feature of virtually all experimental results is the difficulty in achieving a high Reynolds number while resolving the whole range of turbulent scales.

Sreenivasan and Meneveau (1986), Sreenivasan et al. (1989), and Sreenivasan (1991) examined concentration iso-surfaces for a variety of turbulent flows, namely a boundary layer, a round jet, a plane wake, and a plane mixing layer. Using 1-D and 2-D transects and 3-D data in conjunction with the additive law, they consistently found a constant fractal dimension of $D_3 = 2.35 \pm 0.05$, i.e. a power-law scaling of the iso-surfaces (Level 2 complexity). The results were reported to be Reynolds number independent, but the Reynolds number ranges of the particular flows were not stated explicitly. However, Sreenivasan (1991) reported a lack of a power-law range for thresholds near the mean concentration, indicating a fractal dimension that varies with scale.

Miller and Dimotakis (1991) conducted experiments near the centerline of round jets, at Reynolds numbers between 1,000 and 24,000. They performed fractal analysis on line transects from single-point concentration time series and plane transects from time series of concentration profiles (streak images). At least at the smaller Reynolds numbers, the measurements resolved the smallest scales of the concentration field. The concentration iso-surfaces did not exhibit scale similarity. In contrast, the fractal dimension was found to be a function of scale, between the topological and the embedding dimension. In addition, they reported a significant dependence on the threshold concentration level and the Reynolds number.

Frederiksen et al. (1996, 1997) obtained 4-D space-time concentration data for a turbulent round jet at Reynolds numbers between 2,900 and 5,000. At these relatively low Reynolds numbers, they were able to resolve the smallest concentration scales in the flow. The power-law behavior was investigated by comparing to a deterministic fractal set (Cantor dust) and a stochastic fractal set (fractal Brownian motion), both of known dimension. The 1-D concentration iso-surfaces adhered to the power law less closely than the Cantor dust, but approximately as closely as the fractal Brownian motion. It was concluded that line transects exhibited a power-law scaling in the viscous-convective range, with a constant fractal dimension of $D_1 = 0.48$. However, no power-law behavior was found at scales above the Kolmogorov scale. The discrepancy between the findings of Miller and Dimotakis (1991) and Frederiksen et al. (1996) was explained by the fact that Frederiksen et al. (1996) exactly determined the location and width of the threshold crossings from the surroundings of the line transects. For plane transects and the complete 3-D iso-surfaces, however, Frederiksen et al. (1997) did not find a constant fractal dimension. This was attributed to non-fractal inclusions within the concentration field, which increasingly mask power-law behavior for higher-dimensional transects. As a consequence, Frederiksen et al. (1997) found that the additive law did not hold.

A round jet was also considered by Catrakis and Dimotakis (1996) and Catrakis (2000), for Reynolds numbers between 4,500 and 18,000. They focused on concentration iso-surfaces in the outer region of the jet, for which they could resolve the complete range of scales from the diameter of the jet to the Batchelor scale. Plane transects as well as line transects were utilized. The fractal dimension was a smooth function of scale, from $D = d_t$ at the smallest scales, to $D = d$ at the largest scales. Besides, the fractal dimension depended on the concentration threshold level and Reynolds-number. Comparisons between the line and plane transects revealed deviations from the additive law. Another important aspect of this study was the connection of the fractal dimension to a scale distribution PDF. It was shown that the small-scale structure of the concentration iso-surfaces may be reasonably modeled by a Poisson or log-normal scale PDF.

Another examination of a turbulent round jet was performed by Villermaux and Innocenti (1999), for Reynolds numbers between 6,000 and 12,000. In these experiments, only scales larger than the Kolmogorov scale were resolved. The goal was to establish a general and comprehensive relation between the fractal dimension and various parameters such as length scale, Reynolds number, concentration threshold, and time. In that analytic relation, the fractal dimension was scale and concentration threshold level dependent, while being independent of the Reynolds number.

Most recently, Catrakis et al. (2002) raised new hope for finding physical-space scale similarity in turbulence. With their scale-local measures (cf. Sec. 2.2.7), as opposed to the scale-cumulative fractal dimension, a power-law scaling was detected for the 3-D concentration iso-surfaces in the outer region of a round jet at Re $=$ $20,000$. The corresponding fractal dimension was $D = 2.3$, which is close to the value originally reported by e.g. Sreenivasan and Meneveau (1986). They concluded that scale dependence in the cumulative iso-surface structure may be consistent with scale-local self-similarity and argued that the large-scale structure in turbulent flows may mask the self-similarity at smaller scales.

CHAPTER 3

Method

3.1 Experiment setup

The flow facility, experiments, and imaging technique are described in detail in Dasi and Webster (2003), and are summarized here for completeness. The flow facility consisted of a 1.07 m wide, 24.4 m long tilting flume. The fully developed, uniform depth (H=100mm) open channel flow (flow rate 0.0107 m^3/s) produced an equilibrium turbulent boundary layer on the flume bed. In Sec. 2.1.7, a coordinate system was defined by the longitudinal coordinate x, and the vertical coordinate z, with the origin at the plume source location. The flow Reynolds number is $\mathrm{Re} = (\langle U \rangle L)/\nu = 10,000$, i.e. within the range in which the mixing transition occurs (compare Sec. 2.1.5).

A fluctuating passive scalar field was generated by an iso-kinetic release of the laser fluorescent dye Rhodamine 6G ($\mathrm{Sc} = \nu/\kappa \approx 1000$, where $\nu = 1 \times 10^{-6}$ m^2/s and $\kappa = 1 \times 10^{-9}$ m^2/s) through a nozzle, with a source flow rate of $\dot{V}_{source} = 1.733 \times 10^{-6}$ m^3/s. The nozzle was located at the centerline of the flume, 50 mm above the flume bed, and had a nozzle diameter of 4.7 mm. A streamlined fairing on the downstream side of the nozzle minimized the wake perturbation introduced to the flow. The source concentration is adjusted to fit the dynamical range of the measurement system.

The length scales of the flow vary from the integral scale, which is approximately half of the water depth, i.e. $l = 50$ mm, to the Kolmogorov scale. The length scales of the passive scalar field vary from the plume width to the Batchelor scale. To estimate the scales, an order of magnitude estimate of the dissipation rate was made from Eq. 2.18, where the rms fluctuating velocity, u', was determined from Particle

Table 3.1: Important flow and plume parameters.

Re	-	10,000
$\langle U \rangle$	[mm/s]	100
u'	[mm/s]	10
ϵ	[mm^2/s^3]	20
l	[mm]	50
η	[μm]	700
η_B	[μm]	20

Tracking Velocimetry (PTV) measurements for the boundary layer. The flow and plume parameters are summarized in Tab. 3.1.

We employed the planar laser-induced fluorescence (PLIF) technique to measure a sequence of the passive scalar fields (images collected by L. P. Dasi). Measurements were performed in a vertical plane parallel to the flow direction (i.e. the $x-z$ plane) at the centerline of the flume. The laser sheet was created by sweeping an Argon-ion beam (514 nm, 5W, Coherent Innova 90) with a scanning mirror attached to a galvanometer (Cambridge Technology galvanometer controlled by LabView). One scan through the full image region occurs in 8 ms, thus the concentration field is nearly frozen by the measurement technique. The laser beam passed through a beam expander and a convex lens with a 2 m focal length, giving a $1/e^2$ diameter of 80 μm at the measurement location. The laser light caused the dye to fluoresce, and an 8-bit digital CCD camera (Kodak model Megaplus ES1.0 with a 200 mm Nikon MicroNikkor lens, Fstop = 4, Gain = 1, and UV and Hot Mirror, and Orange 21 filters) captured the emitted light over a 20×20 mm region that was located symmetrically about the nozzle centerline. The incident laser light was blocked by an optical filter and does not illuminate the camera sensor. The camera's CCD chip had 1008×1018 pixels, which gives an image resolution of approximately 20 μm per pixel. Thus, the measurements resolved the Batchelor length scale in both dimensions of the laser plane and were slightly under-resolved in the perpendicular direction. A total of 6000 consecutive images were captured at a rate of 10 Hz and stored on a hard drive array in real time (Video Savant software). The center 512×512 pixels of each image (i.e. corresponding to an effective image size of approx. 10×10 mm) were used to extract fractal measures based on a binary image size algorithm.

3.2 Numerical method

3.2.1 Image calibration

The light intensity level of the digitally acquired raw images is directly proportional to the concentration of the passive scalar dye. Therefore, a calibration can be performed to convert the raw intensity images into concentration fields. The calibration data was collected by imaging uniform concentration solutions of various levels. A Plexiglas box, temporarily placed in the measurement region, was consecutively filled with solutions of $C^1 = 19.51\ \mu$g/L, $C^2 = 38.83\ \mu$g/L, and $C^3 = 57.96\ \mu$g/L. A hundred images of each solution were taken to determine the corresponding light intensity levels. In addition, 100 images were taken of clean water in the measurement region without the Plexiglas box to yield the light intensity levels that corresponded to $C^0 = 0\ \mu$g/L. For each concentration level, the 100 images were ensemble-averaged to get the mean light intensities for each pixel, i.e. $\langle I^0 \rangle$, $\langle I^1 \rangle$, $\langle I^2 \rangle$, and $\langle I^3 \rangle$. Based on these data, a linear calibration equation was determined for each pixel by means of a least squares regression. To prevent negative concentration values, the zero-concentration data is not involved in the least squares regression but was considered as a fixed point of the equation. Calibrating each pixel separately eliminates errors due to non-uniformities in pixel sensitivity and laser sheet illumination.

Since the nozzle concentration varied for measurements at different downstream distances it was convenient to normalize the pixel concentrations, C, by the particular source concentration, C_{source}, to get normalized pixel concentrations, C^*, between zero and unity. The linear calibration equation for a pixel at the image location (i, j) is given by

$$C^*_{i,j}(I_{i,j}) = \frac{A_{i,j} I_{i,j} + B_{i,j}}{C_{source}}. \tag{3.1}$$

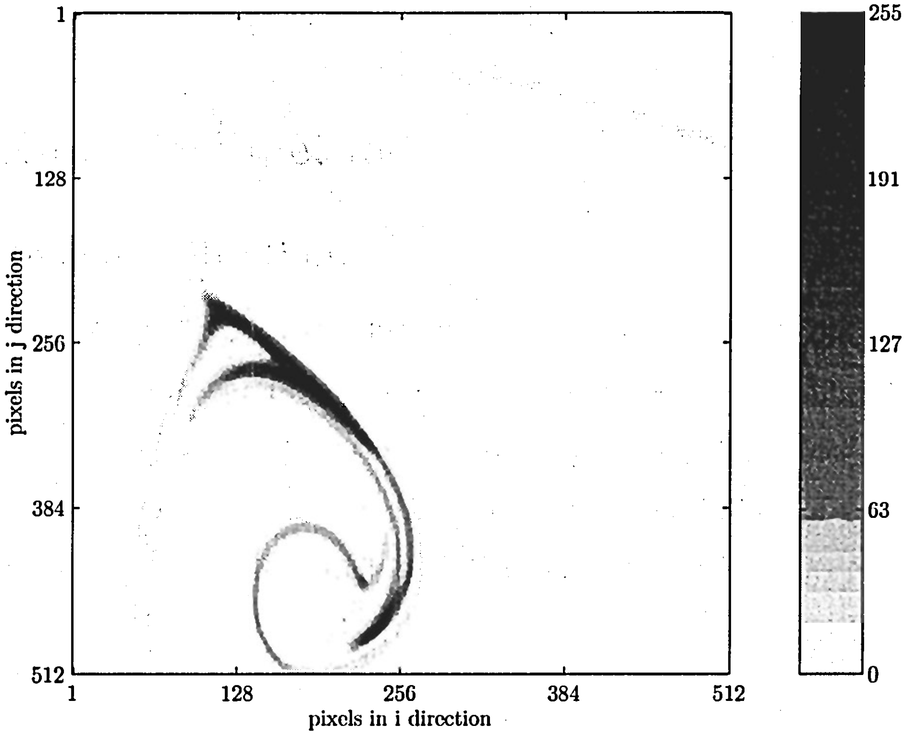

Figure 3.1: Raw intensity image. Contour level corresponds to pixel intensity I.

The two parameters in this equation are

$$A_{i,j} = \frac{\sum_{cal=1}^{cal_{max}} C^{cal}(\langle I_{i,j}^{cal}\rangle - \langle I_{i,j}^{0}\rangle)}{\sum_{cal=1}^{cal_{max}} (\langle I_{i,j}^{cal}\rangle - \langle I_{i,j}^{0}\rangle)^2}, \tag{3.2}$$

$$B_{i,j} = -A_{i,j}\langle I_{i,j}^{0}\rangle. \tag{3.3}$$

Fig. 3.1 shows a typical raw light intensity image and Fig. 3.2 represents the corresponding calibrated concentration image.

3.2.2 Choice of concentration threshold

To extract iso-surfaces from the calibrated concentration images, one has to set a proper threshold for the passive-scalar concentration. The choice of a particular threshold level seems somewhat arbitrary. The essential question, of course, is whether the calculated fractal measures depend on the threshold choice. The literature contains several approaches to justify the choice of a particular threshold value, with contradictory findings concerning threshold-dependence. Sreenivasan (1991) compared fractal dimensions for a range of concentration thresholds and found them

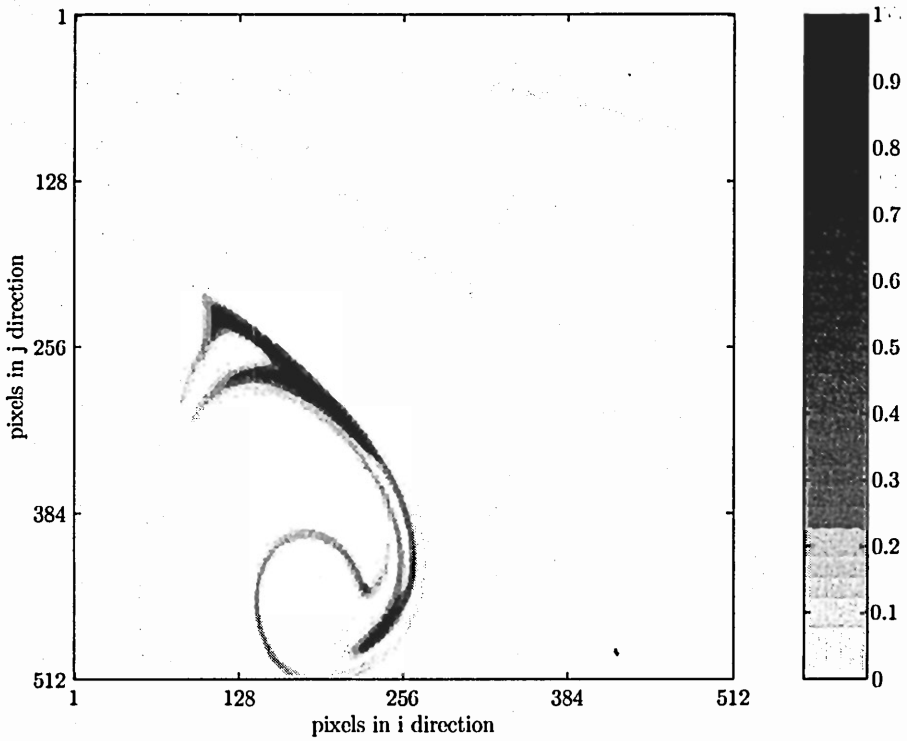

Figure 3.2: Concentration image. Contour level corresponds to C^*.

to be threshold-independent within approximately $0.25 < C_{th}/\langle C\rangle < 2$. However, the size of the range of geometric scales that exhibited a constant fractal dimension was found to depend on the threshold. As already mentioned in Sec. 2.2.8, the self-similar scaling range (Level 2 complexity) almost vanished for thresholds near the mean concentration. Frederiksen et al. (1996) also reported power-law behavior with a fractal dimension independent of the concentration threshold for $0.2 < C_{th}/\langle C\rangle < 4.0$. They eventually used the mean concentration as the threshold because it produced the largest number of threshold crossings. Catrakis and Dimotakis (1996) used characteristic points in the concentration PDF, such as local peaks and minima, for their concentration thresholds. As their images corresponded to cross-sections of a jet flow, they argued that higher concentration thresholds extract iso-surfaces near the centerline of the jet, whereas lower thresholds correspond to iso-surfaces in the outer regions of the jet. For their data, the scale-dependent fractal dimension changed with concentration threshold, being largest at intermediate concentrations. Catrakis et al. (2002) followed this work, and considered only very low concentration thresholds to extract the boundary between mixed fluid and pure ambient fluid. A much more detailed discussion on the influence of the concentration threshold was given by Miller and Dimotakis (1991). They investigated the behavior of the scale-dependent fractal dimension in the range $0.2 < C_{th}/\langle C \rangle < 1.7$. By means of 3-D plots of dimension versus geometric scale and threshold, they showed significant changes in the shape of the dimension plots across the threshold range. Finally, Villermaux and Innocenti (1999) established an analytic relation for the fractal dimension, which exhibits an exponential dependency on the concentration threshold.

All of the results discussed above correspond to a turbulent jet. For our turbulent boundary layer data, there is no distinct concentration gradient within the small images, and we expect the concentration distribution to be statistically homogenous. Therefore, it seems reasonable and necessary to consider a wide range of possible thresholds. The range is bounded on the low end by the fluctuating light intensity noise and the light intensity resolution of the digital camera. Towards higher thresholds, the iso-surface structure becomes increasingly sparse. As fewer images contain iso-surfaces, more and more images are required to get statistically trustworthy results. Thus, the maximum number of images puts an upper limit on the concentration threshold. Fig. 3.3 shows concentration iso-surfaces (more precisely: boundary-outline pixels, which will be introduced in the next section) extracted from the same concentration field (Fig. 3.2), for different concentration thresholds. The thresholds approximately range from the lower (noise) limit to the higher (sparseness) limit for that particular concentration image.

However, there may be applications in which one distinct concentration threshold is of interest. In the field of combustion, for example, we might focus on the stoichiometric concentration of fuel in air.

3.2.3 Extraction of concentration iso-surfaces

There are several approaches to determine the concentration iso-surfaces and to represent them numerically. If the images are relatively noise-free, the simple procedure of setting a proper threshold on the pixel concentration field marks the boundary

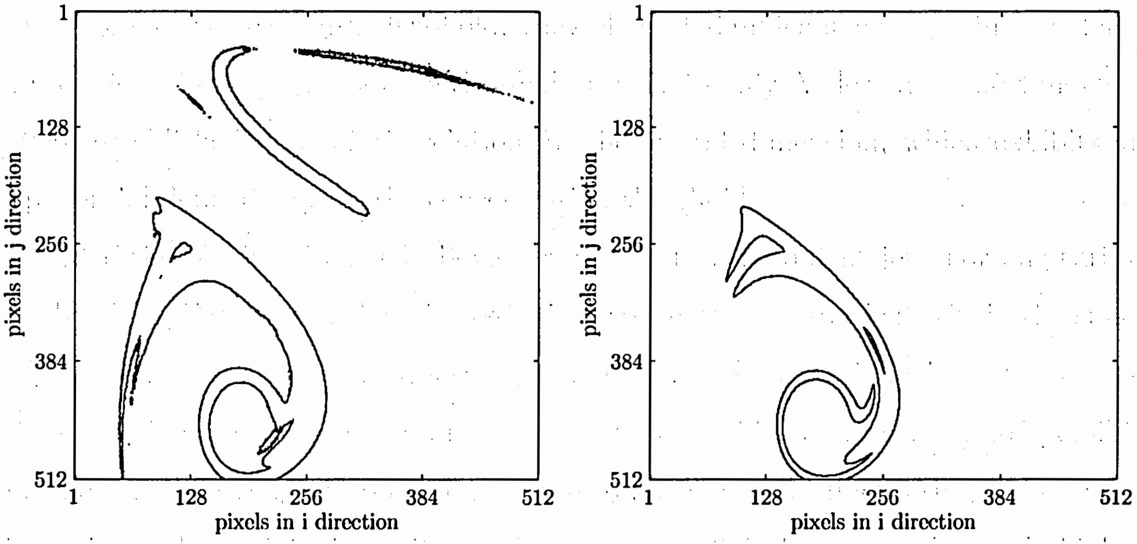

(a) $C_{th}^{*} = \langle C^{*} \rangle + 0 \cdot \mathrm{sdev}(C^{*})$ (b) $C_{th}^{*} = \langle C^{*} \rangle + 1 \cdot \mathrm{sdev}(C^{*})$

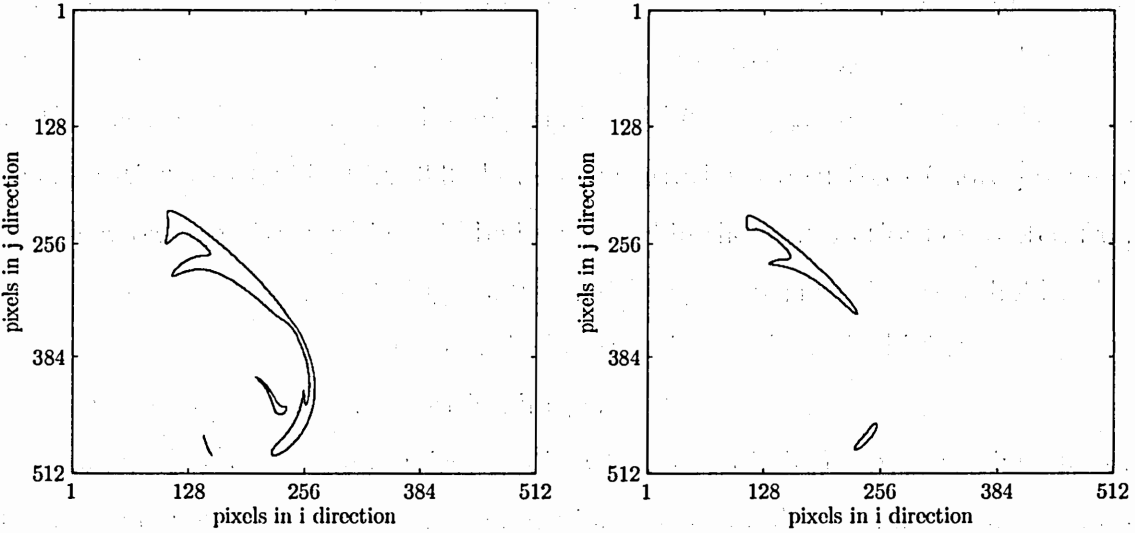

(c) $C_{th}^{*} = \langle C^{*} \rangle + 3 \cdot \mathrm{sdev}(C^{*})$ (d) $C_{th}^{*} = \langle C^{*} \rangle + 7 \cdot \mathrm{sdev}(C^{*})$

Figure 3.3: Concentration iso-surfaces extracted from the same concentration image, for different concentration thresholds C_{th}^{*}.

well. More sophisticated approaches involve edge enhancement techniques from the field of pattern recognition (Sreenivasan, 1991). For matrix-based data such as our digital images, the easiest and most commonly applied method is an iso-surface representation by boundary pixels. In general terms, boundary pixels are defined as those pixels within an image across which a specified concentration threshold is crossed. Catrakis and Dimotakis (1996) provided an extensive discussion about problems and possible improvements of the boundary pixel approach. First, conventional boundary pixels exhibit an inherent asymmetry in their representation of small islands and lakes. As suggested in Sec. 2.2.4, the terms "island" and "lake" here refer to isolated regions that are above and below the concentration threshold, respectively. At small scales, the asymmetry can produce fractal dimension estimates below the topological dimension of the iso-surface. The problem can be overcome by using the boundary-outline pixels approach instead of the conventional boundary pixels approach. Conventional boundary pixels are only located on the island side of the coastline, while boundary-outline pixels cover the complete coastline on both the island and the lake side.

A closer look at each algorithm indicates the differences. For the conventional boundary pixels, each pixel is successively examined as a "center pixel". If the center pixel has a concentration equal to or above the threshold, its surroundings are examined. Each center pixel shares its edges with up to four neighboring pixels. If one of those four neighboring pixels has a concentration below the threshold, the center pixel is identified as a conventional boundary pixel. For the boundary-outline pixels approach, each pixel is again considered as the center pixel. The eight neighboring pixels of the center pixel (including the neighbors at the corners of the center pixel) are examined for a threshold-crossing between the center pixel and the neighbor pixel. If a crossing is present, a linear interpolation is applied between the two pixel concentrations to estimate the location of the level-crossing on the line connecting the center pixel and the neighbor pixel. The pixel that is closer to the interpolated level-crossing location is identified as a boundary-outline pixel. If the level-crossing is located directly in the middle between the two pixels, both pixels are boundary-outline pixels.

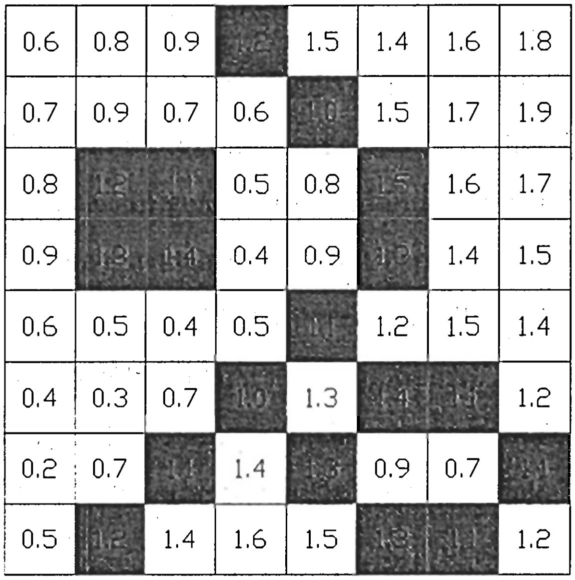

0.6	0.8	0.9	▨ 1.2	1.5	1.4	1.6	1.8
0.7	0.9	0.7	0.6	▨ 1.0	1.5	1.7	1.9
0.8	▨ 1.2	▨ 1.1	0.5	0.8	▨ 1.5	1.6	1.7
0.9	▨ 1.3	▨ 1.4	0.4	0.9	▨ 1.0	1.4	1.5
0.6	0.5	0.4	0.5	▨ 1.1	1.2	1.5	1.4
0.4	0.3	0.7	▨ 1.0	1.3	▨ 1.4	▨ 1.6	1.2
0.2	0.7	▨ 1.1	1.4	▨ 1.3	0.9	0.7	▨ 1.1
0.5	▨ 1.2	1.4	1.6	1.5	▨ 1.3	▨ 1.1	1.2

Figure 3.4: Exemplary 8×8 conventional boundary pixels.

To demonstrate the different results produced by these methods, we created a 8×8 pixels sample concentration field with concentration levels between zero and two. For a concentration threshold of unity, Fig. 3.4 shows the conventional boundary pixels, while Fig. 3.5 shows the boundary-outline pixels. The asymmetry between the small island in the upper-left corner and the small lake in the lower-right corner is evident in Fig. 3.4. Alternatively, the boundary-outline pixel method removes this asymmetry (Fig. 3.5).

Catrakis and Dimotakis (1996) additionally used splines instead of pixels to numerically represent the iso-surfaces. The spline-representation was necessary because they adapted the bounding box of the box-counting algorithm to the actual extent of the iso-surface structure. Therefore, the bounding box varies in size between different images, and in general does not have a binary size. In this case, non-integer box sizes are encountered during the subdivision of the box-counting algorithm, and an iso-surface representation consisting of pixels would require a splitting of the pixels. For our boundary layer data, however, there is no characteristic extent of the iso-surfaces within the images, so it does not make sense to adapt the bounding box to particular images. The splines also allow for an iso-surface resolution below the physical pixel size. The benefit of this sub-pixel resolution is questionable, because the iso-surfaces

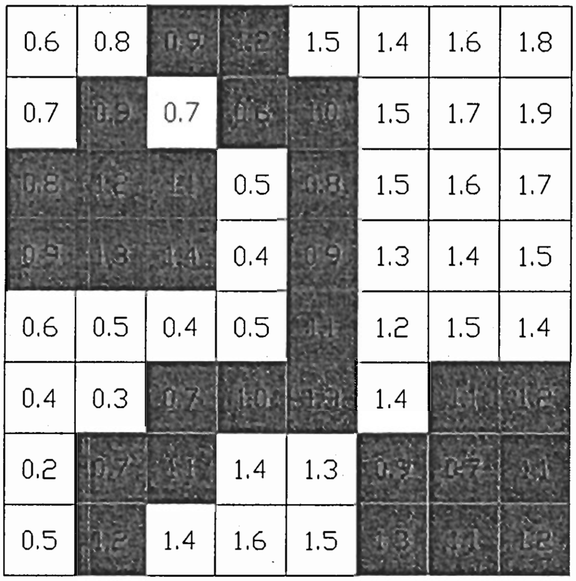

0.6	0.8	**0.9**	**1.2**	1.5	1.4	1.6	1.8
0.7	**0.9**	0.7	**0.6**	**1.0**	1.5	1.7	1.9
0.8	**1.2**	**1.1**	0.5	**0.8**	1.5	1.6	1.7
0.9	**1.3**	**1.4**	0.4	**0.9**	1.3	1.4	1.5
0.6	0.5	0.4	0.5	**1.1**	1.2	1.5	1.4
0.4	0.3	**0.7**	**1.0**	**1.3**	1.4	**1.1**	**1.2**
0.2	**0.7**	**1.1**	1.4	1.3	**0.9**	**0.7**	**1.1**
0.5	**1.2**	1.4	1.6	1.5	**1.3**	**1.1**	**1.2**

Figure 3.5: Exemplary 8×8 boundary-outline pixels.

cannot be convoluted at scales that are not resolved by the physical pixels of the camera. Thus, as expected, Catrakis and Dimotakis (1996) found the fractal dimension to approach the topological dimension for their sub-pixel scales. For our data, a sub-pixel resolution does not make sense because the laser sheet thickness is also of the order of the pixel size. From the discussion above, it is most reasonable for us to use boundary-outline pixels at the pixel resolution to represent the iso-surfaces.

3.2.4 Noise considerations

In the course of the present study, we encountered various sorts of noise in the data sets. For example, one preliminary data set exhibited air bubbles and dirt particles in the images that artificially increased the fractal dimension over the whole range of scales. A sophisticated filter algorithm was developed to remove the noise spots without affecting the surrounding real data (for the effect of the filter, compare Figs. 3.6(a) and (b)). The filter was based on the characteristic shape of the noise spots, and on the fact that the spots could appear independent of the presence of surrounding lower-concentration dye. Essentially, a filter square, slightly larger than the largest noise spots, moved through the concentration images and removed all high-concentration areas that were smaller than the filter square and were completely surrounded by pure ambient water. But finally, we found that carefully cleaning the flume sump and operating the flume for long time periods removed the dirt particles and the dissolved air, respectively.

Another data set was biased by a memory effect of the camera (Dalsa model 01M28, 10 bit), such that pixels in image regions of high light intensity did not perform a complete reset between consecutive images and therefore overestimated the light intensity of the following image (see two consecutive images in Fig. 3.6(c) and (d)). In the affected image regions, this effect corresponded to an artificial downward shift of the concentration threshold for the iso-surface extraction. The problem was overcome by using another camera (Kodak model Megaplus ES1.0, 8 bit) that did not have the pixel reset problem.

Other problems arose from the need to match the dynamical range of the camera. In one data set, the calibration point for zero concentration was slightly below the dynamical range of the camera, which biased the pixel calibration equations. As a result, the iso-surfaces were artificially wrinkled and the fractal dimension was overestimated at small scales. This effect could be reduced for example by neglecting the erroneous calibration point in the least squares regression.

In the final data set, all noise problems mentioned above were overcome through experimental procedures instead of through image processing. For all of the previous noisy data sets, the resulting fractal measures were similar when performing the indicated numerical improvements. Therefore, the results reported in this thesis can be considered as rather robust.

One kind of noise was present in the final data set that merits discussion. For raw light intensity levels close to the lower end of camera's dynamical range (which corresponds to zero due to an offset), the pixel intensities show random fluctuations around the real value. When using normalized concentration thresholds as indicated in Fig. 3.3 (see also Sec. 4.2.1 for a detailed discussion of the normalized concentration threshold), the lowest raw intensities are encountered for low concentration thresholds far away from source, and the corresponding iso-surfaces are most affected by noise. As can be observed for the iso-surface in the upper part of Fig. 3.3(a), the noise

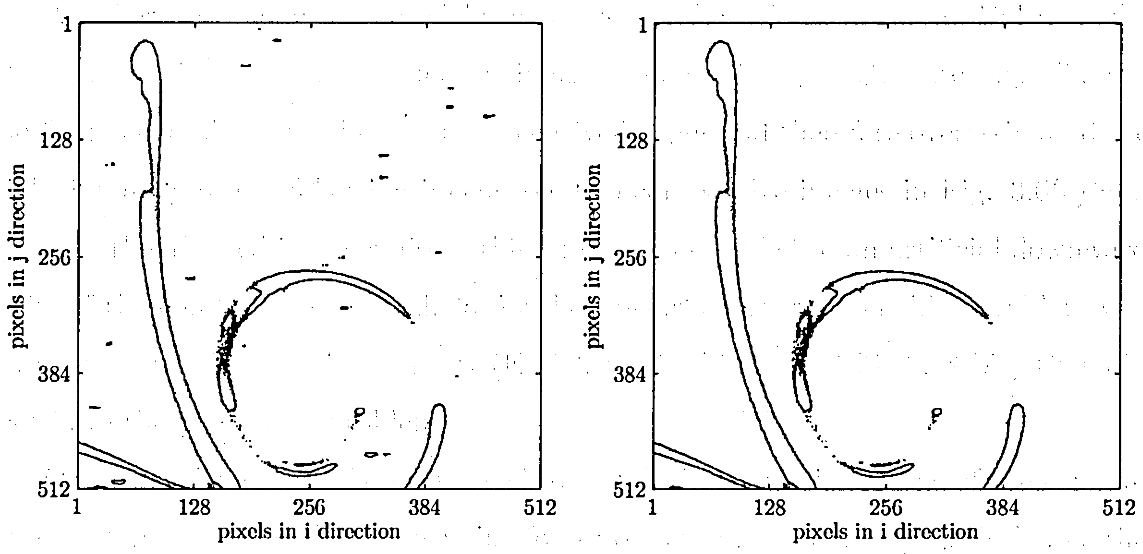

(a) Air bubbles and dirt particles

(b) Bubbles and particles filtered out

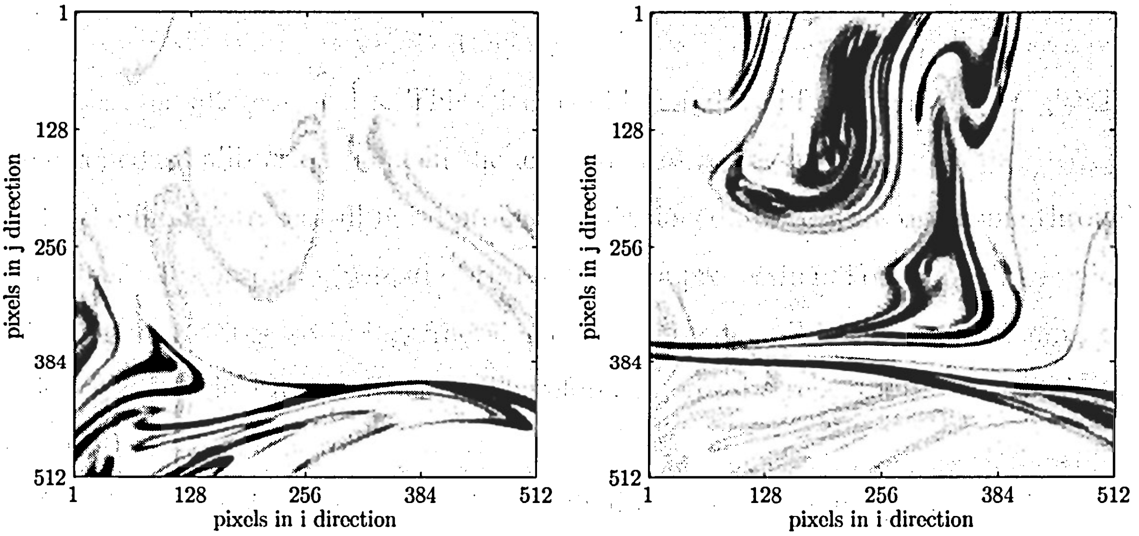

(c) Memory effect in image n

(d) Memory effect in image $n+1$

Figure 3.6: Examples of noise. (a) Iso-surface image with noise spots from air bubbles and dirt particles. (b) Same iso-surface image after filtration. (c), (d) Two consecutive concentration images exhibiting the memory effect. The dim remaining structure from image n can be observed in image $n+1$.

creates significant small-scale roughness of the iso-surfaces, which artificially raises the coverage dimension at small scales. Therefore, it is sensible to only consider concentration thresholds that correspond to a high signal to noise ratio, which we have done in Chapter 4.

3.2.5 Box-counting algorithm

The box-counting algorithm is the most commonly applied method to determine the coverage count, N, of a fractal object. As we have seen in Sec. 2.2.7, the coverage count is the basis for all other fractal measures. The box-counting algorithm is applied to a boundary pixel image and extracts values of the coverage count as a function of subsequently decreasing length scale, λ. The resulting set of discrete coverage count values, $N(\lambda)$, is stored for each image. Statistics of the related fractal measures, such as the coverage dimension, are calculated from the ensemble of images.

The algorithm starts with a bounding box with a characteristic side length, δ_b, defining the largest considered length scale. For the data of Catrakis and Dimotakis (1996), the 2-D images of the jet's cross-section contained the complete radial extent of the jet and therefore the bounding box could be adapted to the largest characteristic scale of the flow by using a rectangle that bounded the iso-surface structure. In our case, the image size is significantly smaller than the characteristic large scales of the plume and therefore it is sufficient to use the square image boundary as the bounding box.

The bounding box is then successively subdivided into an increasing number of boxes of smaller size, until the boxes reach pixel size. Obviously, it is necessary to use a binary bounding-box size, as well as binary subdivisions, because otherwise one would encounter boxes of non-integer pixel size. In our case, the consecutive box sizes are $\lambda = 512$, 256, 128, 64, 32, 16, 8, 4, 2, and 1 pixels. For the sample boundary-outline pixel image shown in Fig. 3.3(b), Fig. 3.7 demonstrates the subdividing grid for box sizes of $\lambda = 256$, 128, 64, 32, respectively.

At each subdivision step, we count the number of boxes that contain part of the iso-surface, which yields the coverage count, $N(\lambda)$, at the particular length scale,

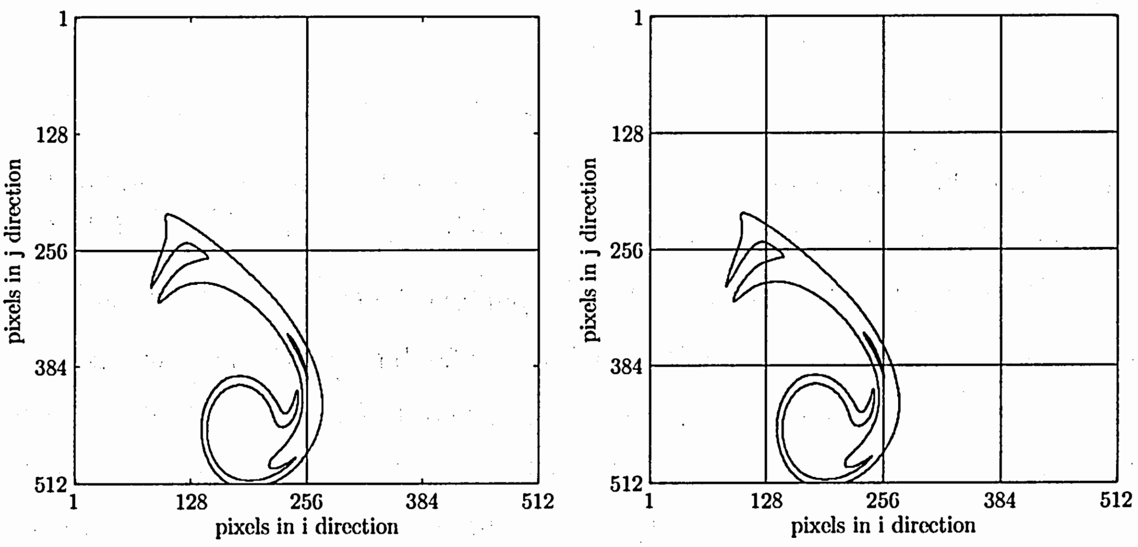
1
128
256
384
512
pixels in j direction
1
128
256
384
512
pixels in i direction

(a) 1st subdivision step: $N(\lambda = 256) = 3$.

(b) 2nd subdivision step: $N(\lambda = 128) = 7$.

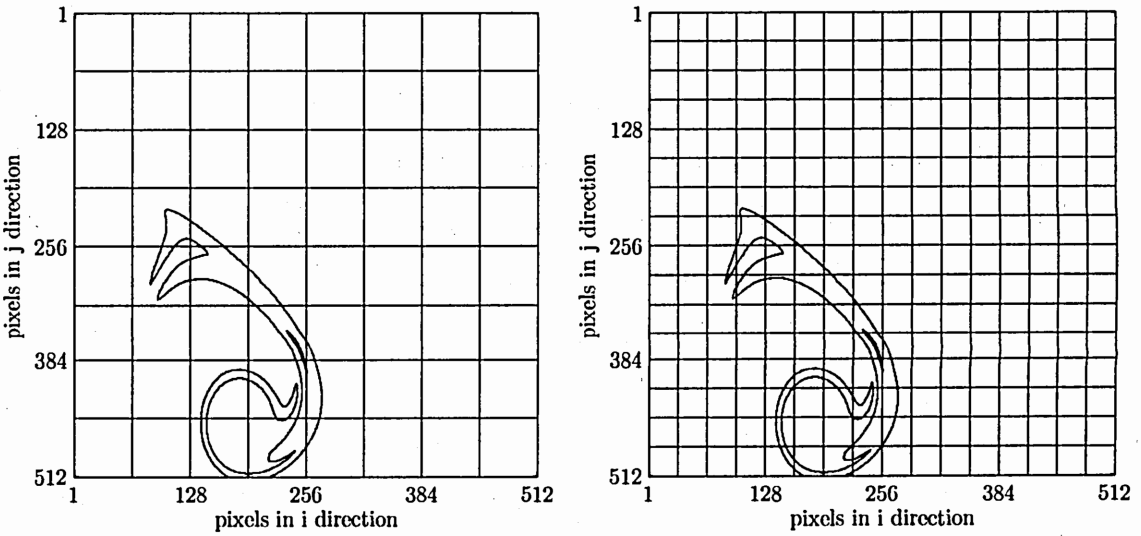
1
128
256
384
512
pixels in j direction
1
128
256
384
512
pixels in i direction

(c) 3rd subdivision step: $N(\lambda = 64) = 13$.

(d) 4th subdivision step: $N(\lambda = 32) = 37$.

Figure 3.7: Consecutive box-counting subdivision of the bounding box. Exemplary coverage counts are indicated for each step of the given sample image and subdivision arrangement.

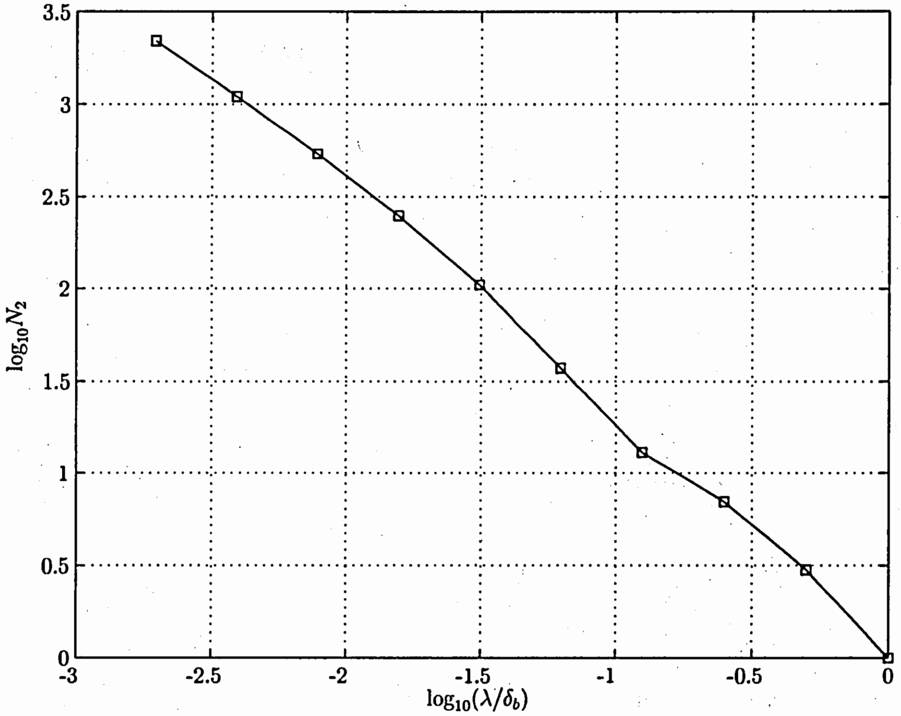

Figure 3.8: Coverage count for the boundary-outline pixel image from Fig. 3.3, and the subdividing arrangement depicted in Fig. 3.7.

λ, that corresponds to the current box size. For the boundary-outline pixel image from Fig. 3.3(d), and for the particular subdivision arrangement depicted in Fig. 3.7, the resulting coverage count is plotted in Fig. 3.8. As can be seen, the length scale, λ, is normalized by the size of the bounding box, δ_b, and logarithmic axes are used to visualize the characteristic slope that corresponds to the negative coverage dimension. For their 1-D data set and box-counting algorithm, Miller and Dimotakis (1991) argued that the choice of the starting location for the subdivision is arbitrary. A single starting location therefore fails to extract all of the information contained in a record, and could bias the box-counting results. They recommend shifting the starting location up to eight times within the possible range and ensemble-averaging the resulting coverage counts. This approach easily generalizes to our 2-D images. The shifting of the starting location is realized by calculating a step size, which is, in general, an eighth of the current subdividing box size. The step size defines a shifting grid, on which the subdividing grid is consecutively shifted by all possible multiples of the step size, in both the horizontal and vertical directions. Thus, for each box

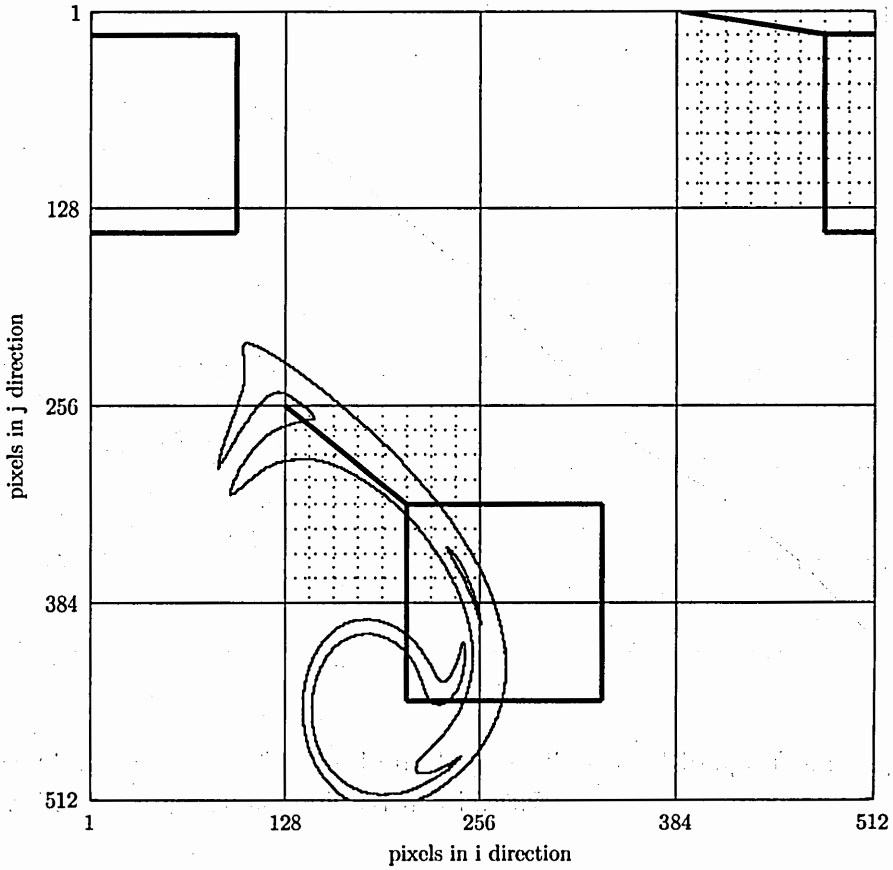

Figure 3.9: Shifting of the starting location for the box-counting subdivision at $\lambda = 128$. The two thick squares show exemplary shifts on the dotted shifting grid. The upper-right shifted box demonstrates the artificial connection between the right and the left image boundary.

size, λ, we shift the grid to up to $8 \times 8 = 64$ different locations. Figure 3.9 shows the shifting of a subdividing box at two exemplary locations. Of course, it does not make sense to shift the grid for the largest length scale, as the coverage count does not change during a shift. Also, at the small scales, the size of the subdivision boxes limits the number of possible shifts. For the smallest scale of one pixel, only one position within the shifting grid is possible. For the second-smallest subdividing box, which extends 2×2 pixels, there are $2 \times 2 = 4$ possible shifting grid locations, and so on.

As in the 1-D case, some boxes shift past the boundaries of the image. A weighting scheme may suggest itself for such boxes. Weighting the coverage count of the box by the fraction of the box that lies within the image did not yield reasonable results, when applied to the deterministic self-similar fractals described in Sec. 3.3.2. In addition, Miller and Dimotakis (1991) reported that various weighting schemes do not correct the difficulty associated with tiles extending past the end of a record. Alternatively, we artificially connected the left image boundary to the right one, and the upper image boundary to the lower one. For example, when a box extends beyond the right boundary of the image, the fraction outside the image is filled with an equivalently sized image fraction at the corresponding location of the left boundary (see the example in Fig. 3.9).

When we applied this algorithm to the deterministic fractal sets described in Sec. 3.3.2, the minimum coverage count from the shift options yielded significantly better results than the ensemble average. This is explained by the fact that the theoretical fractal dimension (i.e. the Hausdorff-Besicovitch dimension, see Sec. 2.2.5) is defined by the minimum number of boxes of arbitrary size that cover a set. In our case, we use equally-sized boxes, but we extract the minimum number of boxes necessary.

Finally, there is an issue associated with images that contain very little or no iso-surface structure. When ensemble-averaging over a number of images, completely empty images decrease the coverage count but do not contribute any information for the coverage dimension. One option is to exclude such images from the ensemble calculations. As the image size is an arbitrary length scale within the flow, one could argue that smaller empty regions within the images should also be left unconsidered. One way to do this is to neglect the coverage count of images down to length scales where the iso-surface structure occupies more than one of the subdividing boxes. This corresponds to an adaptation of the bounding box to the largest iso-surface structure present within a particular image. We have investigated the impact of rejecting empty regions on the different fractal measures. On the one hand, this approach seems to improve the performance of the algorithm in reproducing the exact fractal dimension of deterministic fractals. On the other hand, it neglects an essential characteristic of the flow field, which is the sparseness of the iso-surface structure, i.e. the space between filaments of dye. We believe that the real physics of the flow, expressed by fractal measures like the coverage fraction and the coverage length, are represented most accurately when the empty regions are included. For example, the total coverage length at the smallest scales of the concentration field, $L_2(\lambda \to \eta_B)$, corresponds to the surface area of the dye filaments within the 3-D flow and is therefore directly related to the molecular mixing flux according to Fick's law. Neglecting empty regions within the flow artificially increases the total coverage length (i.e. the total surface area in the flow field) and therefore leads to an overestimation of the global flux of molecular mixing. Thus, we will consistently use the full size of our images as the initial bounding box of the algorithm.

3.2.6 Calculation of fractal measures

From the analytical relations presented in Sec. 2.2.7, we know that the coverage count provides the basis for all other fractal measures of interest. The box-counting algorithm, described in the previous section, determines the coverage count of each image separately. We are ultimately interested in the fractal measures that are ensemble-averaged over all images. It is important to realize that the logarithmic derivatives in the definition of the coverage dimension, for example, do not commute with the procedure of ensemble-averaging. In other words, one has two options to calculate an ensemble-averaged coverage dimension, that yield different results. First, we can first ensemble-average the coverage count and then calculate an average coverage dimension as the logarithmic derivative of the ensemble-averaged coverage count. Second, it is possible to calculate the coverage dimension of each image separately, by means of the logarithmic derivative, and then ensemble-average the single-image values to yield a mean coverage dimension.

Let us define the ensemble-averaged coverage count,

$$\langle N_2(\lambda) \rangle = \frac{1}{n_{max}} \sum_{n=1}^{n_{max}} N_2^n(\lambda), \tag{3.4}$$

where n_{max} is the total number of images in the record, and the superscript indicates the number of the image to which the single coverage count corresponds. With this definition, the non-linearity between the ensemble average and logarithmic derivative, for the example of the coverage dimension, can be expressed by

$$-\frac{d\log_{10}\langle N_2(\lambda)\rangle}{d\log_{10}\lambda} \neq -\frac{1}{n_{max}}\sum_{n=1}^{n_{max}}\frac{d\log_{10}N_2^n(\lambda)}{d\log_{10}\lambda}. \qquad (3.5)$$

The same ambiguity arises for the calculation of the length-area ratio exponent and the length-area density exponent. In the literature of fractal analysis, this issue has only been addressed by Villermaux and Innocenti (1999). They found both approaches to yield numerically similar results. Without explanation, Catrakis and Dimotakis (1996) performed an ensemble-averaging of the coverage count over a number of realizations of their 2-D boundary pixel images, and based the other measures, such as the coverage dimension, on that result. Shepherd et al. (1992) also ensemble-averaged the coverage count over 200 flame images to get an averaged coverage dimension. On the other hand, Frederiksen et al. (1996) calculated the coverage dimension from many single image coverage counts and plotted all of them in one figure to illustrate the variation of the dimension. They extracted a mean dimension out of the set of single image dimensions. A mixture of both approaches can be found in Miller and Dimotakis (1991), where the coverage counts were ensemble-averaged, but single-image coverage dimensions were also shown.

One could argue that the better approach should reproduce the known dimension of deterministic self-similar fractals (cf. Sec. 2.2.4) with a higher precision. We tested both approaches on the evaluation image sets that were created from deterministic self-similar fractals, as described in the following section. Despite the natural oscillations around the theoretical value of the fractal dimension, we could identify the first approach, i.e. the averaging of the coverage count, to be more accurate. Another disadvantage of the second approach, i.e. the averaging of the single-image fractal measures, is that the coverage dimension, for example, is not defined for a completely empty image. Therefore, one has to reject such empty images during the process of ensemble-averaging. For other measures like the coverage length, we have argued in the previous section that empty images should be retained as an essential feature of the overall concentration field. Thus, there is an inconsistency associated with the second approach. In addition, it is more convenient to perform the ensemble-averaging over a large number of images only once (i.e. for the coverage count), and to base the calculations of the fractal measures on a significantly reduced amount of data. We favor the first approach and therefore ensemble-average the coverage count over all images and base all mean fractal measures on that data.

The analytical relations between the coverage count and the other fractal measures (cf. Sec. 2.2.7) have to be discretized to be applicable to our discrete coverage count data. The box-counting algorithm produces 10 discrete values of the coverage count, each corresponding to a particular subdivision step. We label the subdivision steps by the variable s, with $0 \leq s \leq s_{max}$, and $s_{max} = 9$. The initial bounding box corresponds to $s = 0$, and the final subdividing grid of unity pixel size corresponds to $s = s_{max}$. Thus, the subdivision box sizes, normalized by the size of the bounding box, take the values $\lambda_s/\delta_b = 1/2^s = 1/1, 1/2, ..., 1/512$. The ensemble average of the single-image coverage count, N_2, for $0 \leq s \leq s_{max}$, is therefore given by

$$\langle N_2(\lambda_s/\delta_b)\rangle = \frac{1}{n_{max}} \sum_{n=1}^{n_{max}} N_2^n(\lambda_s/\delta_b). \tag{3.6}$$

Based on the ensemble-averaged coverage count, the ensemble average of the coverage fraction, F_2, coverage length, L_2, and length-area ratio, Ω_2, for $0 \leq s \leq s_{max}$, can be calculated from

$$\langle F_2(\lambda_s/\delta_b)\rangle = \left(\frac{\lambda_s}{\delta_b}\right)^2 \langle N_2(\lambda_s/\delta_b)\rangle, \tag{3.7}$$

$$\langle L_2(\lambda_s/\delta_b)\rangle = \lambda_s \langle N_2(\lambda_s/\delta_b)\rangle, \tag{3.8}$$

$$\langle \Omega_2(\lambda_s/\delta_b)\rangle = \frac{\lambda_s}{\delta_b} \langle N_2(\lambda_s/\delta_b)\rangle, \tag{3.9}$$

respectively.

To discretize the derivatives, we employ second-order accurate central differences centered at the half-points between the consecutive subdivision steps (i.e. at $\lambda_{s+1/2}/\delta_b$) and based on the data at the two neighboring subdivision steps, λ_{s+1}/δ_b, and λ_s/δ_b. This means that we get one data point less than the total number of subdivisions. The ensemble averaged of the coverage dimension, D_2, LEB-scale PDF, f_2, length-area ratio exponent, α_Ω, and length-area density, g_2, for $0 \leq s \leq s_{max} - 1$, are calculated from

$$\langle D_2(\lambda_{s+1/2}/\delta_b)\rangle = -\frac{\log_{10}\langle N_2(\lambda_{s+1}/\delta_b)\rangle - \log_{10}\langle N_2(\lambda_s/\delta_b)\rangle}{\log_{10}(\lambda_{s+1}/\delta_b) - \log_{10}(\lambda_s/\delta_b)}, \tag{3.10}$$

$$\langle f_2(\lambda_{s+1/2}/\delta_b)\rangle = \frac{\langle F_2(\lambda_{s+1}/\delta_b)\rangle - \langle F_2(\lambda_s/\delta_b)\rangle}{(\lambda_{s+1}/\delta_b) - (\lambda_s/\delta_b)}, \tag{3.11}$$

$$\langle \alpha_\Omega(\lambda_{s+1/2}/\delta_b)\rangle = -\frac{\log_{10}\langle \Omega_2(\lambda_{s+1}/\delta_b)\rangle - \log_{10}\langle \Omega_2(\lambda_s/\delta_b)\rangle}{\log_{10}(\lambda_{s+1}/\delta_b) - \log_{10}(\lambda_s/\delta_b)}, \tag{3.12}$$

$$\langle g_2(\lambda_{s+1/2}/\delta_b)\rangle = -\frac{\langle \Omega_2(\lambda_{s+1}/\delta_b)\rangle - \langle \Omega_2(\lambda_s/\delta_b)\rangle}{(\lambda_{s+1}/\delta_b) - (\lambda_s/\delta_b)}, \tag{3.13}$$

respectively.

Finally, the length-area density exponent, α_g, involves the logarithmic derivative of the length-area density, which itself is a derivative. Thus, the central differences of the length-area density exponent are centered at the subdivision steps, λ_s/δ_b, and calculated from values of the length-area density, located at the half points, $\lambda_{s+1/2}/\delta_b$. For $1 \leq s \leq s_{max} - 1$, we get

$$\langle \alpha_g(\lambda_s/\delta_b)\rangle = -\frac{\log_{10}\langle g_2(\lambda_{s+1/2}/\delta_b)\rangle - \log_{10}\langle g_2(\lambda_{s-1/2}/\delta_b)\rangle}{\log_{10}(\lambda_{s+1/2}/\delta_b) - \log_{10}(\lambda_{s-1/2}/\delta_b)}. \tag{3.14}$$

3.3 Testing of algorithm

3.3.1 Approach

Before calculating the fractal measures of the passive scalar iso-surfaces in our turbulent boundary layer, it is necessary to validate the numerical method. A common way to test algorithms for fractal analysis is to evaluate the performance when applied to deterministic self-similar fractal objects of known theoretical dimension (cf. Sec. 2.2.4). For our concentration field, we expect a range of scales from the integral scale, l, to the Batchelor scale, η_B. As explained in Sec. 3.1, the largest scales in the flow are of the order of 3400 pixels, i.e. much bigger than our images, and the smallest scales have a size of the order of one pixel. We created fractal objects with the same range of scales, and extracted a large number of 512×512-pixel-sized images from these objects. With these images, it is possible to test three different parts of the numerical method: the box-counting algorithm, the ensemble-averaging over the set of images, and the discretization of the logarithmic derivative to calculate the coverage dimension.

The concentration iso-surfaces in our study can be expected to exhibit a range of fractal dimensions. For a trustworthy evaluation, it is therefore necessary to test the performance for several fractal objects with different dimensions. Koch curves, as introduced in Sec. 2.2.4, are quite simple to create with particular dimensions. A certain degree of dispersion was introduced because then the created image sets closely resemble our real data compared to contiguous Koch curves.

Besides the general validation of the numerical method, the evaluation image sets allow us to investigate the influence of several parameters on the algorithm accuracy, such as the dimension, the number of shifts of the starting location, the adaptation of the bounding box, and the issue of ensemble-averaging the coverage count versus the coverage dimension.

3.3.2 Creation of evaluation image sets

Based on the examples of classical and detached Koch curves with different fractal dimensions given by Mandelbrot (1982), we developed five different deterministic fractals with the dimensions $D = 1.1046$, 1.2553, 1.4466, 1.6131, and 1.7604. In analogy to the results of Catrakis and Dimotakis (1996) for a jet, for example, we initially expected the concentration iso-surfaces in our flow to exhibit fractal dimensions between unity and two, because they are more complex than a straight line, but do not fill the entire image plane. As discussed theoretically in Sec. 2.2.6, and confirmed by our results in Chapter 4, this range turned out to hold only for scales that are smaller than the largest iso-surfaces. Nevertheless, we only examined deterministic self-similar fractals with dimensions above unity. Higher dimensions were not examined because for the $D = 1.7604$ case, the elements of the fractal touch each other, and the extracted images look quite different from the real data.

We represent the fractal objects as an array of straight lines, storing the start and end point of each line. Similar to the fractals in Sec. 2.2.4, all five fractals are based on a square as their initiator, consisting of four straight lines with the origin of the

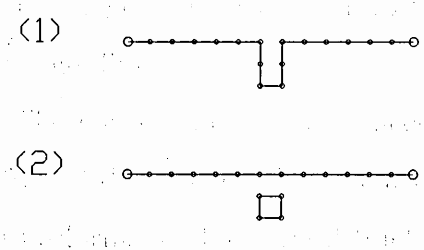

(a) $D = 1.1046$

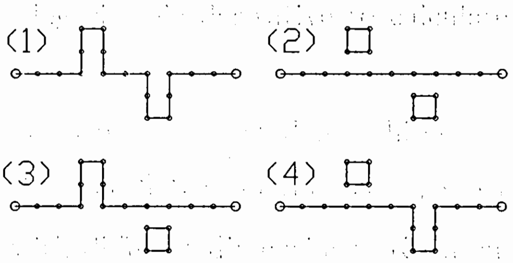

(b) $D = 1.2553$

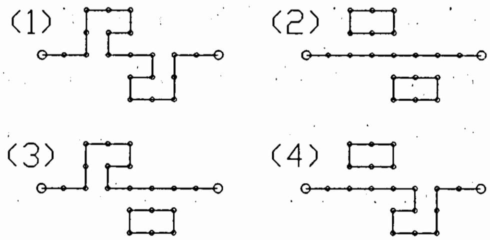

(c) $D = 1.4466$

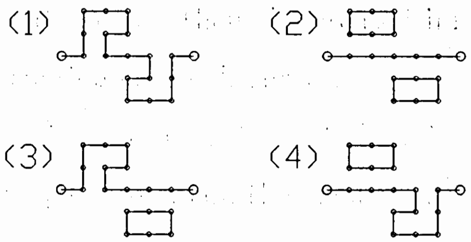

(d) $D = 1.6131$

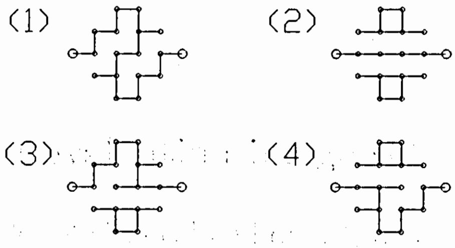

(e) $D = 1.7604$

Figure 3.10: Generators for the randomly dispersed Koch curves.

coordinate system being located at the center of the square. During each step of the self-similar cascade, all straight lines of the previous step are replaced by a generator. To get asymmetric fractal objects with varying numbers of detached islands and lakes, we randomly pick generators out of a set with the same cumulative fractal dimension, but varying degrees of dispersion (cf. Sec. 2.2.5). Each generator is chosen with the same probability. Due to this random process, two realizations of objects with the same fractal dimension may appear quite different. Fig. 3.10 shows the shapes of the generators used for the five different fractals. The range of scales of a fractal object cannot be increased continuously, but rather in discrete steps determined by the generator. It is therefore not possible to match the cut-offs of the scaling range of the real plume data both at the Batchelor scale and at the integral scale. However, we can match *the order of* the desired scaling range by selecting the proper level of the self-similar cascade, i.e. the number of times the generator is applied.

In order to apply our code to the fractal objects, it is necessary to create boundary-outline pixel images from the array of straight lines that represent the fractals. We first rotate the whole fractal object by a randomly chosen angle, which eliminates effects of the box-counting algorithm's directional preference caused by the square shape of the subdividing boxes. The rotated object is scaled to fit the resolution requirement at the smallest scale. Then, a selector square of the size of our images (i.e. 512×512 pixels) is randomly located within the much larger extent of the fractal object. The part of the object lying within the selector square is used to create one boundary-outline pixel image. Exemplary fractal objects for all five dimensions are shown in Fig. 3.11, together with a sample selector square. Note that the total extent of the fractal objects varies by approximately a factor of two to match the resolution cutoff at the pixel size. An algorithm steps along the line segments of the fractal object and calculates the locations of boundary-outline pixels. For each fractal dimension, we create 100 random realizations of the fractal and extract 10 images out of each realization. To save memory, we only accept images that contain structure. Despite our previous discussion about accepting blanks in the plume data, this is possible because completely empty images do not contribute to the ensemble-averaged coverage dimension, although they contribute to other fractal measures. Thus, a total of 1000 evaluation images are created for each of the five fractal dimensions. In Figs. 3.12 - 3.16, 12 exemplary images out of these 1000 are plotted for each of the five dimensions.

3.3.3 Quantitative assessment of algorithm accuracy

Figure 3.17 shows the results of the algorithm for the five evaluation image sets. For intermediate scales, all plots show a clear plateau matching the theoretical dimension. However, fluctuations around the correct value are evident along each plateau. According to Sreenivasan (1991), these fluctuations originate from two sources. First, the dyadic subdivision factor of the box-counting algorithm (i.e. 1/2) generally

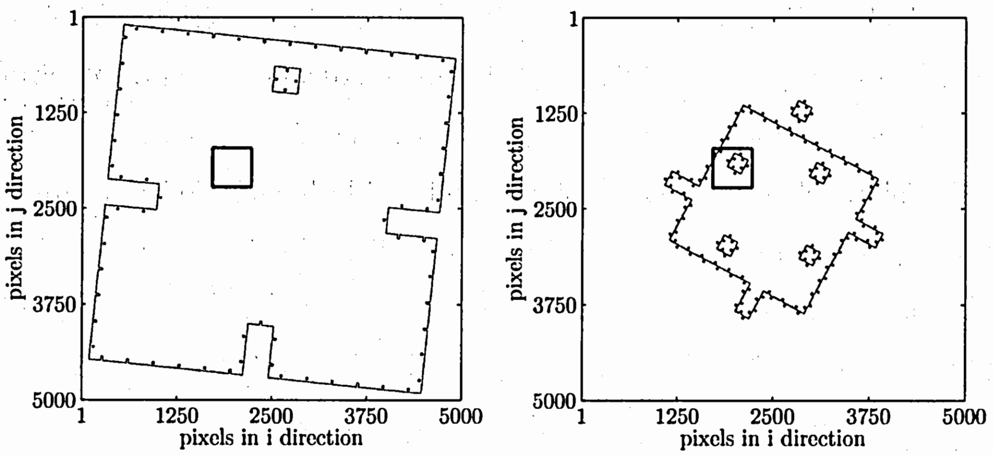
1
1250
2500
3750
5000
pixels in j direction
1
1250
2500
3750
5000
pixels in i direction

(a) $D = 1.1046$ (b) $D = 1.2553$

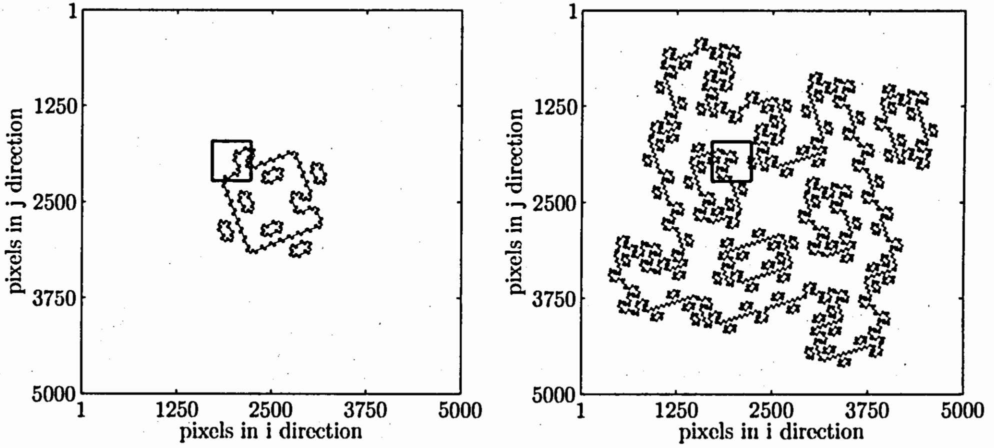
1
1250
2500
3750
5000
pixels in j direction
1
1250
2500
3750
5000
pixels in i direction

(c) $D = 1.4466$ (d) $D = 1.6131$

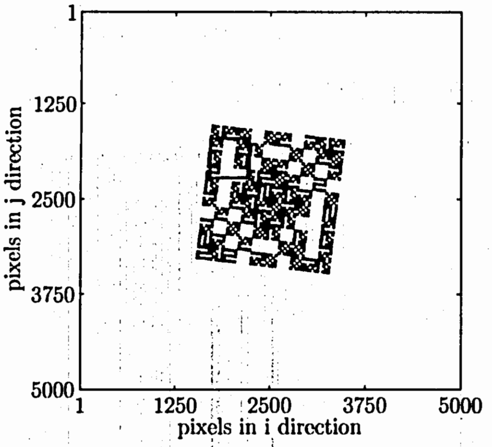
1
1250
2500
3750
5000
pixels in j direction
1
1250
2500
3750
5000
pixels in i direction

(e) $D = 1.7604$

Figure 3.11: Exemplary Koch curves for the 5 different dimensions. One 512×512 boundary image is indicated by a thick square.

does not correspond to the intrinsic subdivision factor of a particular Koch curve, determined by its generator. For example, the intrinsic subdivision factor for our $D = 1.1046$ Koch curve is $r = 1/13$. Second, the starting location of the subdivision usually does not match the starting points of straight-line elements of the Koch curve. In addition, there are two cutoffs of the plateau, at the largest and smallest scales. Such errors at the boundaries of the algorithm's scaling range are reported frequently in the literature. Miller and Dimotakis (1991) attributed these deviations to a lack of smaller features in the fractal objects at the smallest scale and to a lack of larger empty regions at the largest scale. In fact, they showed a plot of the dimension of a Cantor set, obtained from a box-counting algorithm, which looks very similar to our plots. Shepherd et al. (1992) reported fluctuations at scales below approximately two pixels, and Frederiksen et al. (1996) found significant deviations at the largest scales. Thus, we cannot expect reasonable results for the dimensions at the largest and the smallest scale.

In Tabs. 3.2 and 3.3, the rms deviation and the mean of the dimension are presented for all five dimensions and for several algorithm parameters are calculated from the middle 7 data points. The rms value is perhaps a more valuable measure than the mean dimension because positive and negative deviations do not cancel out, and larger deviations are heavier penalized.

The rms deviation, averaged over all dimensions, is smaller than 5 percent. Moreover, the error in the numerically determined dimension, averaged over the 7-point plateau, is of the order of 1 percent. The errors vary among the different dimensions, and appear greatest at intermediate dimensions. Overall, the algorithm performs very well on the evaluation images, and we therefore expect satisfactory performance for the concentration iso-surfaces.

The tables also contain information about the influence of the parameters of the algorithm. Adapting the bounding box clearly improves the results, decreasing the best rms value from 0.0428 to 0.0400 when averaging the coverage count. However, as we explained in Sec. 3.2.5, we want to retain empty regions of the concentration field to get the correct coverage fractions and lengths. Without adaptation of the bounding

Table 3.2: Root mean square (rms) of the deviation of the numerical results from the theoretical dimension over the inner 7 points. The last column shows the rms deviation averaged over all 5 dimensions.

D	1.1046	1.2553	1.4406	1.6131	1.7604	mean
1 shift average N, $\delta_b = 512$	0.0140	0.0433	0.0705	0.0650	0.0543	0.0494
average N, adapt δ_b	0.0222	0.0400	0.0677	0.0645	0.0531	0.0495
average D, $\delta_b = 512$	0.0462	0.0542	0.0545	0.0641	0.0482	0.0534
average D, adapt δ_b	0.0182	0.0422	0.0593	0.0635	0.0500	0.0466
4 shifts, min average N, $\delta_b = 512$	0.0177	0.0360	0.0595	0.0607	0.0419	0.0432
average N, adapt δ_b	0.0134	0.0316	0.0567	0.0600	0.0413	0.0406
average D, $\delta_b = 512$	0.0436	0.0502	0.0436	0.0588	0.0350	0.0462
average D, adapt δ_b	0.0172	0.0296	0.0476	0.0579	0.0358	0.0376
8 shifts, min average N, $\delta_b = 512$	**0.0197**	**0.0348**	**0.0586**	**0.0607**	**0.0404**	**0.0428**
average N, adapt δ_b	0.0136	0.0309	0.0557	0.0599	0.0399	0.0400
average D, $\delta_b = 512$	0.0462	0.0525	0.0419	0.0581	0.0338	0.0465
average D, adapt δ_b	0.0187	0.0285	0.0460	0.0574	0.0342	0.0370
8 shifts, mean average N, $\delta_b = 512$	0.0525	0.0594	0.0807	0.0828	0.0589	0.0669
average N, adapt δ_b	0.0547	0.0600	0.0807	0.0828	0.0589	0.0674
average D, $\delta_b = 512$	0.0997	0.1021	0.0771	0.0847	0.0582	0.0844
average D, adapt δ_b	0.0939	0.1000	0.0771	0.0845	0.0582	0.0827

box, ensemble-averaging the single-image coverage count yields slightly better rms deviations and much better mean dimensions than ensemble-averaging the single-image coverage dimensions. Shifting the starting location of the binary subdivision has a beneficial effect on the results. However, the improvements diminish as we go to more shifts. Therefore, the significant computational cost of more than eight shifts is not justified. Finally, we have shown that in the case of shifting the starting location, it is better to take the minimum of the coverage counts. In fact, taking the average of all shifts yields worse results than no shifting. Based on these results, we calculate the ensemble average of the minimum coverage count for eight shifts without adapting the bounding box when evaluating the plume concentration images. The row corresponding to this set of procedures is highlighted in Tabs. 3.2 and 3.3 by bold digits. The results of these calculations are presented in the next chapter.

Table 3.3: Mean dimension, averaged over the inner 7-point plateau. The last column shows the absolute deviation from the theoretical dimension, averaged over all 5 dimensions.

D	1.1046	1.2553	1.4406	1.6131	1.7604	mean error
1 shift average N, $\delta_b = 512$	1.0997	1.2434	1.4384	1.5871	1.7638	0.97 %
average N, adapt δ_b	1.0871	1.2347	1.4361	1.5857	1.7632	1.46 %
average D, $\delta_b = 512$	1.0660	1.2040	1.4179	1.5665	1.7479	3.43 %
average D, adapt δ_b	1.1007	1.2248	1.4231	1.5709	1.7490	1.32 %
4 shifts, min average N, $\delta_b = 512$	1.1152	1.2579	1.4445	1.5937	1.7651	0.82 %
average N, adapt δ_b	1.1026	1.2483	1.4416	1.5916	1.7645	0.71 %
average D, $\delta_b = 512$	1.0789	1.2172	1.4242	1.5743	1.7494	2.60 %
average D, adapt δ_b	1.1165	1.2432	1.4308	1.5803	1.7506	1.53 %
8 shifts, min average N, $\delta_b = 512$	**1.1172**	**1.2606**	**1.4469**	**1.5953**	**1.7653**	**0.94 %**
average N, adapt δ_b	1.1045	1.2507	1.4440	1.5933	1.7647	0.64 %
average D, $\delta_b = 512$	1.0805	1.2200	1.4267	1.5763	1.7496	2.42 %
average D, adapt δ_b	1.1198	1.2472	1.4333	1.5825	1.7508	1.42 %
8 shifts, mean average N, $\delta_b = 512$	1.0590	1.2072	1.4181	1.5792	1.7574	3.06 %
average N, adapt δ_b	1.0573	1.2064	1.4181	1.5790	1.7574	3.12 %
average D, $\delta_b = 512$	1.0171	1.1586	1.3903	1.5553	1.7388	6.28 %
average D, adapt δ_b	1.0219	1.1604	1.3903	1.5560	1.7388	6.13 %

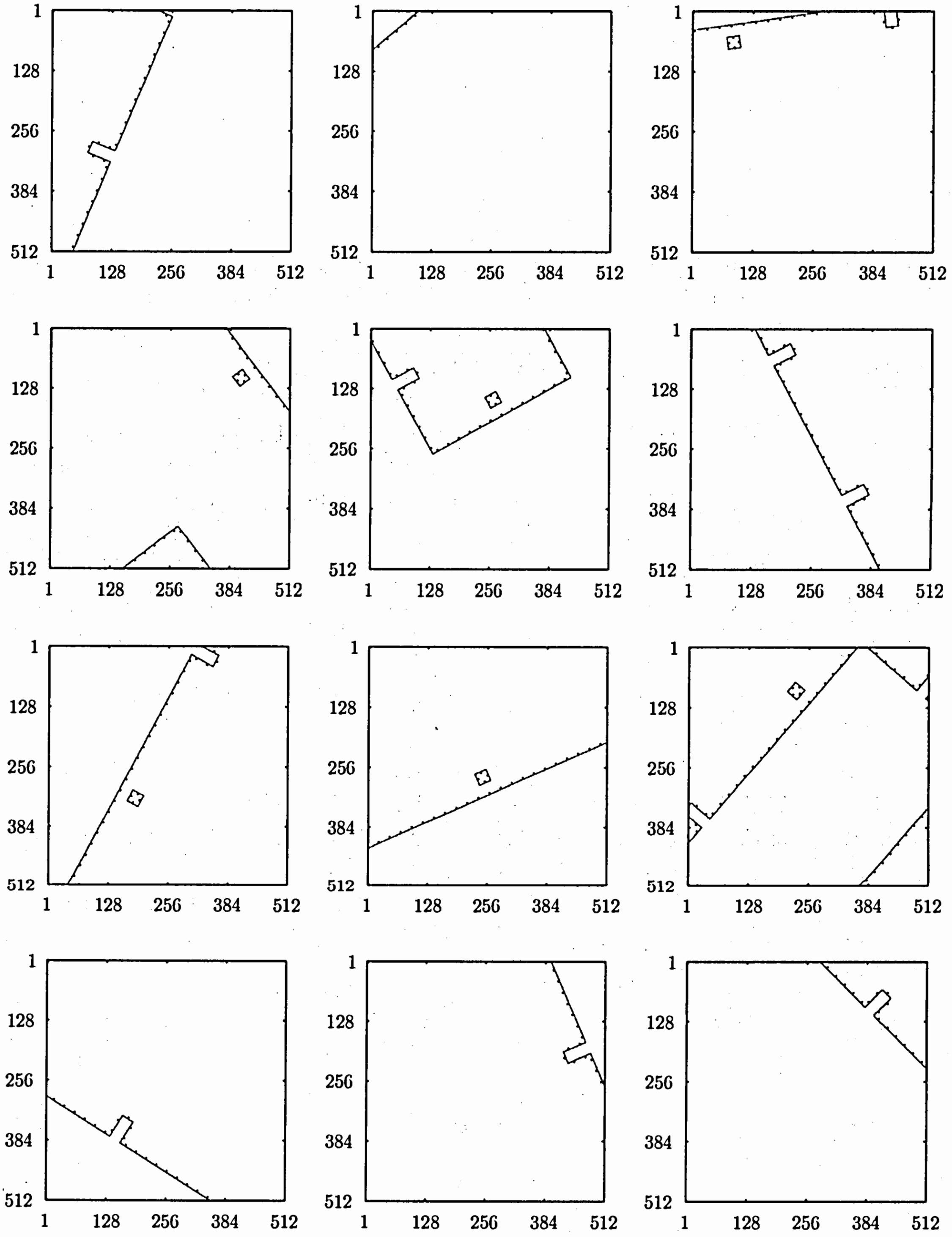
1
128
256
384
512
1
128
256
384
512

Figure 3.12: 12 sample images from the set of 1000 evaluation images for $D = 1.1046$.

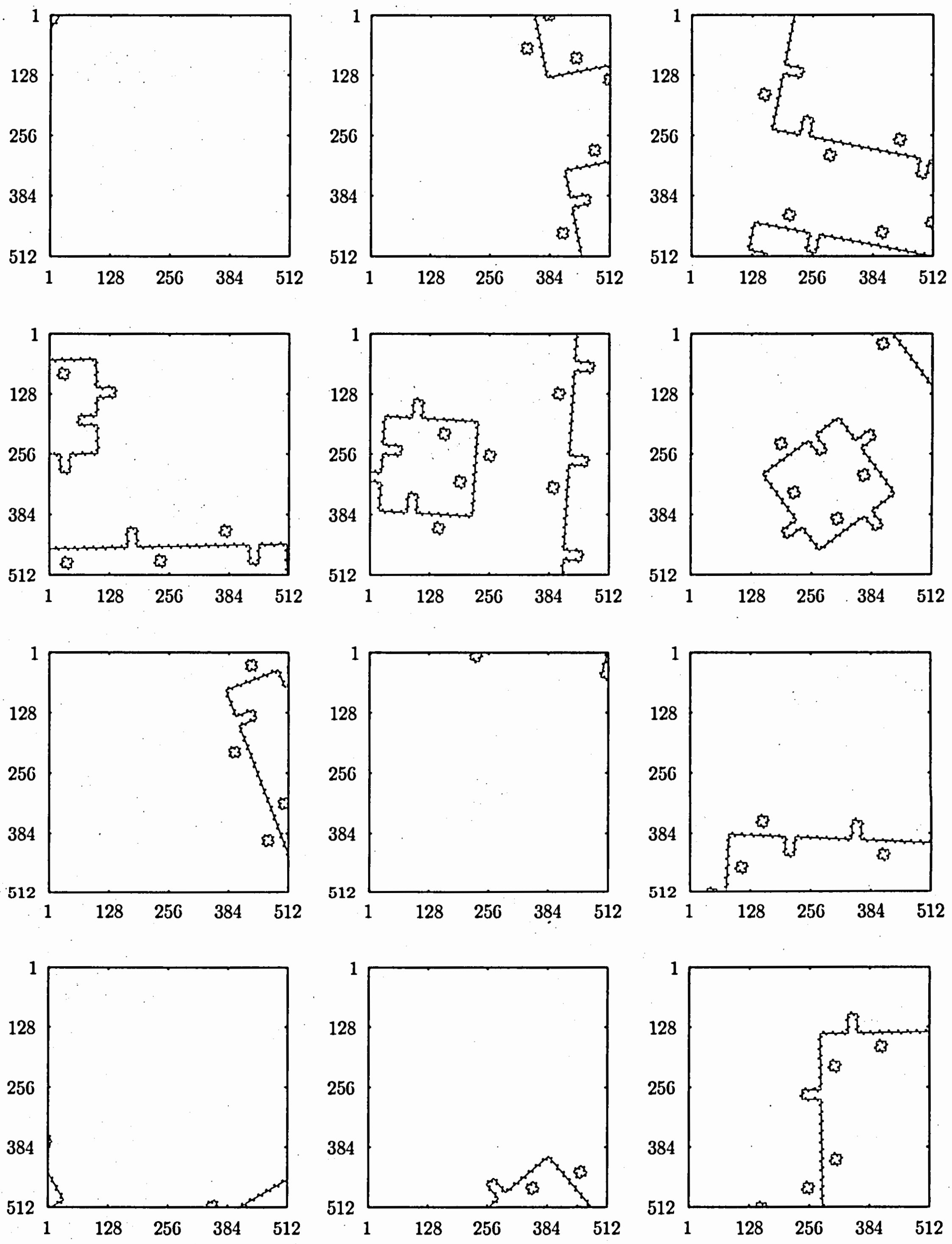

Figure 3.13: 12 sample images from the set of 1000 evaluation images for $D = 1.2553$.

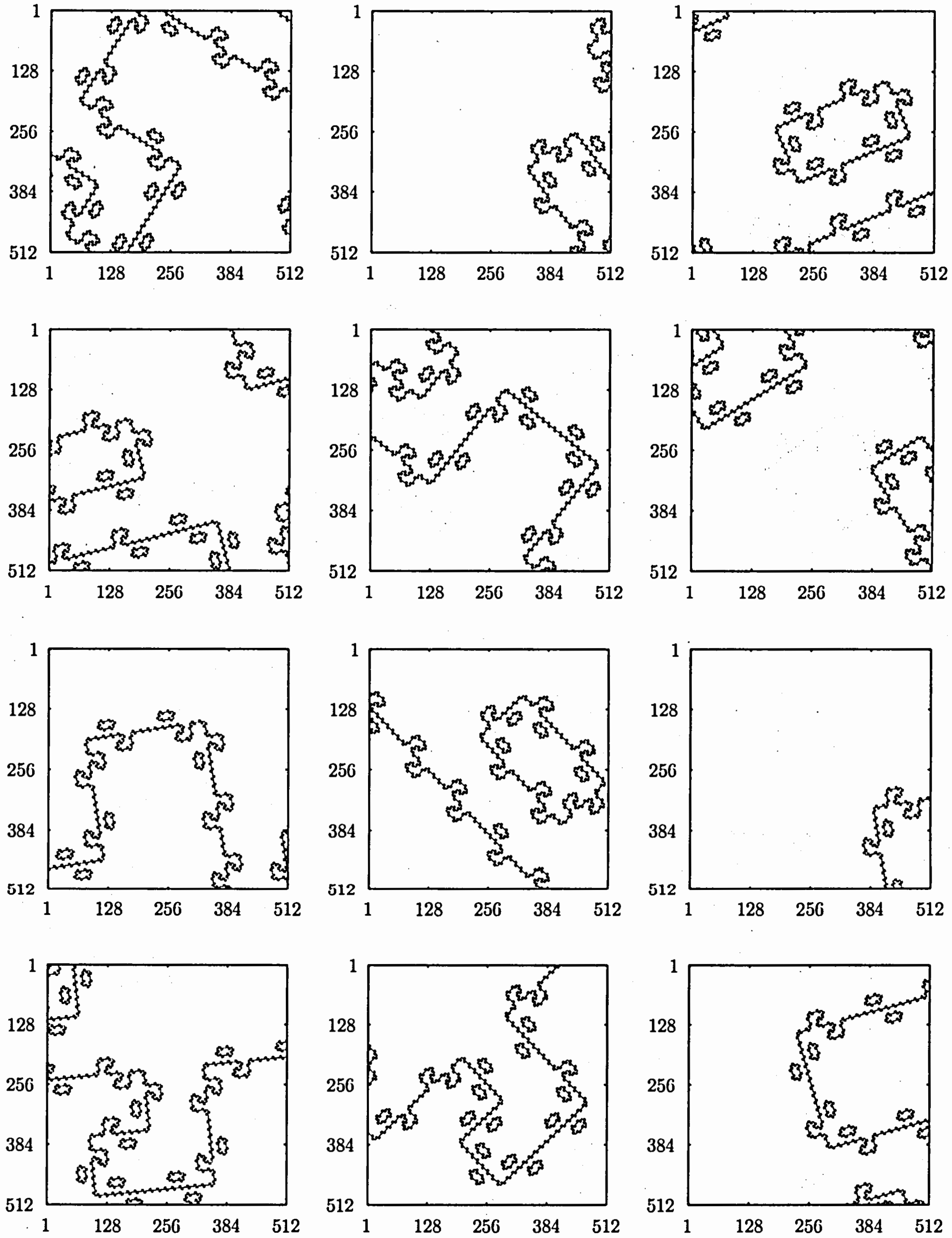

Figure 3.14: 12 sample images from the set of 1000 evaluation images for $D = 1.4466$.

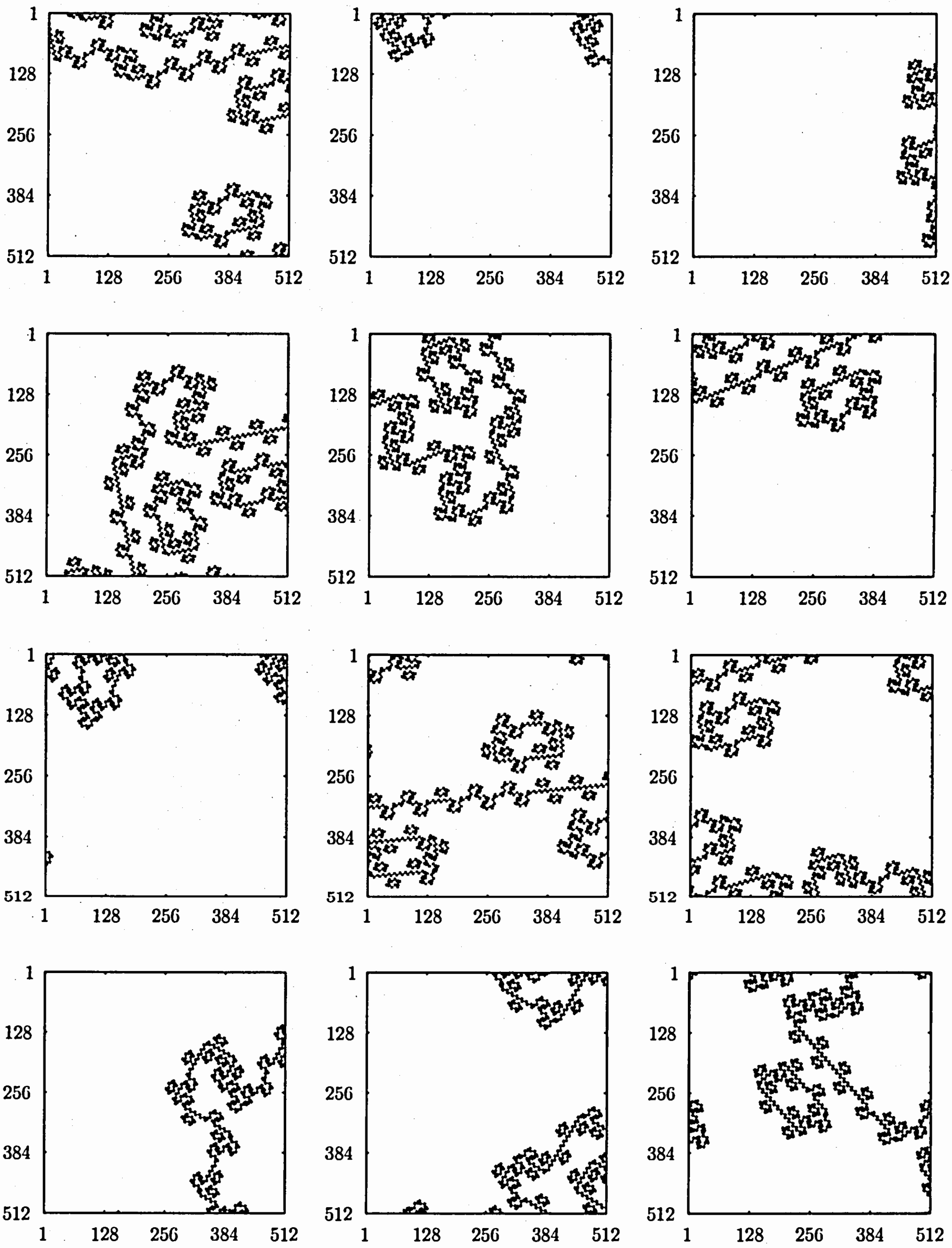
1
128
256
384
512
1
128
256
384
512

Figure 3.15: 12 sample images from the set of 1000 evaluation images for $D = 1.6131$.

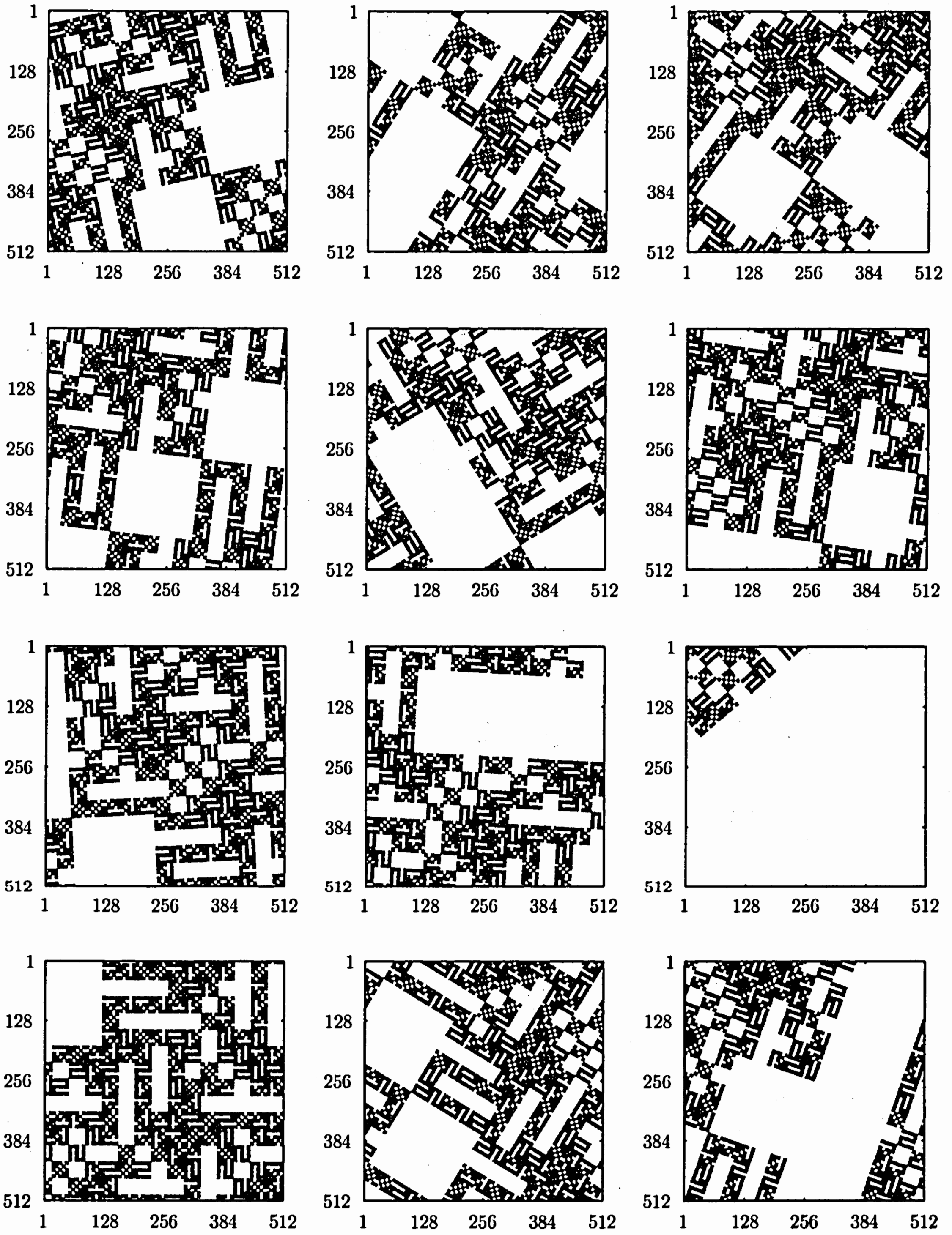
1
128
256
384
512

Figure 3.16: 12 sample images from the set of 1000 evaluation images for $D = 1.7604$.

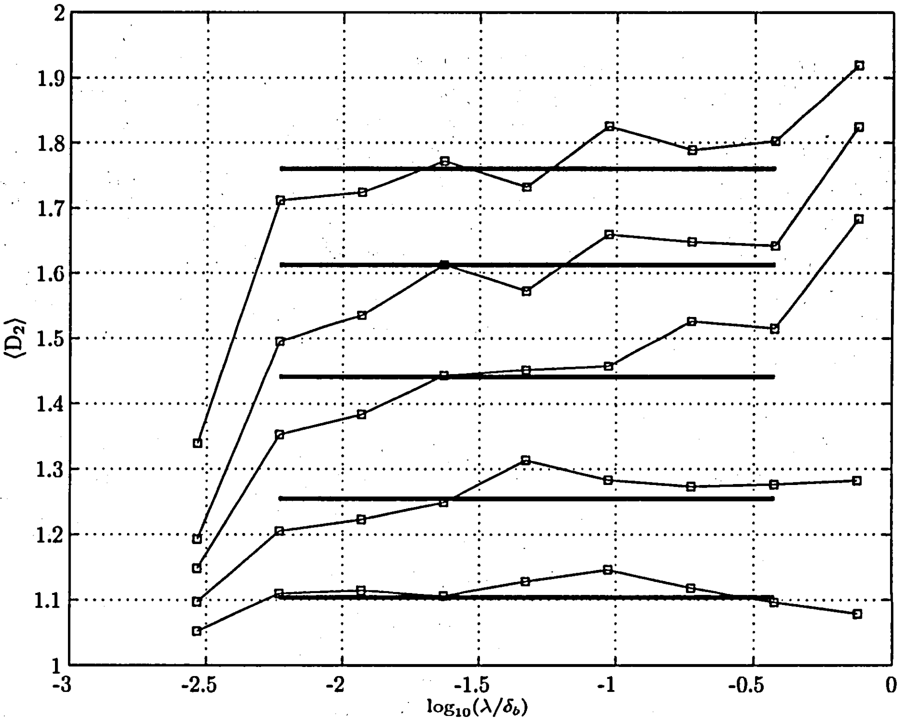

Figure 3.17: Box-counting dimensions calculated via the numerical method, for the five evaluation images sets. The theoretical fractal dimensions are indicated by thick horizontal lines over the range in which the algorithm accuracy is to be evaluated.

CHAPTER 4

Results and discussion

4.1 Statistics of the concentration field

Before analyzing the concentration iso-surfaces in terms of fractal geometry, it is helpful to examine the statistical properties of the concentration fields. After the calibration of the raw images and normalization by the source concentration, C_{source}, (see Sec. 3.2.1 for the exact approach), each data set consists of $n_{max} = 6000$ concentration images, $C^*_{i,j}$, with $0 \leq C^* \leq 1$, $1 \leq i \leq 512$, and $1 \leq j \leq 512$ (see Fig. 3.2 for a sample concentration image). Note that although C^* is normalized by the source concentration, we will refer to this quantity as an absolute concentration, in contrast to a further normalized concentration defined later is this section. The data sets were taken at four distances, x, downstream of the source, namely at $x = 250$, 500, 1000, and 2000 mm. The images were located symmetrically about the plume centerline. Thus, it is important to keep in mind that the concentration statistics, as well as the fractal measures, represent the conditions in proximity to the plume centerline.

For each pixel (i, j) in a data set, the 6000 images correspond to a concentration time record, which is temporally under-resolved. Exemplary time records, for four distances from the source, are shown in Fig. 4.1. As expected from the theoretical discussion in Sec. 2.1.7, the instantaneous concentration fluctuates greatly in time, exhibiting long periods of low concentration, which are interrupted by brief, high peak concentrations. While this intermittent behavior is qualitatively similar at all four downstream locations, the magnitudes of the peaks drop significantly with increasing distance from the source. For $x = 250$ mm, the highest peaks are slightly below the

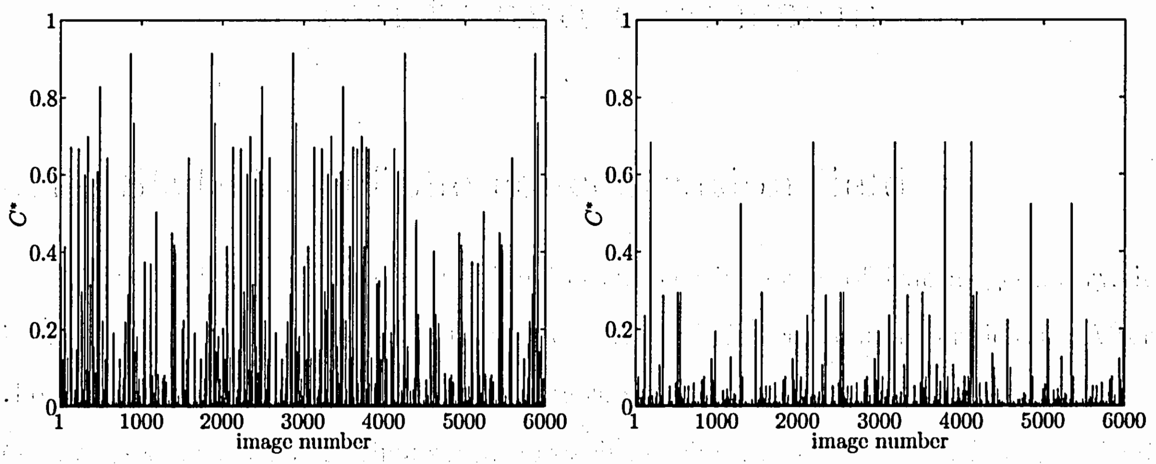

(a) $x = 250$ mm (b) $x = 500$ mm

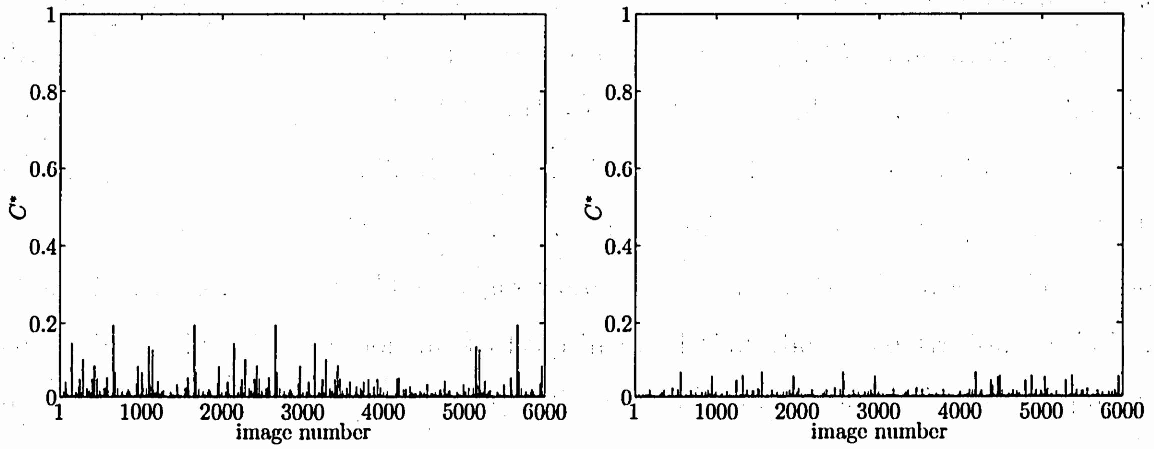

(c) $x = 1000$ mm (d) $x = 2000$ mm

Figure 4.1: Exemplary normalized single-pixel concentration time series, C^*, at four distances, x, from the source. The normalized instantaneous concentration fluctuates greatly between consecutive images. Both the mean concentration and the intensity of the fluctuations drop rapidly with increasing distance from the source.

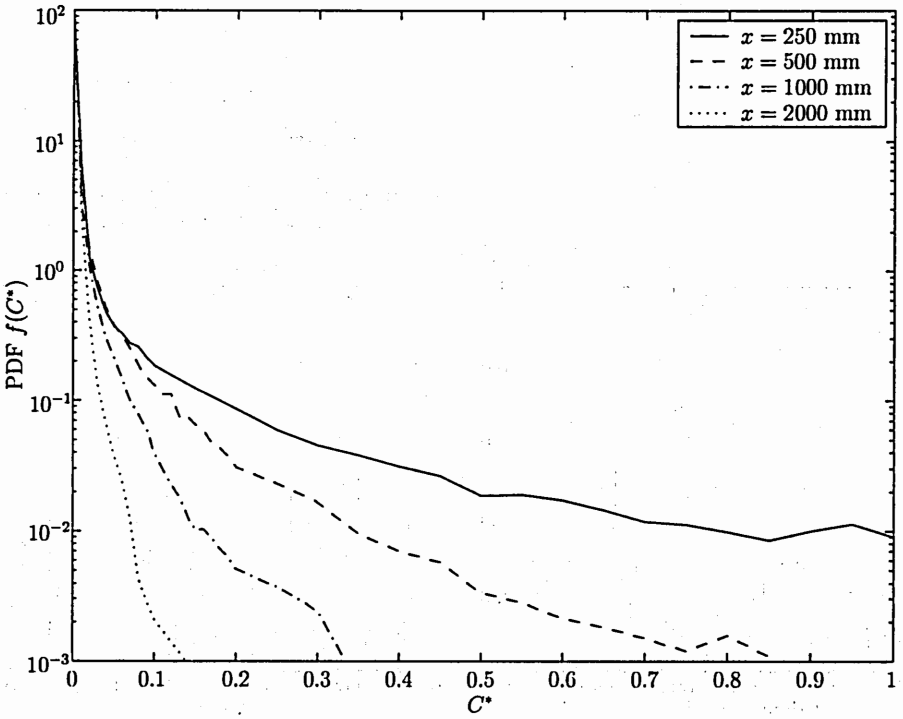

Figure 4.2: PDFs $f(C^*)$ of the instantaneous concentration fields for four distances, x, from the source. With increasing distance from the source, the concentration distributions shift towards the lower boundary of the normalized concentration range.

source concentration. For $x = 2000$ mm, however, the highest peaks reach only about a tenth of the source concentration.

The concentration PDFs $f(C^*)$ show the fluctuation distributions and further reveal the variation with downstream distance. Fig. 4.2 shows the concentration PDFs that correspond to the concentration time records as given in Fig. 4.1. The plots indicate that with increasing distance from the source, the concentration distribution shifts towards the lower end of the possible concentration range. Thus, the concentration mean and standard deviation decrease and it becomes less likely to encounter high concentration peaks. All four PDFs exhibit a sharp and narrow peak towards zero concentration, followed by a steep decrease and long tails towards higher concentrations. The described profile reflects a characteristic property of the underlying concentration field: while the mean concentration is extremely low, the standard deviation is an order of magnitude higher, and the highest instantaneous peaks are

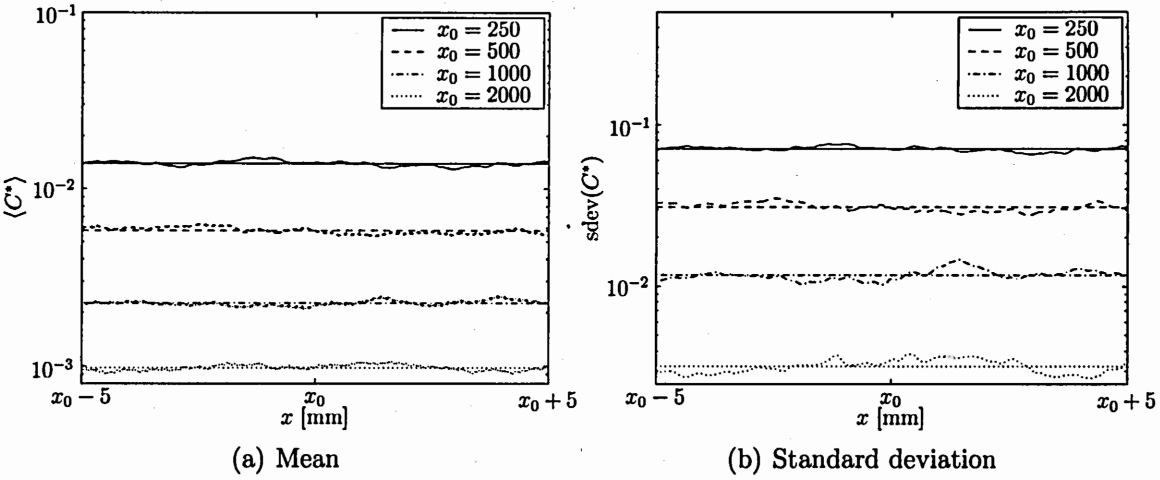

(a) Mean

(b) Standard deviation

Figure 4.3: Profiles of concentration mean and standard deviation in the streamwise direction, averaged over 6000 images and the vertical direction (512 pixel columns), for four distances, x, from the source. Mean values additionally averaged in the streamwise direction are indicated by the straight lines. The concentration mean and standard deviation are approximately uniform in the streamwise direction across the image region.

another order of magnitude higher. These properties represent a major experimental difficulty because events of very high concentration are extremely rare, but they affect the mean and standard deviation significantly. Therefore, it is necessary to consider very long concentration records to statistically capture those rare events. As the mean concentration is very close to zero, a high resolution of the concentration measurements is necessary. Simultaneously, the highest peaks require a wide dynamical range of the measurement technique. In that respect, the concentration fields originating from iso-kinetic sources are experimentally more demanding than fields that are generated, for example, by a jet, where the concentration fluctuations are less intermittent. The spectra of concentration fields typical for our study have been examined by Dasi and Webster (2003).

To ensure a sufficient number of concentration values in the calculation of the statistics, we performed not only a time average over the 6000 images, but also a spatial average over all 512 × 512 pixels of the images. Therefore, the statistics of each data set are based on over 1.5 billion individual concentration values. Of course, spatial averaging requires a uniform distribution of the concentration statistics across

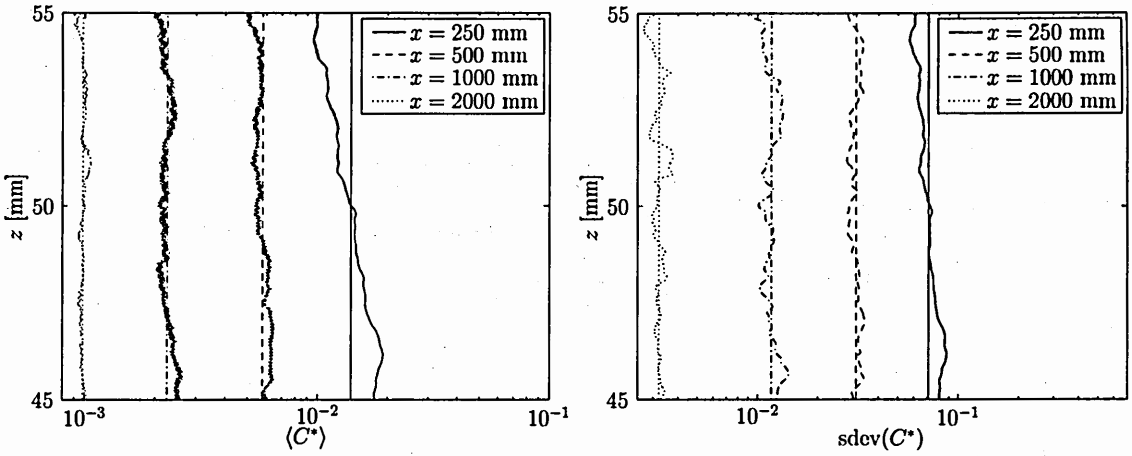

(a) Mean (b) Standard deviation

Figure 4.4: Profiles of concentration mean and standard deviation in the vertical direction, averaged over 6000 images and the streamwise direction (512 pixel rows) for four distances, x, from the source. Mean values additionally averaged in the vertical direction are indicated by the straight lines. Except for the $x = 250$ mm case, the concentration mean and standard deviation are approximately uniform in the vertical direction across the image region.

the image regions. According to the simple continuous point source model from Sec. 2.1.7, we expect the mean and standard deviation to decrease in the streamwise direction with increasing distance from the source, and in the cross-stream directions with increasing distance from the plume centerline. It can be expected that the extent of the individual concentration fields (approx. 10×10 mm) is negligible compared to the considered dimensions in the x direction. However, the fields are about a tenth of the water depth, and thus are not negligible in the z direction. We calculated distributions of mean concentration and standard deviation in both the x and z directions by averaging over 6000 images and the direction perpendicular to the profile direction. The results are shown in Figs. 4.3 and 4.4. As expected, the concentration is homogenous in streamwise direction and, in particular, does not decrease with distance from the source. In the cross-stream direction, in proximity to the source, there is a noticeable inhomogeneity in the mean concentration and standard deviation profiles, but the inhomogeneity vanishes with increasing x. One possible explanation is that the plume is narrowest close to the source and thus could be of size comparable to the image size. The shape of the inhomogeneous profiles, however, is not symmetric

Table 4.1: Statistics of the concentration fields and values of the concentration thresholds used to extract iso-surfaces, at four distances, x, from the source.

x	[mm]	250	500	1000	2000
C_{source}	[μg/L]	101.61	101.61	202.51	501.76
$\langle C^* \rangle$	-	0.0139	0.0058	0.0023	0.0010
sdev(C^*)	-	0.0712	0.0311	0.0117	0.0032
$C^*_{th,1} = \langle C^* \rangle + 1 \cdot \mathrm{sdev}(C^*)$	-	0.0851	0.0368	0.0140	0.0042
$C^*_{th,2} = \langle C^* \rangle + 2 \cdot \mathrm{sdev}(C^*)$	-	0.1563	0.0679	0.0258	0.0074
$C^*_{th,3} = \langle C^* \rangle + 3 \cdot \mathrm{sdev}(C^*)$	-	0.2274	0.0990	0.0375	0.0106
$C^*_{th,5} = \langle C^* \rangle + 5 \cdot \mathrm{sdev}(C^*)$	-	0.3697	0.1611	0.0610	0.0170
$C^*_{th,7} = \langle C^* \rangle + 7 \cdot \mathrm{sdev}(C^*)$	-	0.5120	0.2232	0.0845	0.0235

about the expected plume centerline (i.e. $z = 50$ mm). Thus, it must be concluded that the turbulent mixing was not symmetric in the vertical direction due to the variation in the mean and fluctuating velocity in the boundary layer. In comparison to the changes of the mean and standard deviation among the four data locations, however, we may consider the statistics to be approximately uniform across each image field.

The resulting concentration statistics, along with the corresponding source concentrations, are summarized in Tab. 4.1. The mean and standard deviation decrease rapidly with increasing x. This creates a question of how to compare the iso-surface geometry at different downstream locations. The challenge of a comparison is to define concentration thresholds that identify reasonable iso-surfaces at all of the downstream locations. But, concentrations that are around the mean, and thus very common, at $x = 250$ mm, represent very rare peak events at $x = 2000$ mm. This effect makes it impossible to use absolute concentrations for comparisons, and thus calls for a normalization of the concentration field by a quantity that reflects the systematic changes in the concentration fields with x. Indeed, if we normalize the concentration fluctuations by the standard deviation, according to $(C - \langle C \rangle)/\mathrm{sdev}(C)$, the corresponding concentration PDFs at all four downstream locations appear similar, as can be seen in Fig. 4.5. Note that the concentration PDF is far from Gaussian, and deviates significantly from the concentration PDF of a turbulent jet as reported for example by Catrakis and Dimotakis (1996). Because of the similarity of the normalized PDFs

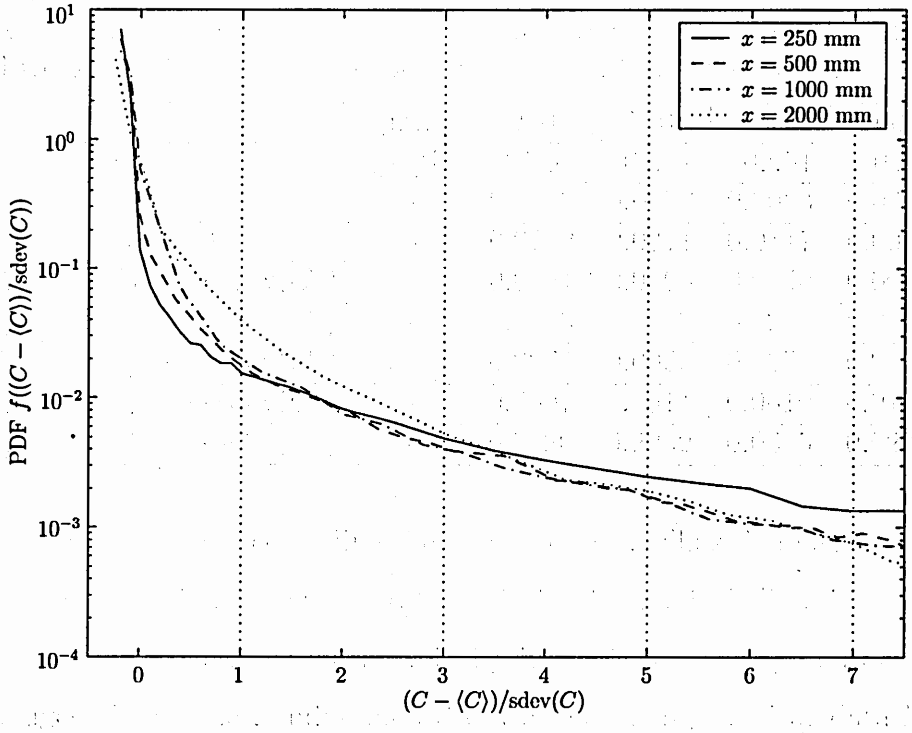

Figure 4.5: PDFs of the fluctuating concentration fields, normalized by the intensity of the fluctuations, sdev(C), for four distances, x, from the source. When normalized, the PDFs at different distances appear similar. The four different concentration thresholds used to extract iso-surfaces are indicated by vertical dotted lines.

at various x, it is reasonable to compare iso-surfaces that are defined by equal magnitudes of the normalized fluctuations. Thus, we define several concentration thresholds of varying levels according to

$$C^*_{th,n} = \langle C^* \rangle + n \cdot \mathrm{sdev}(C^*). \tag{4.1}$$

For the thresholds utilized in the present study, the corresponding absolute concentration values are given in Tab. 4.1. In addition, the thresholds are indicated in the concentration PDF plot of Fig. 4.5. They are chosen to cover a wide range of concentrations. For example, in the case of $x = 250$ mm, the instantaneous concentrations fluctuate roughly between zero and the source concentration. The thresholds, $C_{th,1}$ - $C_{th,7}$, presented in Tab. 4.1, cover almost half of this range. Furthermore, approximately 99 percent of all concentration values are below the highest threshold, $C_{th,7}$. Thus, the threshold levels allow us to make quantitative statements about the iso-surface geometry over a wide range of concentration values that might be of interest

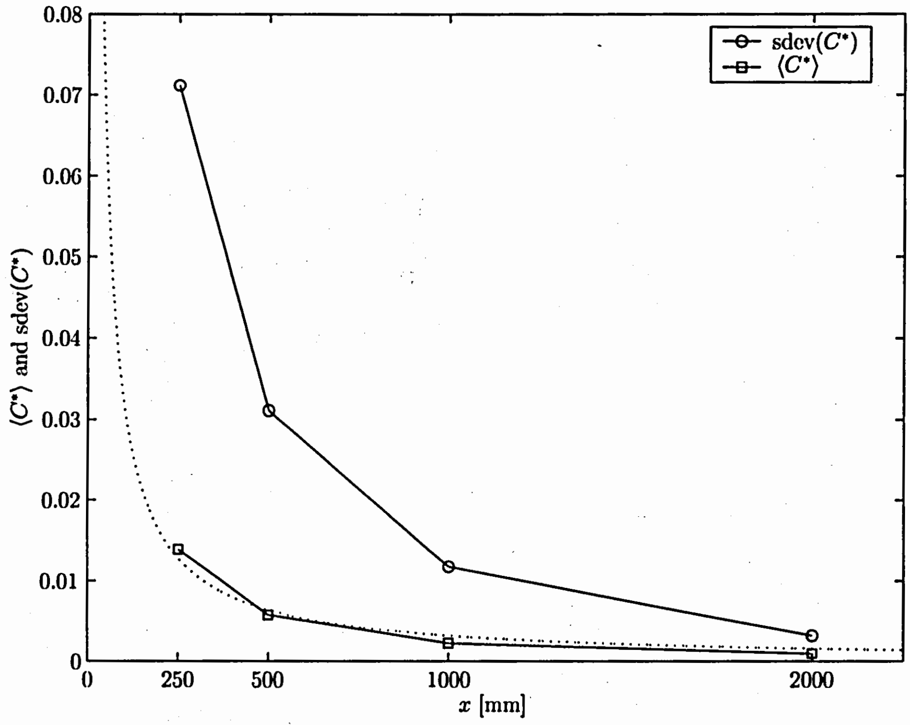

Figure 4.6: Concentration mean, $\langle C^* \rangle$, and standard deviation, sdev(C^*), as functions of distance, x, from the source. Both the mean and standard deviation drop rapidly with increasing distance from the source. The theoretical (const./x) dependence of the mean concentration field from a continuous point source is indicated by a dotted line.

in particular applications.

The variation of the concentration statistics with distance from the source is visualized in Fig. 4.6. Again we see that close to the source the concentration standard deviation is much higher than the mean, but decreases more rapidly with x. As proposed by the continuous point source model, the mean concentration can be reasonably approximated by a (const./x) relation. For the dotted line in Fig. 4.6, the constant has a value of $K = 3.2$ mm. From Eq. 2.34, we can thereby derive a very crude estimate for the eddy diffusivity

$$\kappa_T \sim \frac{\dot{V}_{source}}{4\pi K} \approx 4 \times 10^{-5}\ \mathrm{m}^2/\mathrm{s}. \tag{4.2}$$

This value is more than three orders of magnitude larger than the molecular diffusivity, and emphasizes the efficiency of the turbulent mixing process. In connection with the definition of a 99 percent diameter of the plume, δ, based on the mean concentration distribution, this result can be used to roughly estimate the cross-stream extent of the plume to be $\delta \sim 4$ cm at $x = 250$ mm, $\delta \sim 6$ cm at $x = 500$ mm, $\delta \sim 9$ cm at $x = 1000$ mm, and $\delta \sim 13$ cm at $x = 2000$ mm. Remember that the theoretical model corresponds to an unbounded plume and notice that the estimate for the last location exceeds the water depth. However, the rough estimate at $x = 250$ mm would explain the slight inhomogeneity of the mean concentration because the plume is only about four times as wide as the image field. For the fractal analysis of the concentration field, such estimates might prove important qualitatively, as we only have a zoomed-in view of the field, and thus we need to set for example surface area results in relation to the total extent of the plume.

4.2 Geometry of iso-surfaces

4.2.1 Qualitative description based on sample images

Fractal measures aim to describe and quantify the geometry of concentration iso-surfaces. In order to be able to understand and interpret the *quantitative* results presented later on in this chapter, it is helpful to first develop a *qualitative* picture of the iso-surfaces. For that purpose, Figs. 4.7 - 4.10 each show twelve sample boundary-pixel images from the data sets at four distances, x, from the source. The iso-surfaces contained in the images are defined by the concentration threshold $C^*_{th,3} = \langle C^* \rangle + 3 \cdot \text{sdev}(C^*)$. It is important to note that the sample images are not chosen to be representative for the whole data sets. Rather, we simply plotted the first twelve consecutive images of each data set.

The images clearly reveal the essential features of the iso-surface structure and the underlying concentration fields. First, the dye filaments appear randomly distributed in space and move chaotically in time. Second, the dye filaments exhibit a highly intermittent distribution among large regions of clean fluid. While some images are densely covered by iso-surfaces, a significant fraction of the images contains little or even no iso-surface structure. Third, the iso-surface structure represents the large range of scales involved in the concentration fields. Dispersed iso-surface objects exist from overall sizes larger than the image size (probably of the size of the integral scale) to sizes of only a few pixels (of the order of the Batchelor scale). Moreover, convolution of the iso-surfaces can be observed at a wide range of scales, which may be described as a combination of large-scale folding and small-scale wrinkling (Catrakis, 2000). Moreover, it is interesting to observe that some iso-surfaces are highly convoluted while others have completely smooth shapes.

We have a zoomed-in view and do not resolve the largest scales of the plume. The concentration iso-surfaces in a turbulent boundary layer therefore appear systematically different from the iso-surfaces in the cross section of a turbulent jet, which have been analyzed frequently in the literature, e.g. by Catrakis and Dimotakis (1996). The current iso-surfaces are much more sparse, and single images contain significantly less structure. While different realizations of jet iso-surface images look alike, here consecutive images may look completely different. It must be concluded that single images from our data sets only contain a small fraction of the geometrical information that is contained in the field. Thus, we need to average over a large number of images to obtain a complete description.

When comparing the sample images of the four data sets, one can observe changes in the iso-surface geometry with increasing distance from the source. Close to the source, the iso-surfaces appear more intermittent, i.e. the few images containing structure are typically followed by many mostly empty images. Farther away from the source, a higher fraction of the images tends to contain iso-surface structure, but typically less structure than the "richest" images close to the source. Overall, this corresponds to a homogenization of the concentration field, from few filaments of very high concentration to more, and better distributed, filaments of lower concentration. The shape of the iso-surfaces also changes downstream. Close to the source, they are typically large, complex, and highly convoluted objects. Farther downstream, the structure appears as several smaller filaments, with significantly smoother boundaries. This evolution is consistent with the homogenization of the plume and the action of molecular diffusion, which continues to smear out steep gradients.

4.2.2 Quantitative description based on fractal geometry

This section presents quantitative analysis of the concentration iso-surfaces including the fractal dimension and other fractal measures that have been presented analytically in Sec. 2.2.7, and in discretized notation in Sec. 3.2.6. The goal is to find quantitative support for the qualitative discussion in the previous section.

All fractal measures will be presented in figures containing four subplots corresponding to the four distances, x, from the source. Each subplot shows the particular fractal measure as a function of scale, λ/δ_b (i.e. normalized by the size of the bounding box), for several concentration thresholds, $C^*_{th,n} = \langle C^* \rangle + n \cdot \mathrm{sdev}(C^*)$. All plots include the thresholds $C^*_{th,3}$, $C^*_{th,5}$, and $C^*_{th,7}$. As explained in Sec. 3.2.4, the signal to noise ratio for the $x = 1000$ and 2000 mm cases is rather low, and thus it was

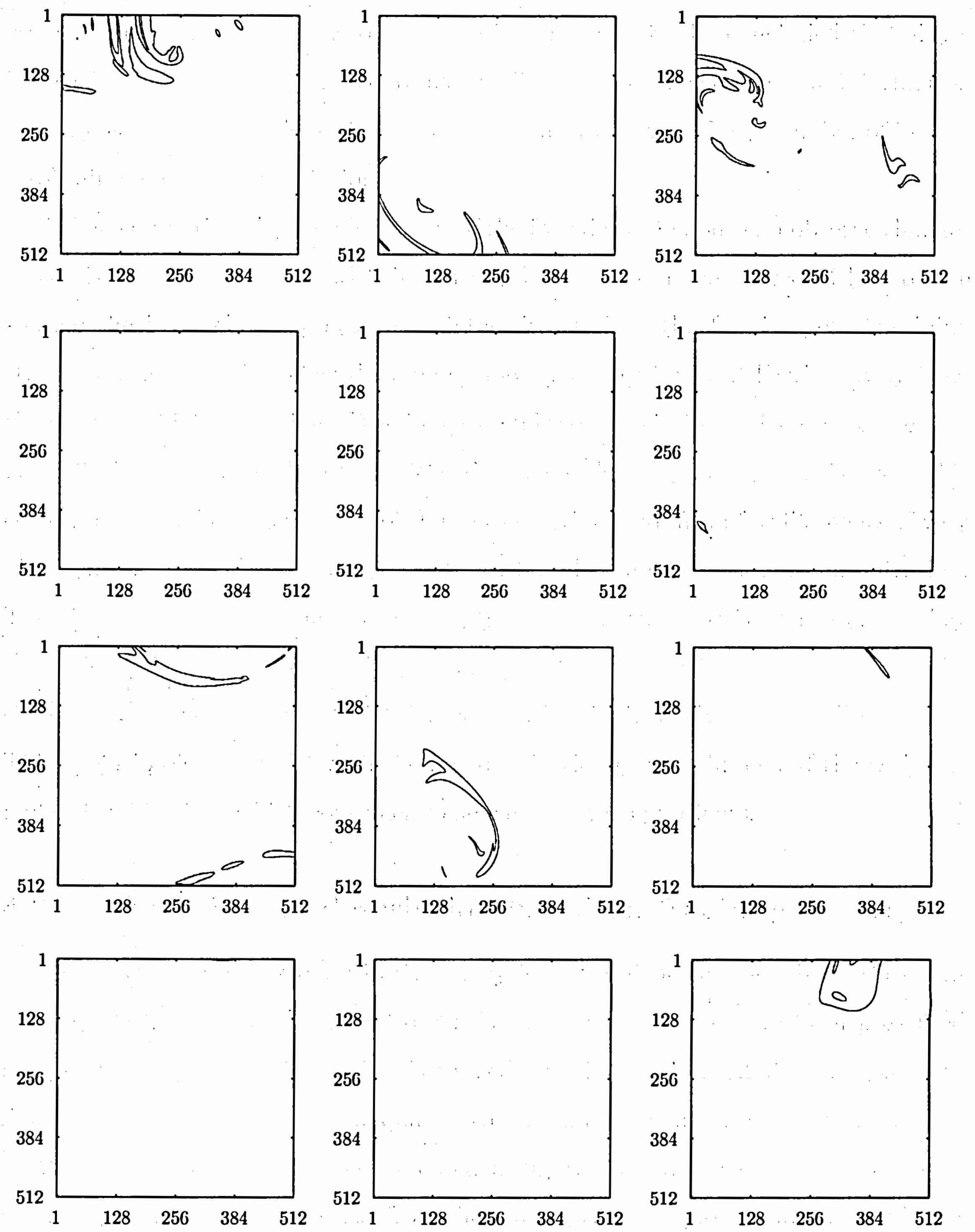

Figure 4.7: 12 consecutive samples from the set of 6000 boundary-outline images at $x = 250$ mm from the source for a concentration threshold of $C^*_{th,3} = \langle C^* \rangle + 3 \cdot \mathrm{sdev}(C^*)$. The streamwise direction within the images is from left to right. The images were captured from left to right, and from top to bottom of the page.

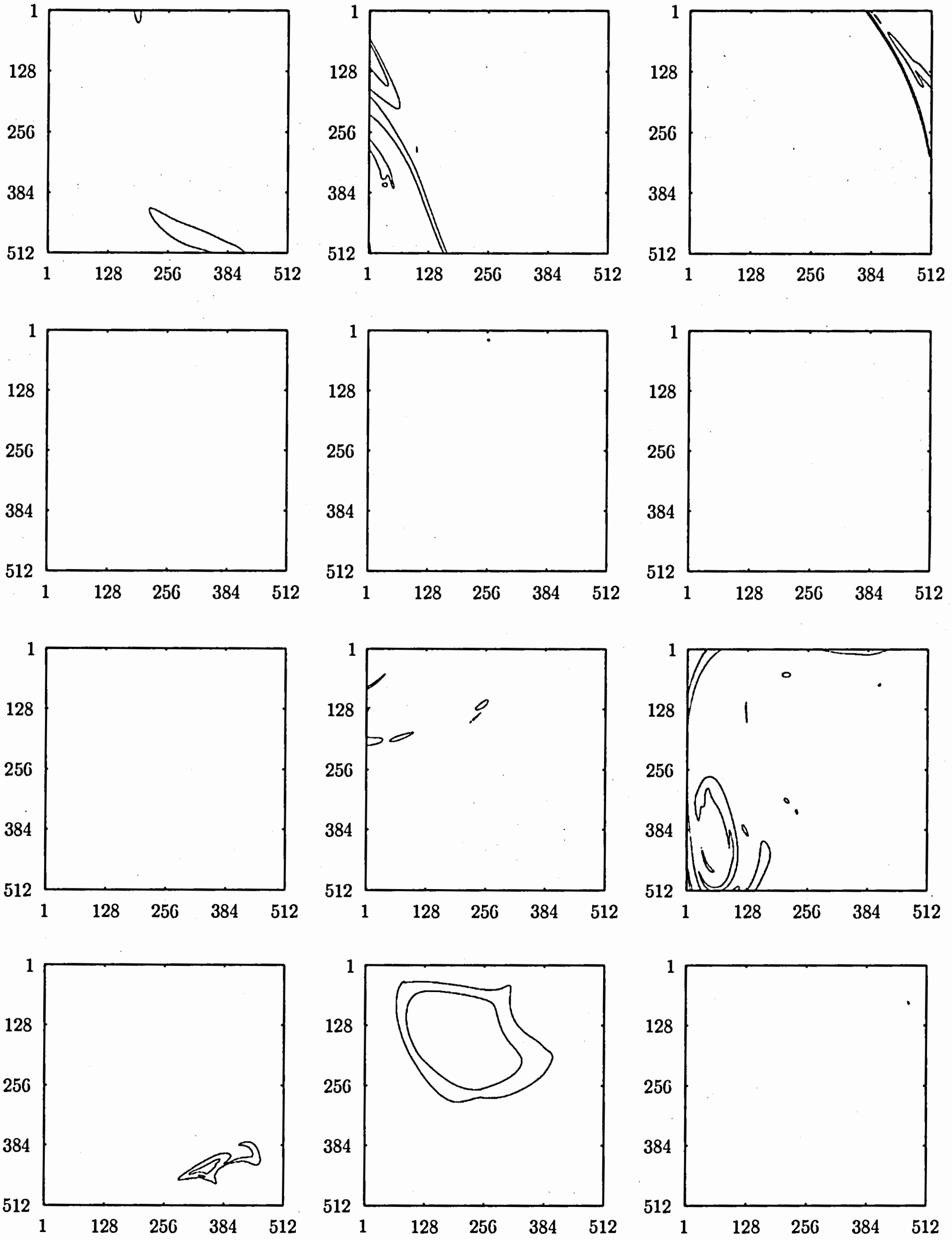

Figure 4.8: 12 consecutive samples from the set of 6000 boundary-outline images at $x = 500$ mm from the source for a concentration threshold of $C^*_{th,3} = \langle C^* \rangle + 3 \cdot \mathrm{sdev}(C^*)$. The streamwise direction within the images is from left to right. The images were captured from left to right, and from top to bottom of the page.

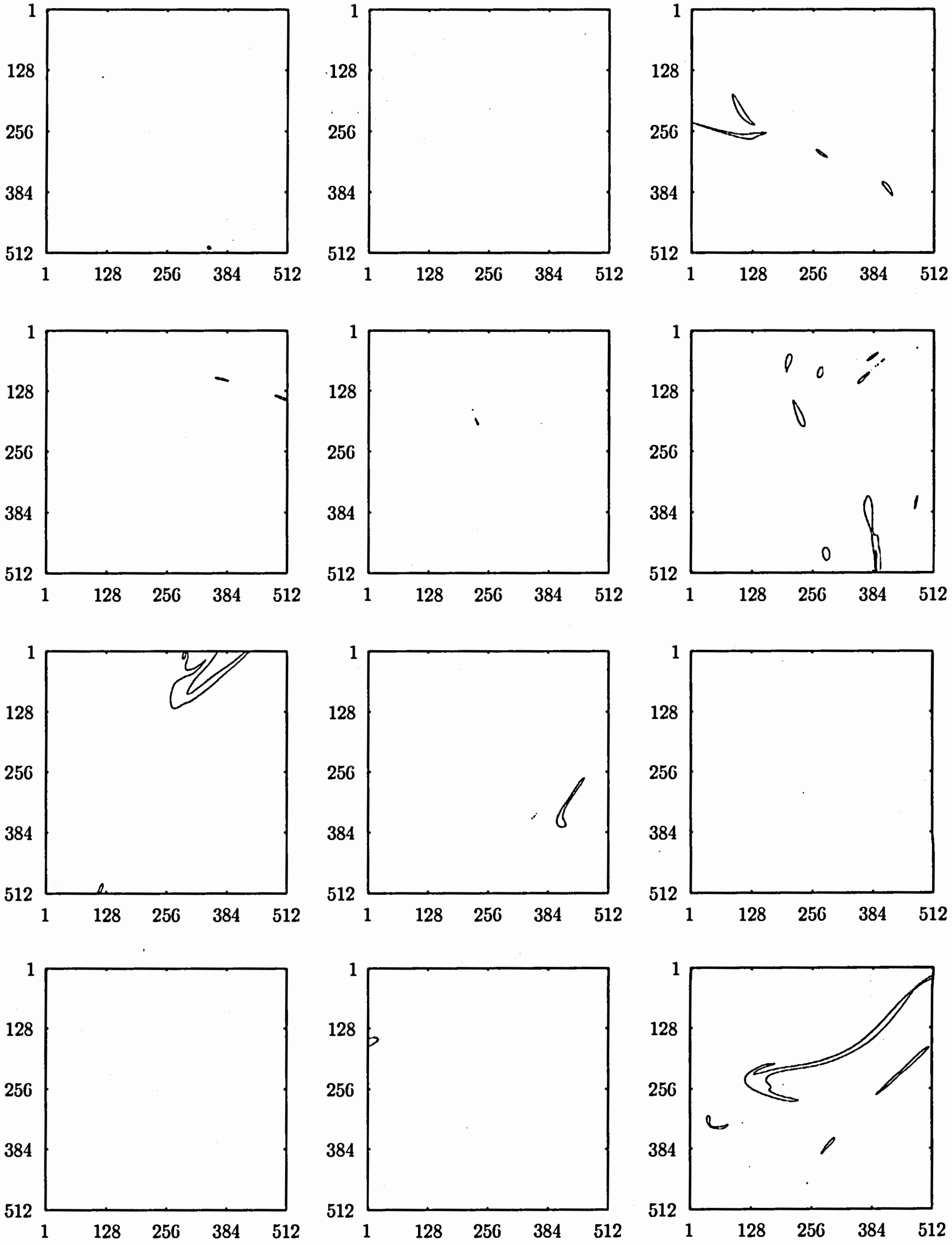

Figure 4.9: 12 consecutive samples from the set of 6000 boundary-outline images at x = 1000 mm from the source for a concentration threshold of $C^*_{th,3} = \langle C^* \rangle + 3 \cdot \mathrm{sdev}(C^*)$. The streamwise direction within the images is from left to right. The images were captured from left to right, and from top to bottom of the page.

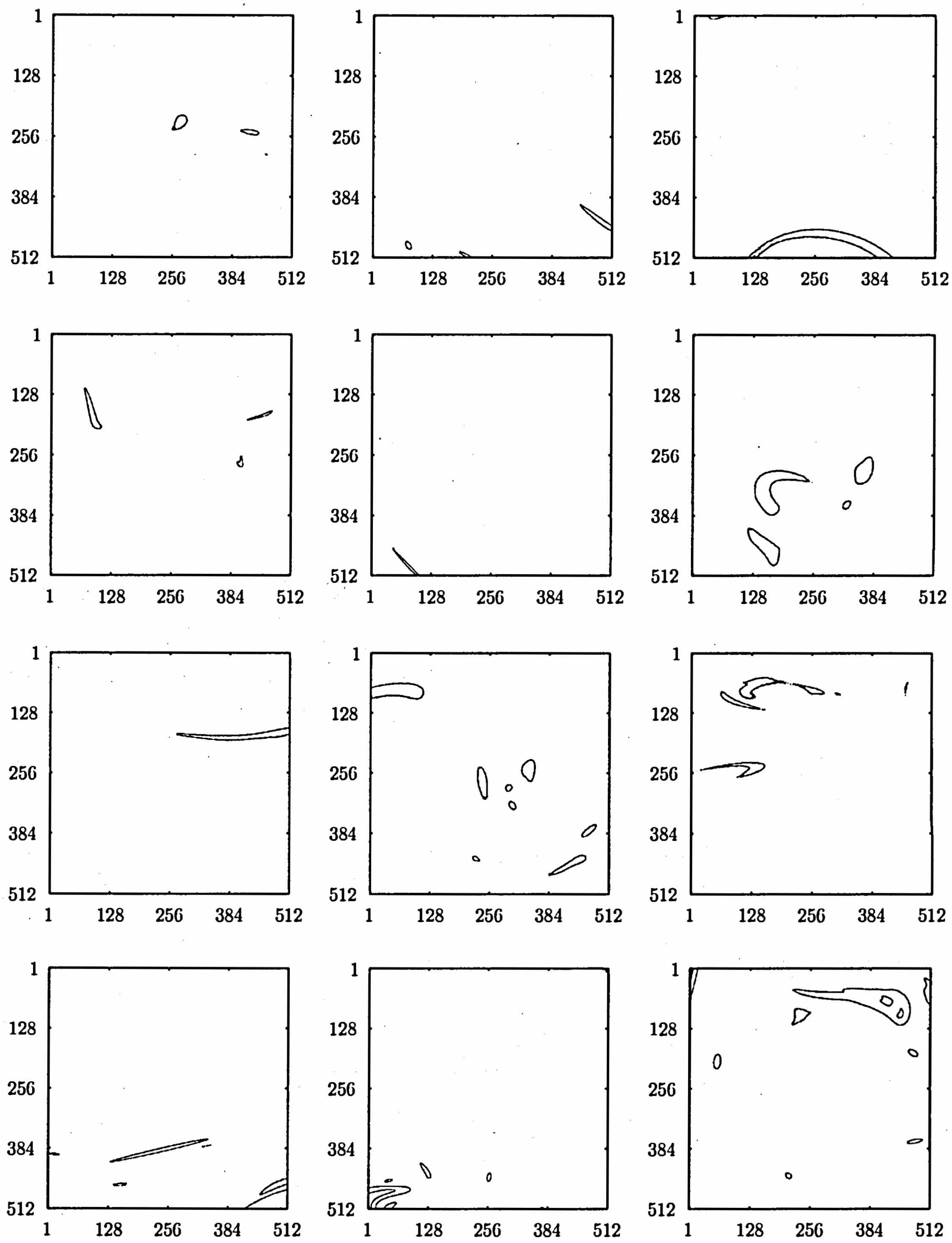

Figure 4.10: 12 consecutive samples from the set of 6000 boundary-outline images at $x = 2000$ mm from the source for a concentration threshold of $C^*_{th,3} = \langle C^* \rangle + 3 \cdot \mathrm{sdev}(C^*)$. The streamwise direction within the images is from left to right. The images were captured from left to right, and from top to bottom of the page.

not possible to extract fractal measures below the threshold $C^*_{th,3}$. For the two cases closer to the source, where the signal to noise ratio is better, the plots additionally contain fractal measures at $C^*_{th,1}$.

The coverage count, $\langle N_2 \rangle$, originates directly from the box-counting algorithm, and thus represents the basis for all other fractal measures (shown in Fig. 4.11). It represents the number of boxes of size λ in the image field that contain part of the iso-surface structure. The coverage count decreases with increasing concentration threshold, indicating that less iso-surface structure is found at larger thresholds. This is consistent with the results of Miller and Dimotakis (1991) for a jet, who emphasized the distinct threshold dependence of fractal measures. At the largest considered scale (i.e. at size of the bounding box), the coverage count is smaller than unity because some of the images do not contain any iso-surface structure. This detail differs from the results of e.g. Catrakis and Dimotakis (1996), where all images contained iso-surface structure. In contrast to the qualitative changes of the iso-surfaces in the images described in the previous section, changes in $\langle N_2 \rangle$ with increasing distance from the source are hardly observable. In addition, most of the curves look approximately linear in a log-log plot, which leads to an expectation of an approximately constant fractal dimension. In fact, it will be necessary to consider more sensitive measures.

The coverage fraction, $\langle F_2 \rangle$ (shown in Fig. 4.12), is closely related to the coverage count and is a measure of the fraction of the image field that is covered by iso-surfaces. As for the coverage count, the coverage fraction drops for higher concentration thresholds, which is consistent with an increasing sparseness of the iso-surface distribution. At the largest scales captured by the image field (i.e. at $\lambda/\delta_b = 1$), the plots indicate that roughly between 40 and 80 percent of the images contain iso-surfaces, depending on the concentration threshold and the distance from the source. When viewed at the smallest scales, however, the iso-surfaces (i.e. the boundaries of the dye filaments, not the filaments as a whole) cover only between a hundredth and a thousandth of the image area. Therefore, if one is interested in the details of the concentration field at a distinct concentration threshold (e.g. to track the concentration limit of a

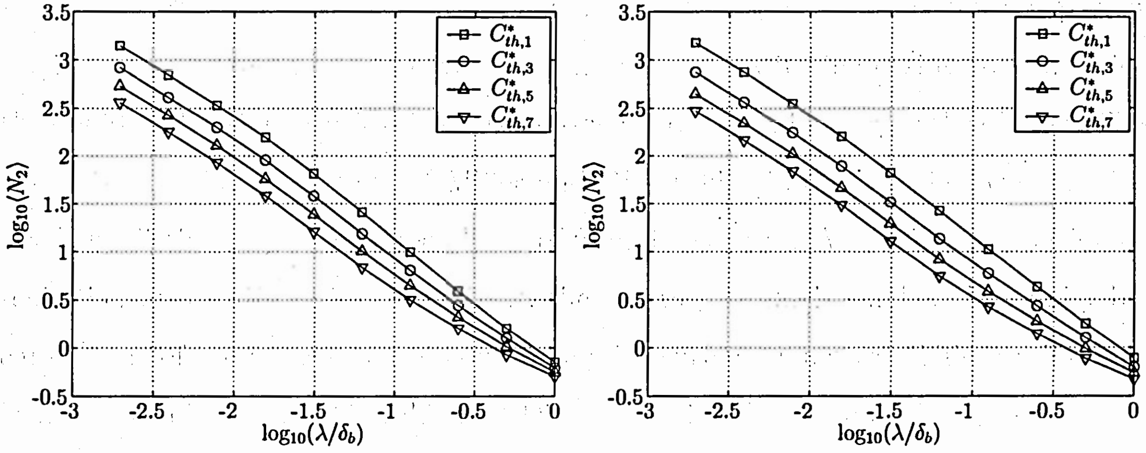

(a) $x = 250$ mm

(b) $x = 500$ mm

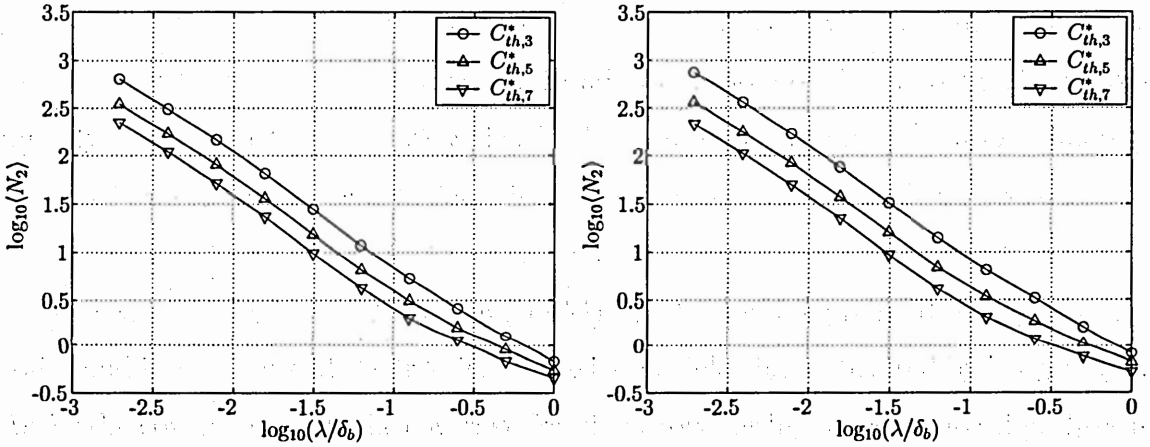

(c) $x = 1000$ mm

(d) $x = 2000$ mm

Figure 4.11: Coverage count, $\langle N_2\rangle$, as a function of normalized scale, λ/δ_b, for several concentration thresholds, $C^*_{th,m} = \langle C^*\rangle + m \cdot \mathrm{sdev}(C^*)$, at four distances, x, from the source.

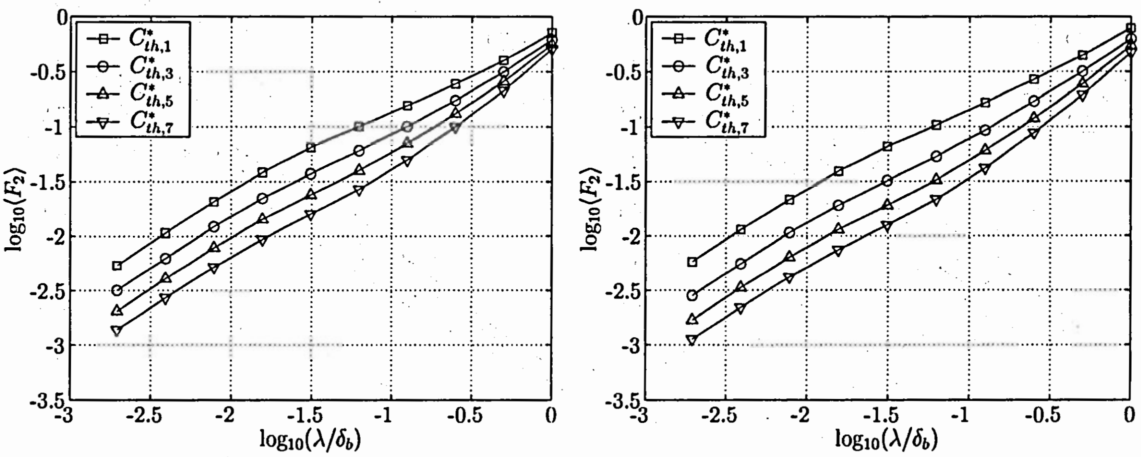

(a) $x = 250$ mm (b) $x = 500$ mm

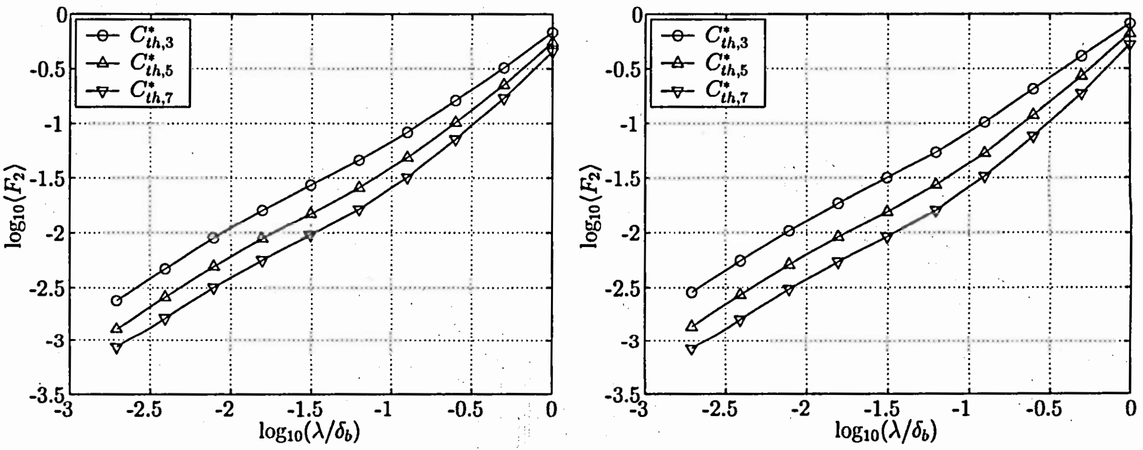

(c) $x = 1000$ mm (d) $x = 2000$ mm

Figure 4.12: Coverage fraction, $\langle F_2 \rangle$, as a function of normalized scale, λ/δ_b, for several concentration thresholds, $C^*_{th,m} = \langle C^* \rangle + m \cdot \text{sdev}(C^*)$, at four distances, x, from the source.

pollutant or the flame surface in stoichiometric combustion), one is confined to a very narrow and tiny fraction of the overall concentration field. With increasing distance from the source, the influence of the concentration threshold on the coverage fraction seems to grow. However, the trend is not distinct, so we will look for more meaningful measures to quantify the influence of the downstream distance.

We have already seen that the fractal measures, and thus the geometry of the iso-surfaces, appear different depending on resolution. The measure that describes this quality, among other things, is the fractal (or coverage) dimension, $\langle D_2 \rangle$, as shown in Fig. 4.13. At the smallest scales, the coverage dimension tends to unity, indicating smooth iso-surfaces with a lack of finer convolution, and thereby identifying the Batchelor scale. With increasing scale, the coverage dimension starts to grow. Thus, the coverage dimension is found to be scale-dependent (i.e. Level 3 complex), in agreement with the results of Catrakis and Dimotakis (1996) for a jet. Therefore, the current data are not in agreement with simple power-law length scaling (Level 2 complexity) as reported by Sreenivasan and Meneveau (1986)), for example. Most interestingly, a distinct range of scales exists where the coverage dimension is independent of the concentration threshold, over the wide range of concentration thresholds considered in this study. This unique scale range is identified as the viscous-convective range of the turbulent concentration field (i.e. $\eta_B \ll \lambda \ll \eta$, cf. Sec. 2.1.5), and is marked within the plots. (Note that the Batchelor and Kolmogorov scales are only scale estimates, and that the discrete points of the coverage dimension are based on values of the coverage count at larger and smaller scales, due to finite differencing). This behavior is also observed when redrawing the plots to examine the changes in the coverage dimension with respect to distance from the source (Fig. 4.14). The coverage dimension in the viscous-convective range is not only independent of the concentration threshold, but also independent of the distance from the source. With respect to these two parameters, the coverage dimension in the viscous-convective range can be described as *universal*.

It could be argued, however, that the universality may be an artifact of the particular normalization of the fluctuating concentration field. This issue leads us back

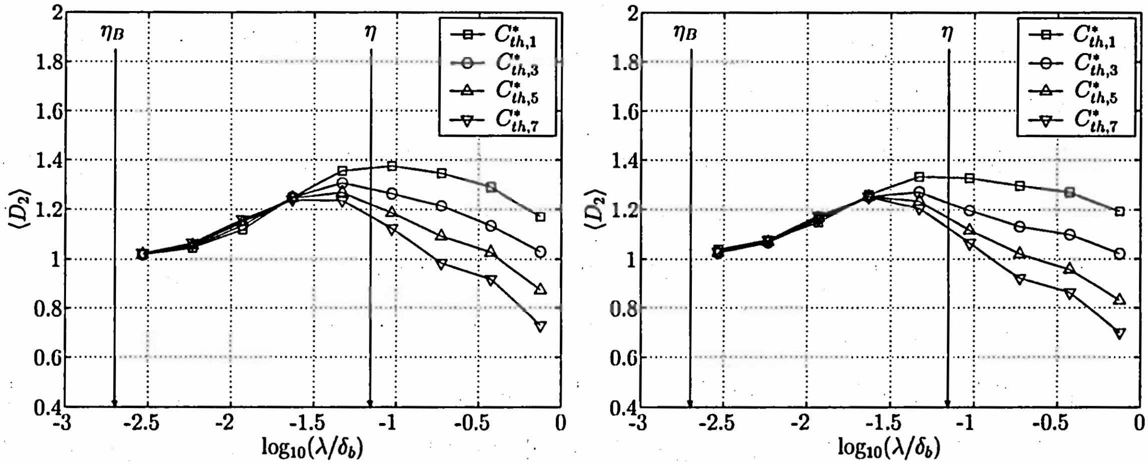

(a) $x = 250$ mm

(b) $x = 500$ mm

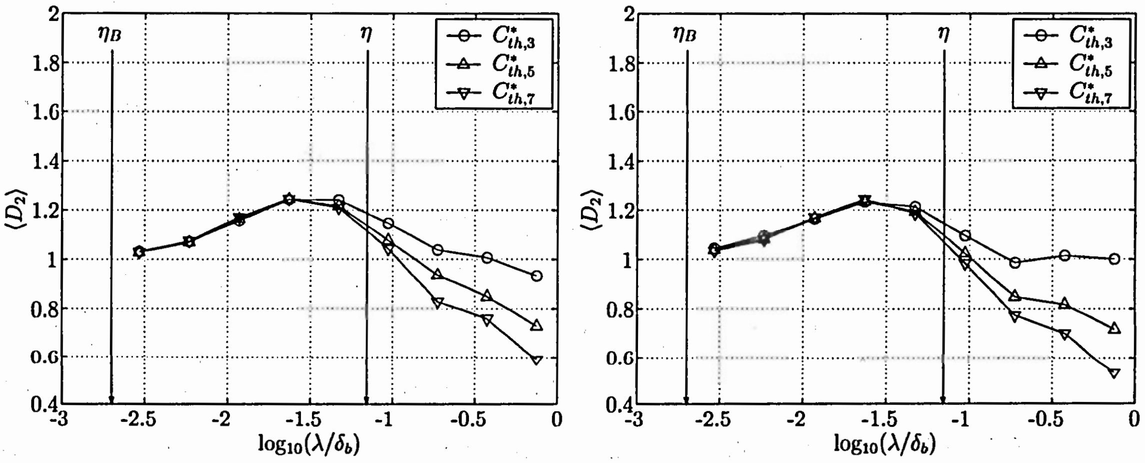

(c) $x = 1000$ mm

(d) $x = 2000$ mm

Figure 4.13: Coverage dimension, $\langle D_2 \rangle$, as a function of normalized scale, λ/δ_b, for several concentration thresholds, $C^*_{th,m} = \langle C^* \rangle + m \cdot \mathrm{sdev}(C^*)$, at four distances, x, from the source. In the viscous-convective range (i.e. $-2.7 \approx \eta_B/\delta_b \ll \lambda/\delta_b \ll \eta/\delta_b \approx -1.2$), the coverage dimension is independent of C^*_{th}.

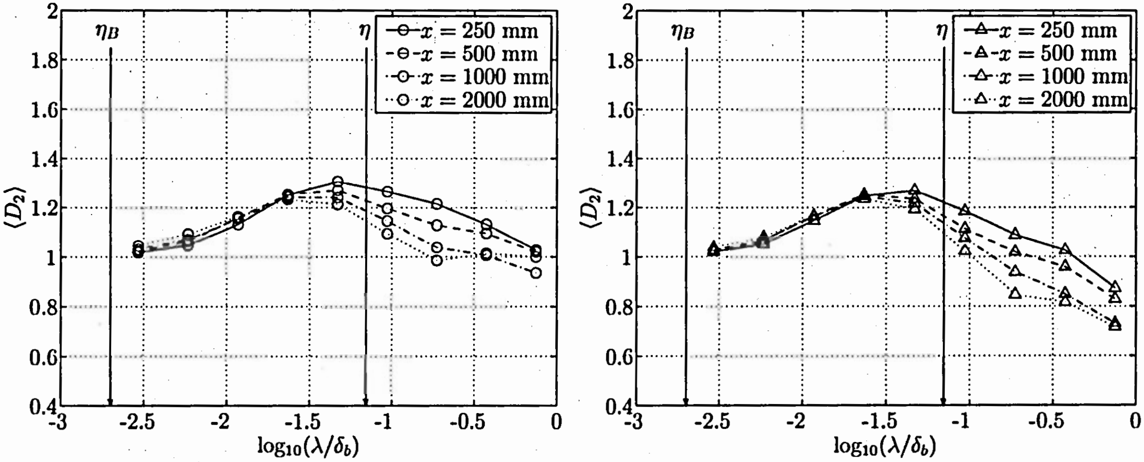

(a) $C^*_{th,3} = \langle C^* \rangle + 3 \cdot \mathrm{sdev}(C^*)$

(b) $C^*_{th,5} = \langle C^* \rangle + 5 \cdot \mathrm{sdev}(C^*)$

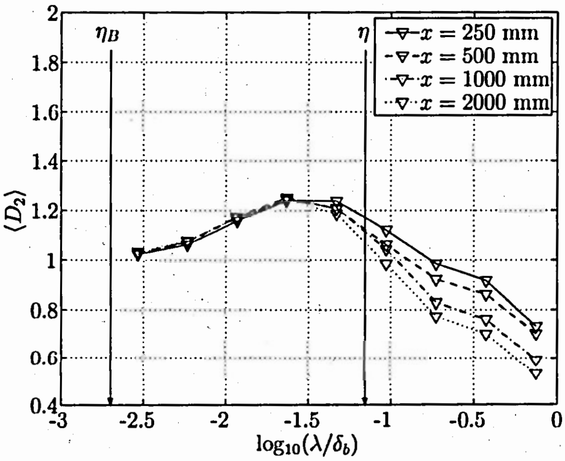

(c) $C^*_{th,7} = \langle C^* \rangle + 7 \cdot \mathrm{sdev}(C^*)$

Figure 4.14: Coverage dimension, $\langle D_2(\lambda/\delta_b) \rangle$, for four distances, x, from the source and three different concentration thresholds, $C^*_{th,m} = \langle C^* \rangle + m \cdot \mathrm{sdev}(C^*)$. In the viscous-convective range (i.e. $-2.7 \approx \eta_B/\delta_b \ll \lambda/\delta_b \ll \eta/\delta_b \approx -1.2$), the coverage dimension is independent of x.

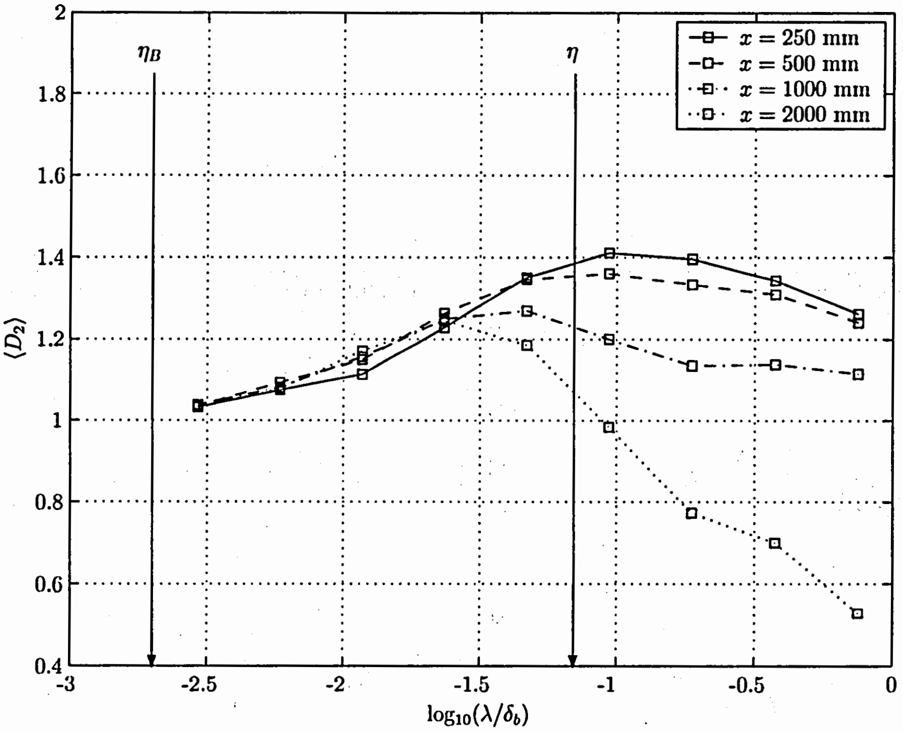

Figure 4.15: Coverage dimension, $\langle D_2(\lambda/\delta_b)\rangle$, over a range of distances, x, from the source, for an absolute concentration threshold of $C^*_{th} = 0.0234$ for the instantaneous concentration field. As before, the coverage dimension in the viscous-convective range (i.e. $-2.7 \approx \eta_B/\delta_b \ll \lambda/\delta_b \ll \eta/\delta_b \approx -1.2$) is approximately independent of x.

to the general question of how to compare concentration iso-surfaces at different downstream locations in the plume. The basic problems associated with an absolute concentration threshold in connection with the rapid decay of the mean and fluctuating field with x have already been discussed (Sec. 4.1). Nevertheless, we attempted to compare the iso-surface geometry also at a constant absolute concentration threshold, namely $C^*_{th} = 0.0235$ (Fig. 4.15). Although the threshold level was chosen carefully to be relevant for each location, for $x = 250$ mm this absolute concentration threshold is outside the previously considered threshold range and is almost as low as the mean concentration (Tab. 4.1). We have argued in Sec. 3.2.4 that iso-surfaces at such low concentration thresholds may be biased by background noise. As expected, the coverage dimension for $x = 250$ mm deviates slightly from the universal behavior. The deviation, however, does not look like the typical result of background noise, and thus cannot be clearly assigned to either noise or the fact that the threshold is below the previously considered range. In any case, for the remaining distances from the source, the universality holds for an absolute concentration threshold. Therefore, we are confident that over a wide range of concentration thresholds and distances from the source, the described universality of the coverage dimension in the viscous-convective range is a real and rather robust characteristic of the concentration field.

Let us now consider scales greater than the viscous-convective range, i.e. for $\lambda > \eta$. In Fig. 4.13, the coverage dimension exhibits distinct threshold dependence up to the largest scales of the image field. The coverage dimension is attenuated with increasing concentration threshold, and clearly tends to zero. Hence, with higher concentration thresholds, the iso-surfaces get smaller and smaller, and their presence within the field becomes rarer. This represents a significant difference compared to the results of e.g. Catrakis and Dimotakis (1996) for a jet, where the topological dimension and thus the coverage dimension were always equal to and above unity, respectively. In addition, the differences in the coverage dimension for adjacent concentration thresholds increases with distance. This implies that during the downstream advection, the dye filaments change from "steep peaks" to "flat hills", as they get eroded by turbulent stirring and molecular diffusion. In Fig. 4.14, we observe a moderate but clear decrease in the coverage dimension with increasing distance from the source. As already argued from the sample iso-surface images in Sec. 4.2.1, the iso-surfaces evolve with x such that few large and complex objects break down into many smaller and less convoluted ones. Recall that the coverage dimension is a measure for both the convolution and dispersion of the iso-surfaces. Hence, it may be concluded that the decrease in convolution outweighs the increase in dispersion. Both the decrease in dimension (and thus in complexity) and the shift from convoluted to dispersed objects are evidence for the progressing homogenization of the concentration field. This is consistent with the results of Catrakis and Dimotakis (1996), who found enhanced homogenization of the concentration field (in their case due to higher Reynolds numbers) corresponds to a decrease in the fractal dimension. For the absolute concentration threshold in Fig. 4.15, the x dependence of the coverage dimension is stronger than for the normalized concentration thresholds, i.e. the coverage dimension drops faster with increasing distance from the source. This is explained by the rapid decay of the instantaneous concentration field. While the selected threshold is of the order of the mean concentration at $x = 250$ mm, and thus identifies vast iso-surface structure, the same threshold is seven standard deviations above the mean concentration for $x = 2000$ mm. Thus, it captures only the highest concentration peaks, which we have already identified to be smooth and extremely sparse. At low concentration thresholds, at which the iso-surfaces exhibit small-scale noise, the coverage dimension rises with distance. This was confirmed by examining several low concentration, large distance iso-surface images.

The big picture for the fate of concentration iso-surfaces in a turbulent boundary layer can therefore be drawn as follows: Few, sparse dye filaments of high concentration and with steep gradients at their boundaries are first significantly distorted by the turbulent motions (corresponding to a medium coverage dimension, dominated by convolution, and only moderately dependent on the threshold). As they evolve downstream, the peaks become less steep and the dye filaments start to break up into several dispersed, smoother objects. At lower thresholds, they therefore cover a larger fraction of the field, tend to homogenize it and increase the coverage dimension due to dispersion. At high thresholds, however, ever fever, very small and smooth peak iso-surfaces remain, which further homogenizes the field and yields a rapid decrease in the coverage dimension.

The fractal measure that may be most important in practical applications is the coverage length, $\langle L_2 \rangle$. In our 2-D concentration fields, the coverage length measures the length (in pixels) of iso-surfaces within the image field, as observed at a particular scale. The coverage length is the lower-dimensional equivalent of the iso-surface area in the more general 3-D case. Thus, it is a direct measure for the surface-area generation of turbulence, which can be considered as the key feature of mixing efficiency. As can be observed in Fig. 4.16, the coverage length decreases continuously with increasing concentration threshold. The reason for this trend is a combination of less convolution and increased sparseness of the iso-surfaces at higher thresholds. In contrast, the coverage length of iso-surfaces in the jet data exhibits a maximum

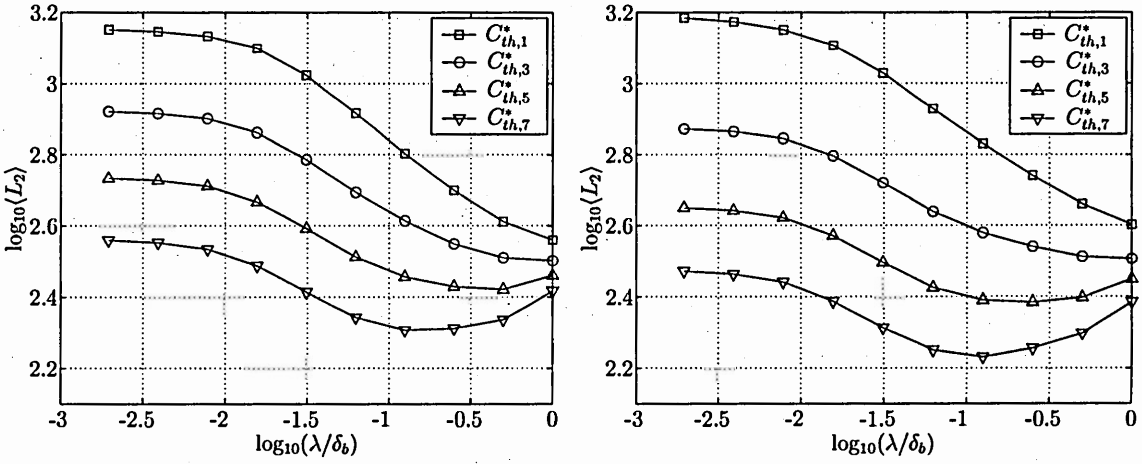

(a) $x = 250$ mm

(b) $x = 500$ mm

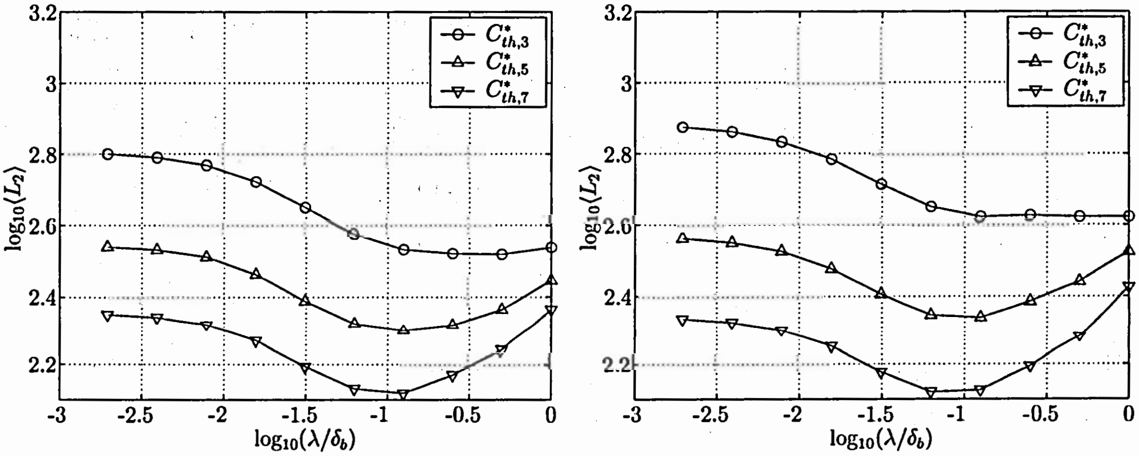

(c) $x = 1000$ mm

(d) $x = 2000$ mm

Figure 4.16: Coverage length, $\langle L_2 \rangle$, as a function of normalized scale, λ/δ_b, for several concentration thresholds, $C^*_{th,m} = \langle C^* \rangle + m \cdot \mathrm{sdev}(C^*)$, at four distances, x, from the source.

at intermediate concentration thresholds (Catrakis and Dimotakis, 1996). As already explained in detail for the coverage dimension, the coverage length increases with x for low concentration thresholds, while it decreases for high thresholds. The coverage length is a scale-cumulative measure (i.e. the length at a particular scale depends on the iso-surface geometry at all scales above that scale, cf. Eq. 2.37). In particular, the coverage length can obviously decrease with decreasing scale, if the coverage dimension is smaller than unity.

As the iso-surfaces must be smooth lines at scales smaller than the Batchelor scale, the coverage length systematically approaches a constant value, the total coverage length, $\langle L_{2,tot} \rangle$, as the scale approaches η_B. For our data, the total coverage length ranges between 250 and 1500 pixels, which corresponds to a length of 4 to 30 mm within the 10×10 mm image field. If the flow was laminar the dye would follow a smooth, straight, and narrow path along the source centerline, which would yield a iso-surface coverage length of approximately $2 \cdot \delta_b = 1024$ pixels (corresponding to approximately 20 mm), independent of a concentration threshold. Thus, *per image field*, the turbulent plume creates iso-surfaces that are at the maximum only about 1.5 times longer than the laminar iso-surface, and even shorter for higher concentration thresholds. The essential advantage of the turbulent plume, as far as surface length (or area in 3-D) generation and mixing efficiency are concerned, is therefore its tendency to rapidly spread in the cross-stream (i.e. vertical and transverse) directions, while the laminar plume remains confined to the very close surroundings of the centerline. Hence, the coverage length has to be related to the cross-stream extent of the plume to assess its effective coverage length. It is very difficult to determine the cross-stream extent of the plume up to which iso-surfaces appear. In particular, this extent is not equivalent to the extent of the mean concentration field. Moreover, in the present study we only have collected iso-surface data along the centerline. Towards the boundaries of the plume, the iso-surface structure can be expected to become more sparse, and thus the total coverage length per image field is likely to be smaller than at the centerline. Nevertheless, a very coarse estimate is possible if we assume the same scaling of the iso-surfaces as presented for the theoretical mean concentration field in

Sec. 2.1.7, i.e. a spread of the vertical and transverse extent in proportion to $x^{-1/2}$. The 2-D extent of the plume in the vertical image plane would then roughly grow as $x^{-1/2}$. The total coverage length for $C^*_{th,3}$ can be observed to be approximately independent of the distance from the source. The effective absolute coverage length of the plume at $x = 2000$ mm would then be almost three times longer than at $x = 250$ mm, and the iso-surface area of the real 3-D plume would be about eight times larger, yielding a molecular diffusion flux that is also enhanced by a factor of eight.

At small scales, the curves of the coverage length for different concentration thresholds look very similar and seem to be only shifted. Thus it may be valuable to normalize them. For that purpose, we introduce the measure

$$\langle L_{2,u}(\lambda/\delta_b)\rangle \equiv \frac{\langle L_{2,tot}\rangle}{\langle L_2(\lambda/\delta_b)\rangle}, \tag{4.3}$$

which we call the "coverage length underestimate" because it can be interpreted as the underestimate of the total coverage length of an iso-surface when the iso-surface is viewed at a scale larger than the Batchelor scale. For example, if the coverage length at a scale λ is half of the total coverage length, the coverage length underestimate at that scale is two. The discretization is analogous to $\langle L_2\rangle$ in Eq. 3.8. This measure, applied to our data sets, is shown in Fig. 4.17. Most interestingly, this measure is *universal* in the viscous-convective range, in analogy to the fractal dimension. For scales larger than the Kolmogorov scale, the underestimate decreases with increasing concentration threshold and with increasing distance from the source. In both cases, the reason is that the total coverage length is not very large anyway.

Next, let us consider the LEB-scale PDF, $\langle f_2\rangle$, which gives the distribution of LEB-scales in the iso-surface data (Fig. 4.18). The LEB-scale of a point randomly placed in the bounding box is the size of the largest square that contains the point but no part of the iso-surface structure. At large scales the LEB-scale PDF is virtually independent of the concentration threshold, while towards smaller scales it decreases more and more with increasing concentration threshold. Generally, a high LEB-scale PDF at small scales means a high probability of finding iso-surface structure in the proximity of randomly positioned points in the bounding box. More iso-surface structure per

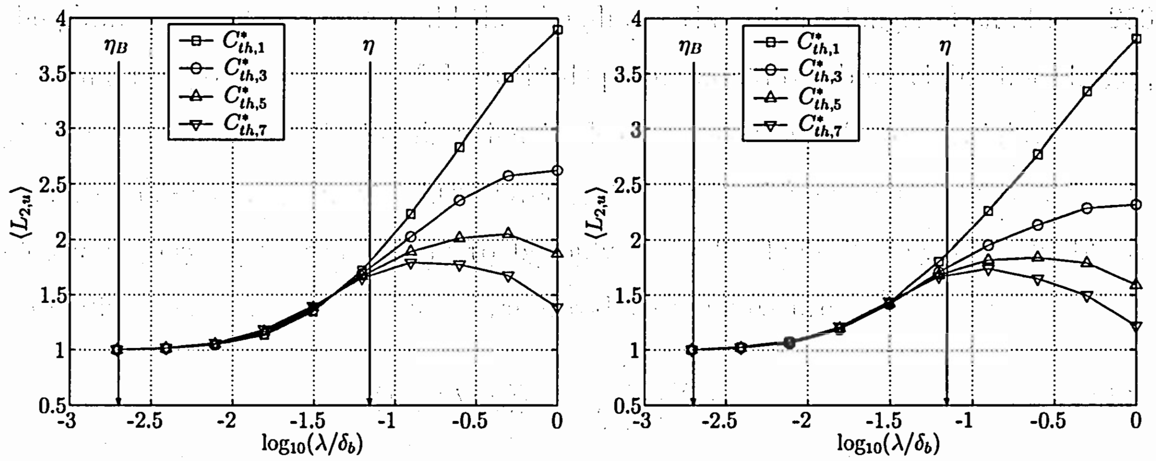

(a) $x = 250$ mm

(b) $x = 500$ mm

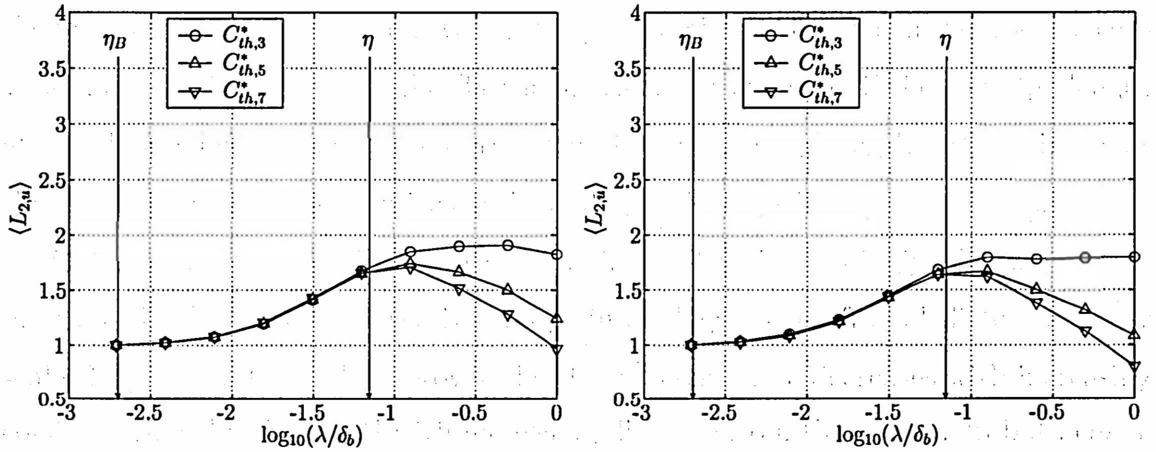

(c) $x = 1000$ mm

(d) $x = 2000$ mm

Figure 4.17: Underestimate, $\langle L_{2,u} \rangle = \langle L_{2,tot} \rangle / \langle L_2 \rangle$ of the total coverage length, as a function of normalized scale, λ/δ_b, for several concentration thresholds, $C^*_{th,m} = \langle C^* \rangle + m \cdot \text{sdev}(C^*)$, at four distances, x, from the source. The measure gives the factor by which the total coverage length is larger than the apparent coverage length at scale $\lambda > \eta_B$. In the visocus-convective range, this measure is independent of C^*_{th} and x.

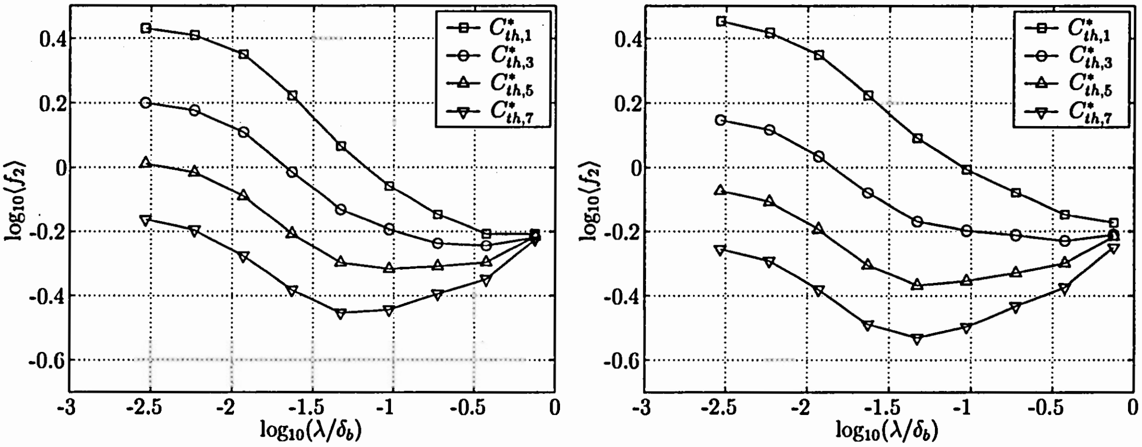

(a) $x = 250$ mm

(b) $x = 500$ mm

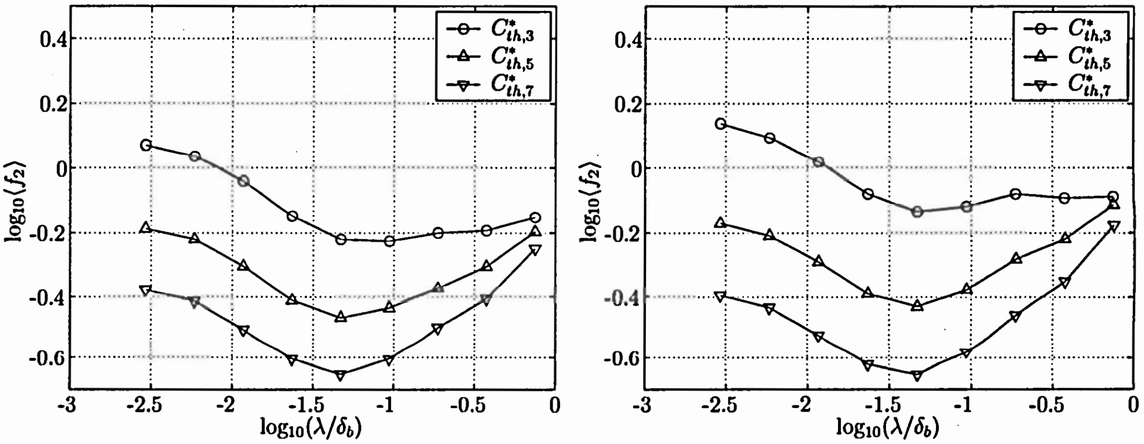

(c) $x = 1000$ mm

(d) $x = 2000$ mm

Figure 4.18: LEB-scale PDF, $\langle f_2(\lambda/\delta_b)\rangle$, as a function of normalized scale, λ/δ_b, for several concentration thresholds, $C^*_{th,m} = \langle C^*\rangle + m \cdot \text{sdev}(C^*)$, at four distances, x, from the source.

image field increases the LEB-scale PDF at smaller scales, and a sparse iso-surface field decreases it. In addition, at small concentration thresholds, the LEB-scale PDF increases with increasing distance from the source, while for higher thresholds, the inverse trend can be observed. Again, this is consistent with our conclusions from the results of other fractal measures, i.e. that the iso-surface structure becomes more dense at lower thresholds and more sparse at higher thresholds, when moving away from the source. The LEB-scale PDF might be of interest in the artificial creation of iso-surfaces for modeling.

The scale-cumulative length-area ratio, $\langle \Omega_2 \rangle$ (Fig. 4.19), and its length-area exponent, $\langle \alpha_\Omega \rangle$ (Fig. 4.20), do not contain new information because they are directly connected to the coverage length (by a constant factor) and to the coverage dimension (by a constant summand), respectively (cf. Sec. 2.2.7). They are presented here for completeness.

Finally, the scale-local length-area density, $\langle g_2 \rangle$, and its exponent $\langle \alpha_g \rangle$, are shown in Figs. 4.21, and 4.22, respectively. Many of the plotted curves are not continuous because of the logarithmic derivative in the definition of the length-area density. Because $\langle \Omega_2 \rangle$ has regions of negative slope, the logarithmic finite difference is not defined and therefore gaps form in the plots. The length-area density measures the scale-local contribution of the iso-surface structure to the scale-dependent length-area ratio, or equivalently the contribution to the coverage length. The scale-local contributions decrease with increasing concentration threshold, consistent with a lower scale-cumulative coverage length and with a sparse iso-surface field. Generally, smaller scales provide higher local contributions to the coverage length, with the maximum shifting towards the smallest scales for increasing distance from the source. As explained in Sec. 2.2.7, Catrakis et al. (2002) have shown that the fractal dimension itself is a scale-cumulative measure, and therefore is influenced by the scale-local length-area density of all scales larger than the considered scale.

In contrast, $\langle \alpha_g \rangle$ can be viewed as a scale-local dimension, able to detect scale-local power-law scaling (expressed by a constant scale-local dimension). Fig. 4.22 is not very helpful in this respect, however. The only interesting feature is the hint of

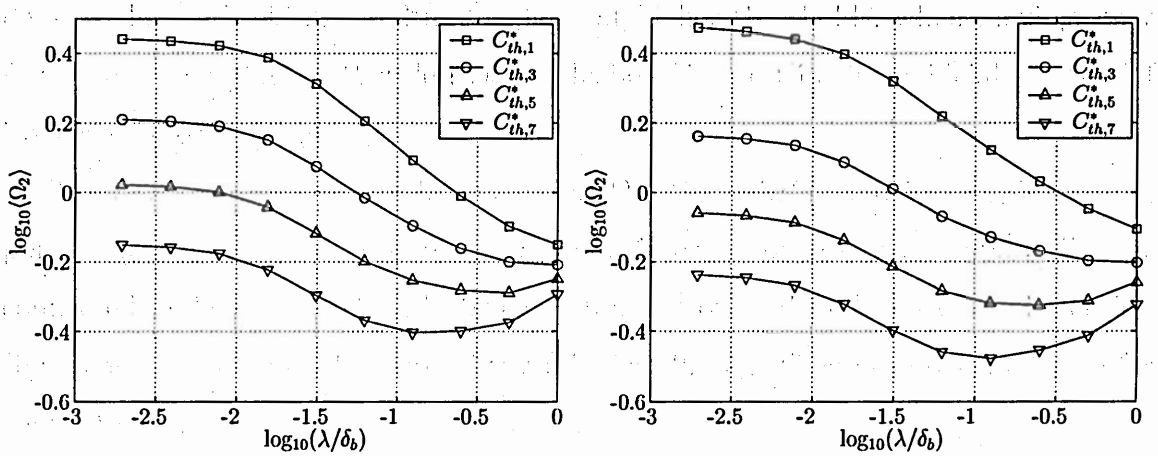

(a) $x = 250$ mm

(b) $x = 500$ mm

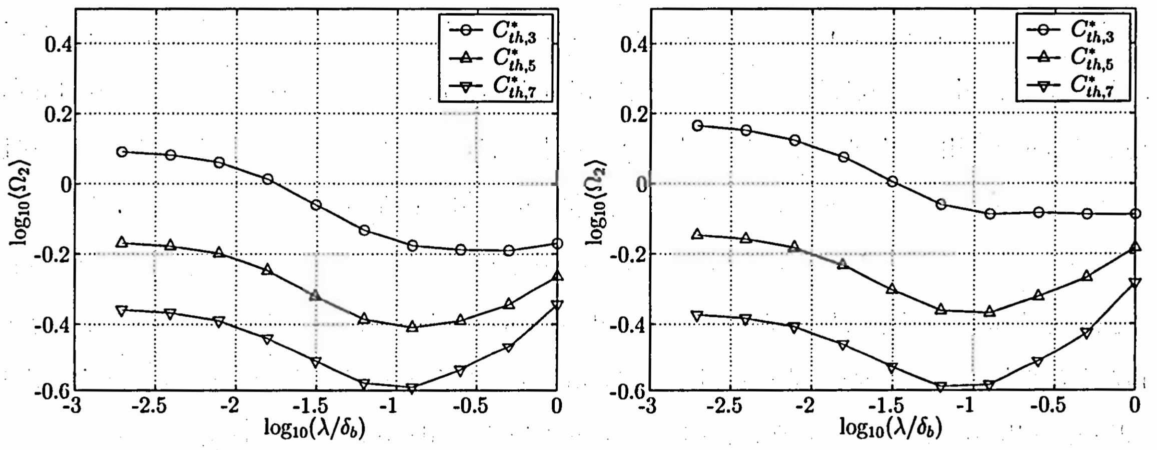

(c) $x = 1000$ mm

(d) $x = 2000$ mm

Figure 4.19: Scale-cumulative length-area ratio, $\langle \Omega_2(\lambda/\delta_b) \rangle$, as a function of normalized scale, λ/δ_b, for several concentration thresholds, $C^*_{th,m} = \langle C^* \rangle + m \cdot \mathrm{sdev}(C^*)$, at four distances, x, from the source.

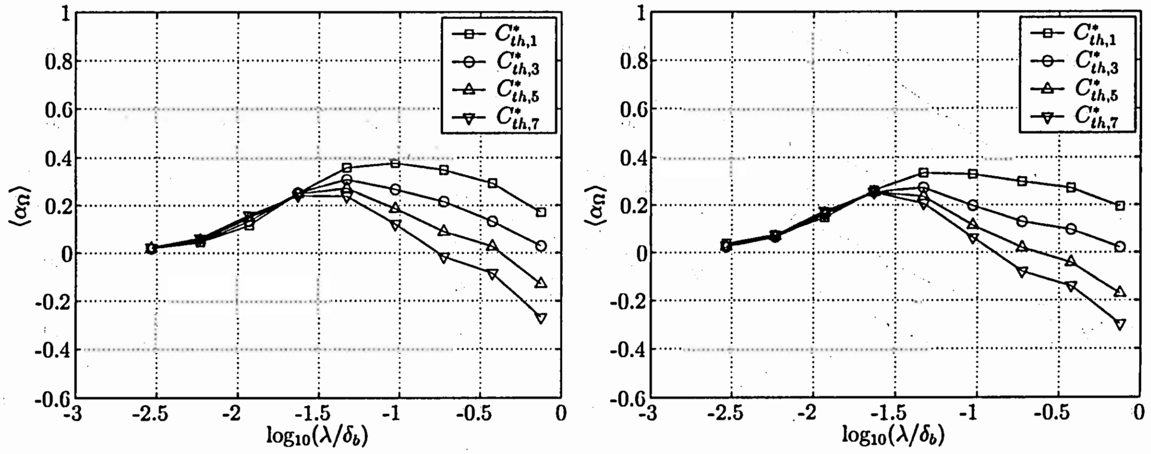

(a) $x = 250$ mm

(b) $x = 500$ mm

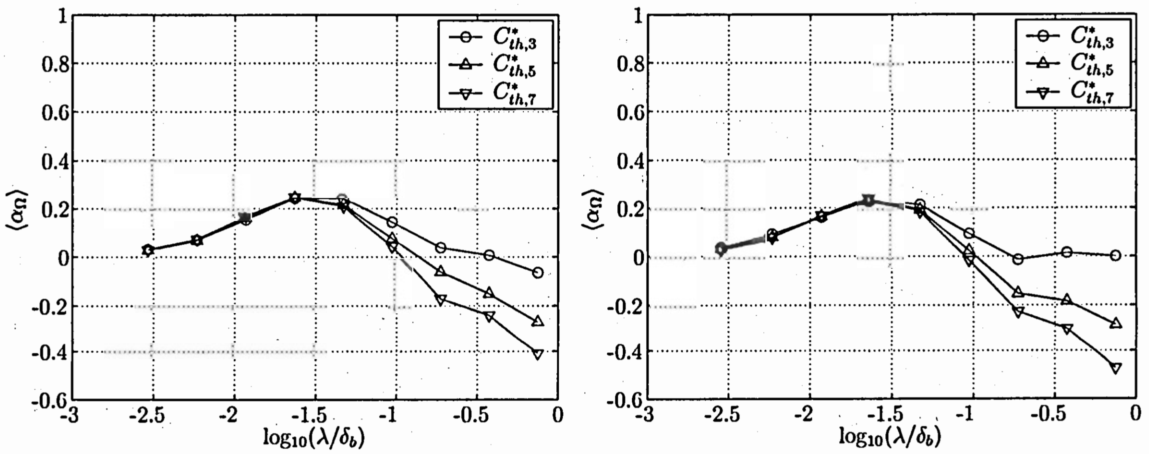

(c) $x = 1000$ mm

(d) $x = 2000$ mm

Figure 4.20: Scale-cumulative length-area ratio exponent, $\langle\alpha_\Omega(\lambda/\delta_b)\rangle$, as a function of normalized scale, λ/δ_b, for several concentration thresholds, $C^*_{th,m} = \langle C^*\rangle + m \cdot \mathrm{sdev}(C^*)$, at four distances, x, from the source.

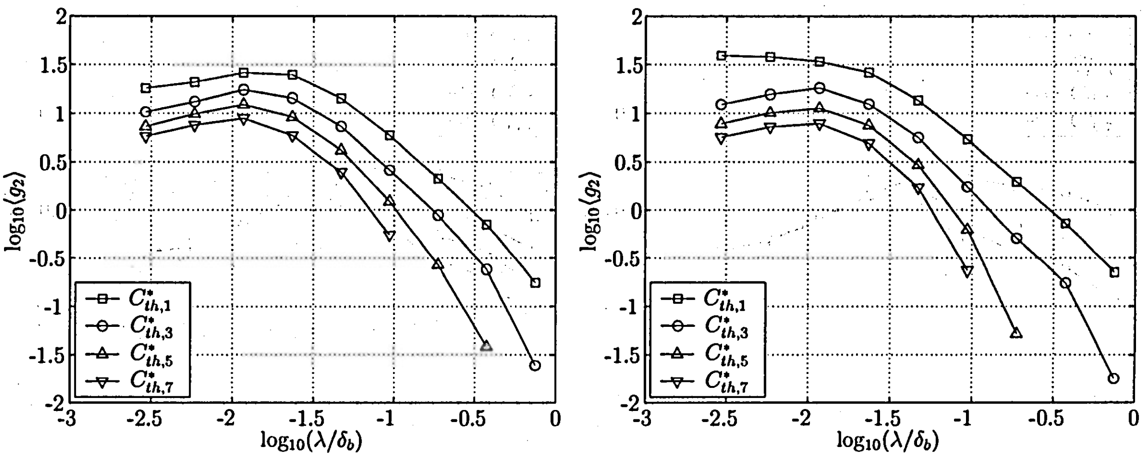

(a) $x = 250$ mm (b) $x = 500$ mm

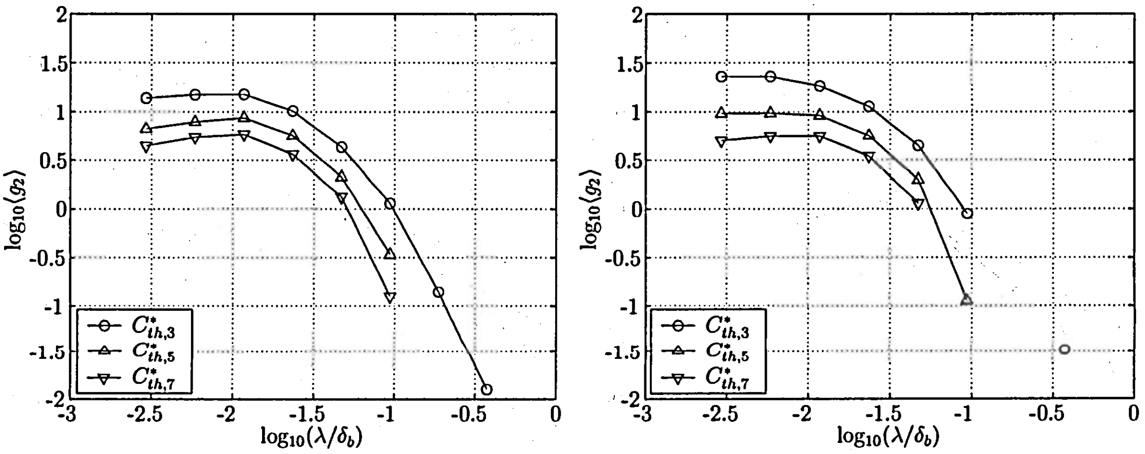

(c) $x = 1000$ mm (d) $x = 2000$ mm

Figure 4.21: Scale-local length-area density, $\langle g_2(\lambda/\delta_b)\rangle$, as a function of normalized scale, λ/δ_b, for several concentration thresholds, $C^*_{th,m} = \langle C^*\rangle + m \cdot \mathrm{sdev}(C^*)$, at four distances, x, from the source.

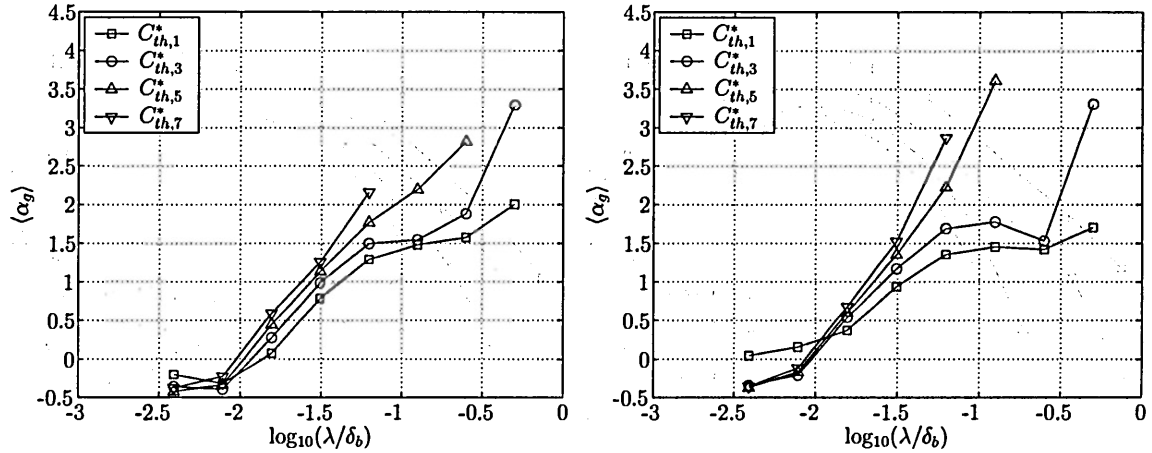

(a) $x = 250$ mm

(b) $x = 500$ mm

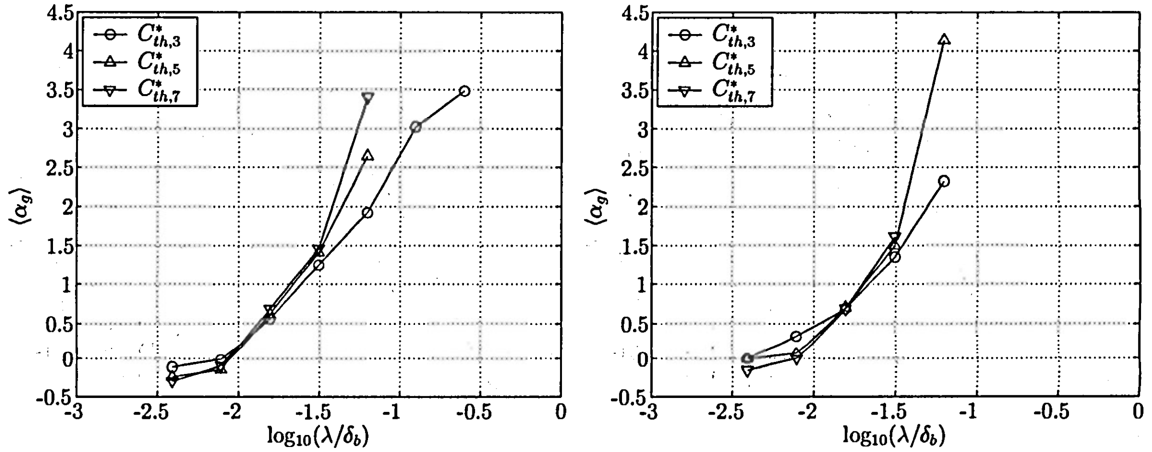

(c) $x = 1000$ mm

(d) $x = 2000$ mm

Figure 4.22: Scale-local length-area density exponent, $\langle\alpha_g(\lambda/\delta_b)\rangle$, as a function of normalized scale, λ/δ_b, for several concentration thresholds, $C^*_{th,m} = \langle C^*\rangle + m \cdot \text{sdev}(C^*)$, at four distances, x, from the source.

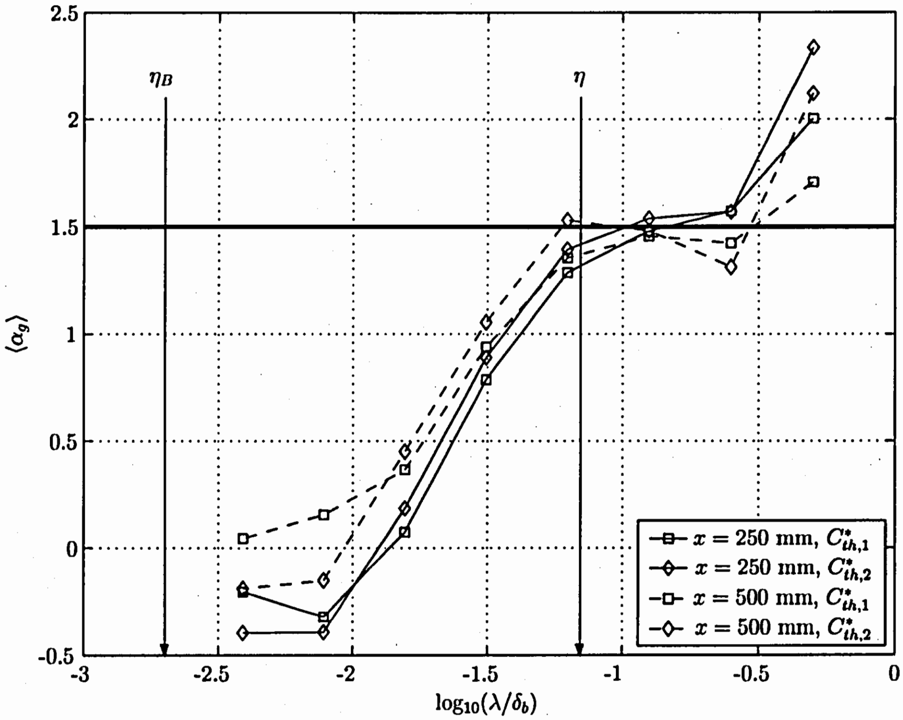

Figure 4.23: Scale-local length-area density exponent, $\langle\alpha_g(\lambda/\delta_b)\rangle$, for two threshold levels, $C^*_{th,1}$ and $C^*_{th,2}$, at the two locations nearest to the source. For scales larger than the Kolmogorov scale (i.e. $\lambda/\delta_b > \eta/\delta_b \approx -1.2$), and for relatively low concentration thresholds, the plateau in the profiles indicates a scale-local power law scaling behavior of the concentration iso-surfaces with a constant scale-local fractal dimension of $D_2 \approx 1.5 = \text{const.}$ (indicated by the horizontal line).

a plateau in the curves for low concentration thresholds for the two locations nearest the source. Even a very narrow plateau can indicate scale similarity, as was shown by Catrakis (2000). Oscillations are typical as we have seen in the evaluation of the theoretical Koch curves in Sec. 3.3.3. Therefore, we combined several $\langle\alpha_g\rangle$ curves into one plot, specifically for the two locations nearest to the source, and for the lowest two thresholds, $C^*_{th,1}$, and $C^*_{th,2}$ (Fig. 4.23). Indeed, a narrow but clear plateau is evident at the lower end of the inertial-convective range of the turbulent concentration field, with a scale-local fractal dimension of $D_2 \approx 1.5 = \text{const.}$. The existence of a constant scale-local dimension is consistent with the results for a jet reported by Catrakis et al. (2002), but the particular value is different. Now that we have identified a potential scale similarity, we can re-examine the coverage dimension and realize that this particular scale range corresponds to the rather flat maximum in the coverage dimension plots (see Fig. 4.13). The fractal dimension is roughly constant in a range of approximately half decade of scales. However, the scale similarity only holds in a narrow range of scales, and for the lowest threshold considered in the present study. Thus, further investigations towards lower thresholds are necessary to evaluate practical significance of this finding.

4.3 Discussion and outlook

In the previous sections, we have presented a comprehensive, qualitative and quantitative description of concentration iso-surfaces in a high Schmidt number (Sc $\approx$ 1000) turbulent passive scalar field produced by an iso-kinetic point source in the inertial layer of a fully developed turbulent boundary layer of an open channel flow. We have identified some similarities but also significant differences to the more frequently examined turbulent jets.

The most important finding of this study is the universal behavior of the iso-surface coverage dimension in the viscous-convective range of the turbulent concentration field. For the turbulent boundary layer and the source location specified in the present study, the iso-surface coverage dimension is therefore known over a wide range of scales, concentration thresholds, and distances from the source. As many additional fractal measures are related to the coverage dimension, it is possible to derive quantitative predictions about their behavior in the viscous-convective range. Most of the fractal measures, however, are scale-cumulative, so that their absolute values also depend on the coverage dimension of the iso-surfaces above the viscous-convective range, which was found to be non-universal. In that case, we are restricted to relative instead of absolute predictions.

In the present study, the coverage dimension is only available in discretized form, with a rather coarse resolution due to the binary subdivision steps of the box-counting algorithm. For practical applications, however, one might be interested in a continuous function, especially if the analytical relations presented in Sec. 2.2.7 are used to

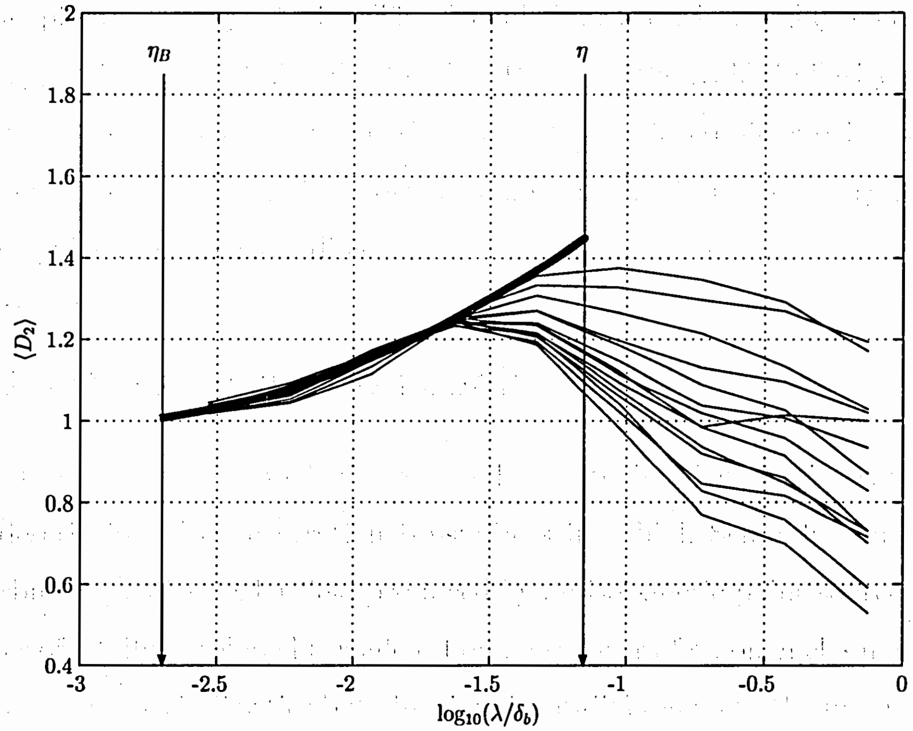

Figure 4.24: Fitting of the coverage dimension in the viscous-convective range, by means of a 2nd order polynomial (thick curve). The thin curves are the measured coverage dimensions profiles for various C^*_{th} and x previously shown in Fig. 4.13.

calculate other fractal measures. For that purpose, we averaged the discretized coverage dimension (in the scale-normalized space λ/δ_b) over all concentration thresholds and distances from the source for example given in Fig. 4.13 and fitted a second order polynomial curve. The result can be seen in Fig. 4.24, where the polynomial is the thick curve and thin curves represent the numerous experimental results. In the scale-normalized viscous-convective range, i.e. for $20/10000 \ll \lambda/\delta_b \ll 700/10000$, the coverage dimension thus can approximated by

$$\langle D_2(\lambda/\delta_b)\rangle \approx 0.12 \cdot \log^2_{10}(\lambda/\delta_b) + 0.75 \cdot \log_{10}(\lambda/\delta_b) + 2.2. \tag{4.4}$$

Obviously, the fitted curve deviates from the measured results near the Kolmogorov scale, but a more exact fit would require a higher-order polynomial, which makes the approach more cumbersome. We also have to keep in mind that the Kolmogorov scale is only a scaling estimate and that the viscous-convective range theoretically starts significantly below the Kolmogorov scale. Over the rest of the viscous-convective range, the polynomial fits the measured results very closely. In particular, the expression for $\langle D_2 \rangle$ approaches unity at the Batchelor scale, as can be expected from theoretical considerations.

Now, let us use the fitted relation to calculate the coverage length underestimate, $\langle L_{2,u} \rangle$. An analytical relation can be derived from Eqs. 2.37 and 4.3. In the general notation valid for arbitrary dimensionality (compare Sec. 2.2.7), we obtain

$$\langle L_{d,u}(\lambda/\delta_b) \rangle = \frac{\langle L_{d,tot} \rangle}{\langle L_d(\lambda/\delta_b) \rangle} = \left(\frac{\eta_B/\delta_b}{\lambda/\delta_b} \right)^{d_t} \cdot \exp \left\{ \int_{\eta_B}^{\lambda} \langle D_d(\tilde{\lambda}/\delta_b) \rangle \frac{\mathrm{d}(\tilde{\lambda}/\delta_b)}{(\tilde{\lambda}/\delta_b)} \right\}. \qquad (4.5)$$

An explicit analytical expression is only possible because the coverage length underestimate, at a particular scale λ, solely depends on the coverage dimension below λ (as opposed to most other fractal measures). For our 2-D case, we can substitute the approximated analytical expression for the coverage dimension, Eq. 4.4, into Eq. 4.5 and solve the integral to get the simper expression

$$\langle L_{2,u} \rangle = \frac{0.0020}{\lambda/\delta_b} \cdot \exp\Big\{ 0.0075 \cdot \ln^3(\lambda/\delta_b) + 0.16 \cdot \ln^2(\lambda/\delta_b) + 2.2 \cdot \ln(\lambda/\delta_b) + 9.0 \Big\}. \qquad (4.6)$$

In Fig. 4.25, the analytical result of Eq. 4.6 (thick curve) is compared with the measured results (numerous thin curves) of all concentration thresholds and distances from the source shown in Fig. 4.17. As can be observed, the coverage length underestimate is weakly sensitive to deviations of the coverage dimension, due to the integral relation. As a result, the analytical solution fits the experimental results very closely, over the entire viscous-convective range. It is redrawn in Fig. 4.26 as a function of absolute length scale, and with higher resolution.

In order to interpret the significance of the presented results, it is necessary to recall the limitations of the present study. First, we only collected measurements at the plume centerline. It is therefore not known whether the universality of the fractal dimension holds off the centerline, i.e. in the vertical and transverse directions. Also, we do not know the cross-sectional extent of the plume, and we do not resolve the largest scales of the iso-surfaces. For a complete description of the mixing process, we need to consider the plume as a whole. Thus, knowledge about cross-sectional

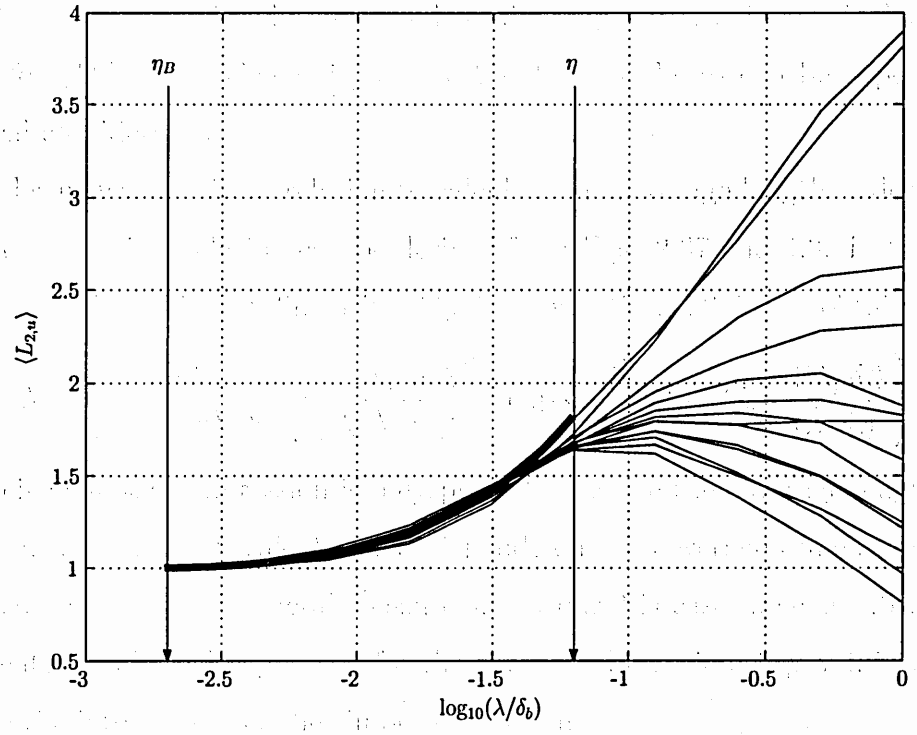

Figure 4.25: Analytical versus measured underestimated coverage length. The thick curve is analytically calculated from the fitted curve, and the thin curves are the measured results for various C^*_{th} and x previously shown in Fig. 4.17.

length-scaling behavior of the concentration iso-surfaces would be crucial. Second, the experiments have been conducted with the source at a fixed vertical location within the turbulent boundary layer, and for a fixed Reynolds number. Thus, we are unable to comment on the sensitivity of the length-scaling behavior to these parameters. Strictly, we can only talk about a universal behavior of the specific plume investigated, not of plumes in turbulent boundary layers in general. Third and most important, our investigation was confined to two dimensions, whereas turbulent mixing processes are inherently three-dimensional. As discussed extensively in Sec. 2.2.6, we underestimate the surface generation of turbulence when measuring in two dimensions. Thus, we need to know how the obtained results can be extrapolated to 3-D concentration fields. For example, do the iso-surfaces have similar small-scale properties in the vertical and in the transverse plane, i.e. are they isotropic? If we assume the cited results of Catrakis and Bond (2000) are applicable to our flow geometry, it could be argued that the coverage dimension that we found in 2-D,

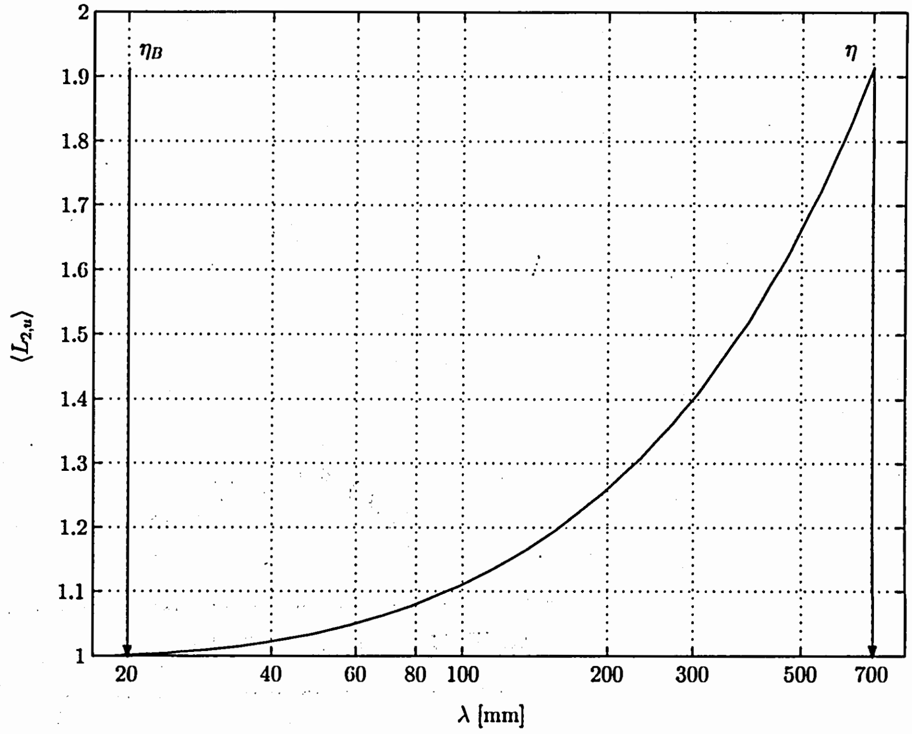

Figure 4.26: Analytical underestimated coverage length as a function of absolute length scale, between the Batchelor Kolmogorov length scales.

increased by one, is a lower limit to the real fractal dimension.

Despite the limitations of the present study, we are confident that the observed small-scale universality of the scaling behavior of concentration iso-surfaces in a turbulent boundary layer is an important discovery, both theoretically and practically. From a theoretical point of view, it would be interesting to identify the physical mechanisms that cause the universality. Universal behavior of scales in spectral space, although it is known today that this is only an approximation, led to a phenomenological spectral-space turbulence theory. Further studies in this area of physical-space scale universality could lay the foundation for a physical-space turbulence theory.

How can such an interesting result be used in practice? Despite promising theoretical progress in the last two decades, the study of fractal geometry of scalar interfaces in fluid turbulence is still characterized by very few practical applications. We would like to suggest a possible application here. The coverage length is related to the iso-surface area in three dimensions. At a particular concentration (threshold), the total interfacial area determines the molecular flux according to Fick's law (Eq. 2.25). Molecular diffusion across high concentration gradients ultimately leads to a dilution of the plume. In the previous section, we introduced a measure, $\langle L_{d,u} \rangle$, for the underestimation of the total interfacial area that occurs when viewing the concentration field at resolutions larger than the Batchelor scale. In this section, we additionally derived an analytical relation for $\langle L_{2,u} \rangle$ in the 2-D case, based on the observed small-scale universality of the fractal dimension. This information could be used to develop a subgrid-scale turbulence model for Large Eddy Simulations (LES). The problem associated with all numerical simulations of turbulent flows (except for Direct Numerical Simulation, DNS), is that the underlying grid does not resolve the smallest scales in the field. Assume that we simulate a continuous point source in a turbulent boundary layer with a grid of resolution λ_{grid}, somewhere between the Kolmogorov scale and the Batchelor scale (i.e. $\eta_B < \lambda_{grid} < \eta$). Hence, the velocity field is fully resolved, but the concentration field is under-resolved. As a consequence, the molecular flux is underestimated due to an underestimation of the total surface area between adjacent fluid elements. Now, $\langle L_{d,u} \rangle$, which is a function of λ_{grid}, but is independent of the concentration and the distance from the source, gives the factor of how much larger the surface area is compared to how it appears at that resolution λ_{grid}. Thus, we expect that the underestimated molecular flux between adjacent grid points, given by the scalar evolution equation in the set of governing equations of the numerical simulation, could be corrected *in some way* based on $\langle L_{d,u} \rangle$.

Finally, what can be done in the future? This study is only a starting point to the investigation of the fractal geometry of fluid interfaces in turbulent boundary layers. In fact, the limitations of the study, as summarized above, already indicate a line of approach to further studies. Besides a complete three-dimensional analysis of the concentration field, it would be also interesting to expand the range of concentration thresholds towards lower concentrations (of interest e.g. in environmental engineering, where pollutant limits are typically very low), and to expand the range of distances. Therefore, an improvement of the signal to noise ratio is necessary. The parameters

Reynolds number and vertical location of the source should be altered to investigate influences of the mixing transition and the turbulence intensity, respectively. Finally, there is an additional measure for the description of geometrical structures, called "lacunarity" (for an overview, see for example Plotnick et al., 1996; Allain and Cloitre, 1991; Smith et al., 1986). This scale-dependent quantity measures the degree to which a spatial pattern deviates from translational invariance. It can be related to the term of intermittency and thereby completes our framework of fractal measures. Overall, it may be appreciated that fractal geometry, with its affinity to detailed descriptions of physical-space properties, has become a powerful tool in the advance of turbulence research.

Bibliography

Allain, C. and Cloitre, M. (1991). Characterizing the lacuarity of random and deterministic fractal sets. *Physical Review A*, 44(6):3552–3558.

Allen, M., Brown, G. J., and Miles, N. J. (1995). Measurement of boundary fractal dimensions: review of current techniques. *Powder Technology*, 84:1–14.

Batchelor, G. K. (1959). Small-scale variation of convected quantities like temperature in turbulent fluid. *Journal of Fluid Mechanics*, 5:113–133.

Bublath, J. (1992). *Das neue Bild der Welt. Chaos, Relativität, Weltformel.* Ueberreuter, Wien.

Catrakis, H. J. (2000). Distribution of scales in turbulence. *Physical Review E*, 62:564–578.

Catrakis, H. J., Aguirre, R. C., and Ruiz-Plancarte, J. (2002). Area-volume properties of fluid interfaces in turbulence: scale-local self-similarity and cumulative scale dependence. *Journal of Fluid Mechanics*, 462:245–254.

Catrakis, H. J. and Bond, C. L. (2000). Scale distributions of fluid interfaces in turbulence. *Physics of Fluids*, 12:2295–2301.

Catrakis, H. J. and Dimotakis, P. E. (1996). Mixing in turbulent jets: scalar measures and isosurface geometry. *Journal of Fluid Mechanics*, 317:369–406.

Corrsin, S. (1951). On the spectrum of isotropic temperature fluctuations in isotropic turbulence. *Journal of Applied Physics*, 22:469–473.

Dasi, L. P. and Webster, D. R. (2003). Small-scale characteristics of the fluctuating passive scalar field in a turbulent boundary layer. In 3rd *International Symposium on Turbulence and Shear Flow Phenomena*, Sendai, Japan.

Dimotakis, P. E. (2000). The mixing transition in turbulent flows. *Journal of Fluid Mechanics*, 409:69–98.

Frederiksen, R. D., Dahm, W. J. A., and Dowling, D. R. (1996). Experimental assessment of fractal scale-similarity in turbulent flows. Part 1. One-dimensional intersections. *Journal of Fluid Mechanics*, 327:35–72.

Frederiksen, R. D., Dahm, W. J. A., and Dowling, D. R. (1997). Experimental assessment of fractal scale-similarity in turbulent flows. Part 2. Higher-dimensional intersections and non-fractal inclusions. *Journal of Fluid Mechanics*, 338:89–126.

Kolmogorov, A. N. (1941). Local structure of turbulence in an incompressible fluid at very high reynolds numbers. *Dokl. Akad. Nauk SSSR*, 30:299–303.

Kundu, P. K. (1990). *Fluid mechanics*. Academic Press, Inc., San Diego, CA.

Mandelbrot, B. B. (1967). How long is the coast of Britain? Statistical self-similarity and fractional dimension. *Science*, 155:636–638.

Mandelbrot, B. B. (1975). On the geometry of homogenous turbulence, with stress on the fractal dimension of the iso-surfaces of scalars. *Journal of Fluid Mechanics*, 72(2):401–416.

Mandelbrot, B. B. (1982). *The fractal geometry of nature*. W. H. Freeman & Co., New York.

Miller, P. L. and Dimotakis, P. E. (1991). Stochastic geometric properties of scalar interfaces in turbulent jets. *Physics of Fluids A*, 3:168–177.

Obukhov, A. M. (1949). Structure of the temperature field in turbulent flows. *Izvestiya Akademii Nauk SSSR, Geogr. and Geophys. Series*, 13:58–69.

Plotnick, R. E., Gardner, R. H., Hargrove, W. W., Prestegaard, K., and Perlmutter, M. (1996). Lacunarity analysis: a general technique for the analysis of spatial patterns. *Physical Review E*, 53(5):5461–5468.

Pope, S. B. (2000). *Turbulent flows.* Cambridge University Press, Cambridge.

Richardson, L. F. (1922). *Weather prediction by numerical process.* Cambridge University Press, Cambridge.

Richardson, L. F. (1961). The problem of contiguity: an appendix of statistics of deadly quarrels. *General Systems Yearbook*, 6:139–187.

Roberts, P. J. W. and Webster, D. R. (2002). Turbulent diffusion. In Shen, H., Cheng, A., Wang, K.-H., Teng, M., and Liu, C., editors, *Environmental fluid mechanics - theories and application*, pages 7–45. ASCE Press, Reston, Virginia.

Shepherd, I. G., Cheng, R. K., and Talbot, L. (1992). Experimental criteria for the determination of fractal parameters of premixed turbulent flames. *Experiments in Fluids*, 13:386–392.

Smith, L. A., Fournier, J.-D., and Spiegel, E. A. (1986). Lacunarity and intermittency in fluid turbulence. *Physics Letters*, 114A(8,9):465–468.

Sreenivasan, K. R. (1991). Fractals and multifractals in fluid turbulence. *Annual Review of Fluid Mechanics*, 23:539–600.

Sreenivasan, K. R. and Meneveau, C. (1986). The fractal facets of turbulence. *Journal of Fluid Mechanics*, 173:357–386.

Sreenivasan, K. R., Prasad, R. R., Meneveau, C., and Ramshankar, R. (1989). The fractal geometry of interfaces and the multifractal distribution of dissipation in fully turbulent flows. *Pure and Applied Geophysics*, 131:43–60.

Tennekes, H. and Lumley, J. L. (1972). *A first course in turbulence.* MIT Press, Cambridge, MA.

Villermaux, E. and Innocenti, C. (1999). On the geometry of turbulent mixing. *Journal of Fluid Mechanics*, 393:123–147.

Webster, D. R., Rahman, S., and Dasi, L. P. (2003). Laser-induced fluorescence measurements of a turbulent plume. *Journal of Engineering Mechanics*, 129:1130–1137.